



**UNIVERSIDAD DE INVESTIGACIÓN DE TECNOLOGÍA
EXPERIMENTAL YACHAY**

Escuela de Ciencias Físicas y Nanotecnología

**TITLE: BEAM DYNAMICS IN FOURTH GENERATION LINACS:
SIRIUS AND CLEAR FIST DATA**

Trabajo de integración curricular presentado como requisito para la obtención
del título de Físico

Autor:

Cocha Toapaxi Carlos Eduardo

Tutor:

Ph.D. Yepes Ramírez Harold

Urcuquí, julio 2020

SECRETARÍA GENERAL
(Vicerrectorado Académico/Cancillería)
ESCUELA DE CIENCIAS FÍSICAS Y NANOTECNOLOGÍA
CARRERA DE FÍSICA
ACTA DE DEFENSA No. UITEY-PHY-2020-00009-AD

A los 22 días del mes de mayo de 2020, a las 16:00 horas, de manera virtual mediante videoconferencia, y ante el Tribunal Calificador, integrado por los docentes:

Presidente Tribunal de Defensa	Dr. MEDINA DAGGER, ERNESTO ANTONIO , Ph.D.
Miembro No Tutor	Dr. BRAMER ESCAMILLA , WERNER , Ph.D.
Tutor	Dr. YEPES RAMIREZ, HAROLD , Ph.D.

El(la) señor(ita) estudiante **COCHA TOAPAXI, CARLOS EDUARDO**, con cédula de identidad No. **1804569935**, de la **ESCUELA DE CIENCIAS FÍSICAS Y NANOTECNOLOGÍA**, de la Carrera de **FÍSICA**, aprobada por el Consejo de Educación Superior (CES), mediante Resolución **RPC-SO-39-No.456-2014**, realiza a través de videoconferencia, la sustentación de su trabajo de titulación denominado: **Beam dynamics and assessment in fourth generation LINACs: SIRIUS and CLEAR first data**, previa a la obtención del título de **FÍSICO/A**.

El citado trabajo de titulación, fue debidamente aprobado por el(los) docente(s):

Tutor	Dr. YEPES RAMIREZ, HAROLD , Ph.D.
--------------	-----------------------------------

Y recibió las observaciones de los otros miembros del Tribunal Calificador, las mismas que han sido incorporadas por el(la) estudiante.

Previamente cumplidos los requisitos legales y reglamentarios, el trabajo de titulación fue sustentado por el(la) estudiante y examinado por los miembros del Tribunal Calificador. Escuchada la sustentación del trabajo de titulación a través de videoconferencia, que integró la exposición de el(la) estudiante sobre el contenido de la misma y las preguntas formuladas por los miembros del Tribunal, se califica la sustentación del trabajo de titulación con las siguientes calificaciones:

Tipo	Docente	Calificación
Miembro Tribunal De Defensa	Dr. BRAMER ESCAMILLA , WERNER , Ph.D.	9,7
Presidente Tribunal De Defensa	Dr. MEDINA DAGGER, ERNESTO ANTONIO , Ph.D.	9,9
Tutor	Dr. YEPES RAMIREZ, HAROLD , Ph.D.	9,6

Lo que da un promedio de: **9.7 (Nueve punto Siete)**, sobre 10 (diez), equivalente a: **APROBADO**

Para constancia de lo actuado, firman los miembros del Tribunal Calificador, el/la estudiante y el/la secretario ad-hoc.

Certifico que *en cumplimiento del Decreto Ejecutivo 1017 de 16 de marzo de 2020, la defensa de trabajo de titulación (o examen de grado modalidad teórico práctica) se realizó vía virtual, por lo que las firmas de los miembros del Tribunal de Defensa de Grado, constan en forma digital.*

COCHA TOAPAXI, CARLOS EDUARDO
Estudiante

Dr. MEDINA DAGGER, ERNESTO ANTONIO , Ph.D.
Presidente Tribunal de Defensa



Firmado electrónicamente por:
ERNESTO ANTONIO
MEDINA DAGGER

Dr. YEPES RAMIREZ, HAROLD , Ph.D.
Tutor



Firmado electrónicamente por:
HAROLD
YEPES

Dr. BRAMER ESCAMILLA , WERNER , Ph.D.
Miembro No Tutor



Firmado electrónicamente por:
**WERNER
BRAMER**

CIFUENTES TAFUR, EVELYN CAROLINA
Secretario Ad-hoc



Firmado electrónicamente por:
**EVELYN CAROLINA
CIFUENTES TAFUR**

AUTORÍA

Yo, **Carlos Eduardo Cocha Toapaxi**, con cédula de identidad 1804569935, declaro que las ideas, juicios, valoraciones, interpretaciones, consultas bibliográficas, definiciones y conceptualizaciones expuestas en el presente trabajo; así cómo, los procedimientos y herramientas utilizadas en la investigación, son de absoluta responsabilidad de el autor del trabajo de integración curricular. Así mismo, me acojo a los reglamentos internos de la Universidad de Investigación de Tecnología Experimental Yachay.

Urcuquí, julio 2020.



Carlos Eduardo Cocha Toapaxi
CI: 1804569935

AUTORIZACIÓN DE PUBLICACIÓN

Yo, **Carlos Eduardo Cocha Toapaxi**, con cédula de identidad 1804569935, cedo a la Universidad de Investigación de Tecnología Experimental Yachay, los derechos de publicación de la presente obra, sin que deba haber un reconocimiento económico por este concepto. Declaro además que el texto del presente trabajo de titulación no podrá ser cedido a ninguna empresa editorial para su publicación u otros fines, sin contar previamente con la autorización escrita de la Universidad.

Asimismo, autorizo a la Universidad que realice la digitalización y publicación de este trabajo de integración curricular en el repositorio virtual, de conformidad a lo dispuesto en el Art. 144 de la Ley Orgánica de Educación Superior.

Urququí, julio 2020.



Carlos Eduardo Cocha Toapaxi

CI: 1804569935

Agradecimiento

En primer lugar, agradezco a Dios por darme salud y fuerza todos los días y, más importante, gracias por crear nuestro universo físico como una estructura matemática.

Agradezco profundamente a mis padres, Carlos y Patricia, por su confianza incondicional, su aliento y su paciencia infinita. Fue su amor lo que me levantó en momentos difíciles. A mi hermana, Pamela y a mi sobrino Gael, también por su amor y aliento a pesar de la larga distancia entre todos nosotros.

Gracias a mi tutor de tesis y asesor de investigación, el profesor Harold Yepes Ramírez, por ayudarme a convertir en investigador y a darme cuenta del poder del razonamiento crítico. También me demostró lo que un científico comprometido y trabajador puede lograr.

También agradezco al CNPEM por darme la oportunidad de participar en el programa '28 Programa de Becas de Verano del CNPEM' y llevar a cabo un proyecto de investigación en SIRIUS. Tengo mucho que agradecer a mis asesores en SIRIUS, Fernando y Liu, quienes han sido los principales mentores en mi aprendizaje de Física de aceleradores, siempre mostrando paciencia y cuidado en mi aprendizaje inicial. No podía dejar de agradecer a todos los del grupo de Física de Aceleradores, especialmente a Murilo, Ximenes, Ana y Guilherme porque siempre me ayudaron en mi aprendizaje, dándome valiosos comentarios en mis presentaciones y en el desarrollo del proyecto.

Quiero agradecer de todo corazón al CERN Summer Student Program y a mis supervisores Roberto Corsini y Kyrre Sjøbæk por darme la inolvidable oportunidad de trabajar y llevar a cabo un proyecto de investigación en CLEAR. También, quiero agradecer a todo el equipo de CLEAR por el apoyo en el desarrollo del proyecto, especialmente a Kyrre por toda la ayuda, consejos amigables y la formidable enseñanza sobre el Software y el Hardware en CLEAR necesarios para completar mi proyecto y a Antonio Gilardi por sus útiles comentarios.

Gracias a mi universidad, a todos mis profesores de Física, especialmente a Clara Rojas por inspirarme a investigar y ser parte de mi iniciación científica. Gracias también a todos mis compañeros de clase y ahora colegas.

No puedo olvidar a mis mejores amigos y compañeros de cuarto Jorge, Bryan y Fernando, por todo el apoyo en los momentos felices y difíciles y por todas las celebraciones de cada uno de nuestros logros.

Finalmente, le agradezco a mi novia Lupe. Ella ha sido mi mejor amiga y una gran compañera. Gracias por su amor, apoyo, ánimo, entretenimiento y ayuda para superar este período de la manera más positiva.

Resumen

En esta tesis, se estudia la dinámica del haz, es decir, la emitancia normalizada, la energía y la dispersión de energía a la salida de LINAC de SIRIUS. El interés es principalmente evaluar si los parámetros del haz cumplen los requisitos necesarios para su inyección adecuada en el Booster. En el modo Single-Bunch, se obtuvo una energía de 147.8 ± 0.2 MeV con un porcentaje de dispersión de energía de 0.18 ± 0.01 %, emitancia normalizada de 53.855 ± 0.007 mm.mrad para el plano horizontal y 51.07 ± 0.02 mm.mrad para el plano vertical. En el modo Multi-Bunch, energía de 147.6 ± 0.2 MeV con porcentaje de dispersión de energía 0.41 ± 0.02 %, emitancia normalizada de 50.747 ± 0.005 mm.mrad en el plano horizontal y 61.567 ± 0.007 mm.mrad en el plano vertical. Estos datos se ingresaron en una simulación para determinar la fuerza del cuadrupolo en los imanes de la línea de transporte. Experimentalmente, esta configuración de imán crea un transporte estable de haz de electrones hacia el Booster.

Por otro lado, se probó el nuevo sistema digital Basler instalado en CLEAR y para medir su eficiencia, se evaluaron la emitancia del haz y los parámetros Twiss comparando los resultados del sistema digital Basler con los resultados del sistema BTV tradicional. El nuevo sistema proporciona mejores resultados con respecto a la calidad y la resolución de las imágenes obtenidas. También muestra un error estándar más pequeño del tamaño medio del haz, lo que condujo a un error menor en el cálculo de la emitancia y los parámetros de Twiss. Además, se utilizó Monte Carlo para propagar los errores. En general, los resultados de Basler se parecen mucho a los del sistema BTV, especialmente en rangos de corriente cuadrupolo cercanos y equidistantes al punto mínimo de la parábola obtenida después de la exploración cuadrupolo. En el plano horizontal, los valores del tamaño del haz para los rangos de corriente lejos del punto mínimo tienden a crear parábolas ligeramente diferentes en ambas cámaras que conducen a resultados diferentes. En el plano vertical, este problema no fue observado. El principal culpable parece ser una mala alineación en la instalación física del sistema Basler. En el plano horizontal, una emitancia normalizada de 16.96 ± 0.01 mm.mrad y 13.843 ± 0.004 mm.mrad en el plano vertical se obtuvieron para la cámara BTV. Por otro lado, una emitancia normalizada de 16.94 ± 0.01 mm.mrad en el plano horizontal y 13.94 ± 0.01 mm.mrad se obtuvieron en el plano vertical para el sistema Basler. Todos estos cálculos se realizaron con una energía del haz de 200 MeV.

Palabras clave: Acelerador lineal, emitancia normalizada, energía del haz, dispersión de la energía del haz, parámetros Twiss, propagación de errores Monte Carlo, rango dinámico, sistema BTV, sistema Basler, CLEAR, SIRIUS.

Abstract

In this thesis, the beam dynamics, namely the normalized emittance, energy and energy spread at LINAC exit of SIRIUS are studied. The interest is mainly assessed if the beam parameters meet the necessary requirement for its proper injection into the Booster. In the Single-Bunch mode, an energy of 147.8 ± 0.2 MeV was obtained with energy spread percentage of 0.18 ± 0.01 %, normalized emittance of 53.855 ± 0.007 mm.mrad for the horizontal plane and 51.07 ± 0.02 mm.mrad for the vertical plane. In the Multi-Bunch mode, energy of 147.6 ± 0.2 MeV with energy spread percentage 0.41 ± 0.02 %, normalized emittance 50.747 ± 0.005 mm.mrad in the horizontal plane and 61.567 ± 0.007 mm.mrad in the vertical plane were obtained. These data were input in a simulation to determine the quadrupole strength in the transport line magnets. Experimentally, this magnet configuration creates a stable electron beam transport towards the Booster.

On the other hand, the new Basler digital system installed at CLEAR was tested and to measure its efficiency, beam emittance and Twiss parameters were assessed by comparing the results of the Basler digital system with the results of the traditional BTV system. The new digital system provides better results regarding the quality and resolution of the images obtained. It also shows a smaller standard error of the mean beam size, which led to a lower error in the emittance and Twiss parameters calculation. In addition, Monte Carlo was used to propagate the errors. In general, the Basler results closely resemble those of BTV system, especially in quadrupole current ranges near and equidistant to the minimum point of the parabola obtained after the quadrupole scan. In the horizontal plane, beam size values for current ranges far from the minimum point tend to create slightly different parabolas in both cameras leading to different results. In the vertical plane, this issue was not observed. The main culprit seems to be a bad alignment in the physical installation of the Basler system. In the horizontal plane, a normalized emittance of 16.96 ± 0.01 mm.mrad and 13.843 ± 0.004 mm.mrad and in the vertical plane were obtained for the BTV camera. On the other hand, a normalized emittance of 16.94 ± 0.01 mm.mrad in the horizontal plane and 13.94 ± 0.01 mm.mrad in the vertical plane for the Basler system were obtained. All these calculation were done with a beam energy of 200 MeV.

Keywords: Linear Accelerator, Normalized Emittance, Beam Energy, Beam Energy Spread, Twiss Parameters, Monte Carlo Error Propagation, Dynamic Range, BTV System, Basler System, CLEAR, SIRIUS.

Contents

List of Figures	xvi
List of Tables	xx
List of Papers	xxi
1 Introduction	1
1.1 Synchrotron Light Facilities	2
1.2 Synchrotron light	5
1.2.1 Radiation from relativistic electrons	5
1.2.2 Spectral Flux and Brightness	6
1.2.3 Emittance	6
1.3 Brief history of the Synchrotron accelerator facilities	7
1.3.1 FIRST GENERATION LIGHT SOURCES	7
1.3.2 SECOND GENERATION LIGHT SOURCES	8
1.3.3 THIRD GENERATION	8

1.3.4	FOURTH GENERATION SOURCES	8
1.4	SIRIUS: The largest Latin America Synchrotron facility ever built	9
1.5	CERN Linear Electron Accelerator for Research	10
1.6	Problem Statement	12
1.7	General and Specific Objectives	12
2	Theoretical Background	15
2.1	SIRIUS Injection system and LINAC	15
2.2	CERN Linear Electron Accelerator for Research	18
2.2.1	CALIFES injector and Experimental Beamline	19
2.2.2	Experimental beamline	21
2.2.3	Optical Diagnostic System	21
2.2.4	Beam Imaging system: Basler and BTV cameras	22
2.2.5	The new Basler Ace U acA1920-40gm camera.	23
2.2.6	Trigger System	24
2.3	Beam Dynamics	24
2.3.1	Basic Phenomenology	25
2.3.2	The Guide Field	26
2.3.3	Equations of motion	27
2.3.4	Separation of radial movement.	28
2.3.5	Pseudo-harmonic betatron oscillations	29
2.3.6	Betatron trajectories	30

2.4	Beam Emittance	31
2.4.1	Phase Space	31
2.4.2	Beam Emittance	33
2.4.3	Phase space transformation	34
3	Methodology	37
3.1	Measurement of beam Emittance and Twiss Parameters	37
3.1.1	Transfer Matrix Method	38
3.1.2	Thin lens approximation	39
3.2	Error propagation and uncertainties	40
3.3	Statistical data analysis	41
3.4	Beam Energy Measurement	42
3.5	Software Implementations	43
3.5.1	CLEAR Software Set-up	44
3.5.2	SIRIUS Software Set-up	47
4	Results & Discussion	49
4.1	Beam dynamics with first data of the LINAC of SIRIUS	49
4.1.1	Beam energy and beam energy spread results	49
4.1.2	Normalized beam emittance and Twiss parameters results	51
4.2	Beam optical diagnostic system at CLEAR	57
4.2.1	Quadrupole Scan Fitting	57

4.2.2	Dynamic range analysis	64
4.2.3	Improvements	66
5	Conclusions	67
	Bibliography	69
	Abbreviations	75

List of Figures

1.1	Main components of a modern synchrotron facility. Electrons from the e-gun are injected and accelerated into a LINAC an evacuated to the Booster Ring, where they undergo further acceleration. Then, they are injected into the Storage Ring being maintained in a closed path using bending magnets. The Beamlines use the radiation emitted from insertion devices and the beam energy lost is restored by a RF supply.	3
1.2	Main elements in a magnet lattice. A dipole bends the electron beam, a quadrupole focuses the bean and a sextupole solves chromaticity problems.	4
1.3	Wigglers and undulators. It in principle differ only in the size of the radiation excursions from a straight path that they force the electrons to execute.	4
1.4	Beamline Structure. Tangential to the storage ring, the radiation is normally monochromated and focused using x-ray optics onto a sample in the experimental hutch.	5
1.5	Radiation distribution from relativistic electrons. Left: Electromagnetic radiation emitted by acceleration of a charged particle travelling at small velocities compared to the speed of light. Right: Relativistically moving charged particles emit narrow radiation beam in the direction in which they are travelling	5
1.6	Beam emittance. The four parameters defining the emittances ϵ_x and ϵ_y of a beam propagating in z direction. Figure extracted from Willmott (2011).	7
1.7	The brilliance/brightness of synchrotron light sources. a) A historical graph showing the enormous increase in brilliance starting in the second half of the twentieth century. b) Typical spectral brilliance curves of devices commonly used in third-generation synchrotrons.	9

1.8	Theoretical brilliance of the most important Synchrotron Light facilities. SIRIUS brightness according to the produced photon energy will be the second powerful worldwide only below the ESRF-U and above ALS-U, MAX IV, ESRF-U.	10
1.9	CLEAR accelerator facility. Located in the experimental area of the CLIC experiment at CERN.	11
2.1	Layout of the SIRIUS injection system. It has a 150 MeV LINAC and a 3-GeV Booster in the same tunnel as the Storage Ring. The Booster and Storage Ring injection sections are placed close together to restrict the 'dirty' area in terms of radiation.	16
2.2	LINAC sectors of SIRIUS. Sector 01 is responsible for electron acceleration. Sector 02 and Sector 03 are experimental stations to measure beam emittance and beam energy respectively.	17
2.3	CLEAR beamline scheme: elements directly interacting with the beam, and the location of the experimental stations. Element positions indicate the middle of each element, rounded to the nearest cm.	19
2.4	OTR Optical Ray Diagram. The interference pattern is seen at the focal plane and the beam distribution is seen at the image plane.	22
2.5	Beam Imaging system at CLEAR. BTV and Basler cameras installed at 620 position at CLEAR beamline. BTV camera is perpendicular to the Beamline and Basler camera is at 90° from BTV camera and parallel to the Beamline.	23
2.6	Electron reference frame. Coordinates (s, x, y) describes the motion of a particle inside a storage ring around the design orbit.	25
2.7	Some beam trajectories with different initial conditions. a) Betatron $\beta(s)$ function. b) Cosine-like trajectory for $s = 0$. c) Sine-like trajectory for $s = 0$. d) A particular trajectory after several revolutions.	30
2.8	Beam Phase Space Ellipse. (x, x') phase space coordinates for an electron moving in s direction. α, β, γ are Twiss parameters and determine the ellipse shape and orientation.	32
2.9	Beam distribution in phase space. The beam distribution has a gaussian-like shape in x and x' planes.	33
3.1	Set-up for emittance measurement at LINAC exit of SIRIUS, sector 02. Varying the current of the quadruple, the quadrupole strength will change to have a different focusing condition.	38

3.2	Set-up for emittance measurement at CLEAR. Varying the current of any quadrupole of the quadrupole triplet to have a different focusing condition.	38
3.3	Experimental set-up for Energy and Dispersion measurement, LINAC-Sector 03. The spectrometer bends the beam 45° through a OTR screen to emit the OTR radiation towards a profile monitor/camera.	42
3.4	Beam images for 620 BTV and Basler cameras. Under a certain quadrupole current, the image from the Basler cameras presents better quality images as reduced noise and better resolution.	45
3.5	Beam Fittings for BTV and Basler cameras. Example of beam size fittings using the script done for vertical and horizontal planes.	45
3.6	t-test using the Basler and BTV results. The normalized emittance distributions for both cameras presents quite similar distributions with a p-value bigger than the acceptance level.	46
3.7	Beam images coming from the profile monitor. The script perform gaussian beam fittings in horizontal and vertical planes over the beam images for the two modes of LINAC operationm.	47
4.1	Beam energy and energy spread results. For the Single-bunch mode and Multi-bunch mode at the LINAC exit, the E and σ_δ results are oscillating around the mean value due to thermal effects.	50
4.2	Quad-scan beam fitting for Single-bunch mode. For vertical and horizontal plane the beam size is quadratic as function of quadrupole current. $E = 147.8$ MeV at SIRIUS LINAC.	51
4.3	Normalized emittance and Twiss parameters distributions. Monte Carlo error propagation results for horizontal plane (left) and vertical plane (right). Single Bunch mode at $E = 147.7$ MeV	52
4.4	Quad-Scan beam fitting for Multi-Bunch mode. For vertical and horizontal plane the beam size is quadratic as function of quadrupole current. $E = 147.80$ MeV.	54
4.5	Normalized emittance and Twiss parameters distributions. Monte Carlo uncertainty propagation results for horizontal (left) plane and vertical plane (right). Multi Bunch mode at $E = 147.592$ MeV	55
4.6	Phase space ellipses at the LINAC exit. As expected the equation of motion for each operation mode in both planes describes an ellipse in phase space.	56
4.7	CLEAR quad-scan QFD510 beam results. Fitting for BTV and Basler cameras are shown with their corresponding uncertainties. Current range: 10-30 A at $E = 200$ MeV. Horizontal plane.	57

4.8	CLEAR horizontal plane analysis. Current range from 18-28 A. Left: Normalized emittance and Twiss parameters distributions for quad-scan QFD510 at $E = 200$ MeV. Right: Subtracted mean distributions and their respective statistics analysis results.	59
4.9	CLEAR horizontal plane analysis. Current range from 10-30 A. Left: Normalized emittance and Twiss parameters distributions for quad-scan QFD510 at $E = 200$ MeV. Right: Subtracted mean distributions and their respective statistics analysis results.	60
4.10	Quad-scan results QFD520 at 200 MeV, vertical plane. The standard errors of the mean describe a quadratic dependence as function of the quadrupole current.	62
4.11	CLEAR Vertical plane analysis. Current range from 27-38 A. Left: Normalized emittance and Twiss parameters distributions for quad-scan QFD520 at $E = 200$ MeV. Right: Subtracted mean distributions and their respective statistics analysis results.	63
4.12	CLEAR Dynamical range analysis. Emittance and Twiss parameters results as function of different dynamic ranges. Horizontal plane.	65

List of Tables

2.1	Design parameters of the LINAC of SIRIUS. It operates at energies bigger than 150 MeV with emittances around 50 mm.rad in two different operation modes.	18
2.2	Design parameters of the LINAC of SIRIUS. It operates at energies bigger than 150 MeV with emittances around 50 mm.rad in two different operation modes.	18
2.3	Beam and laser properties at CLEAR. Left: CALIFES photo-injector laser properties. Right: General beam parameters at CLEAR.	20
2.4	BTV and Basler cameras differences. The Basler camera has better qualities than the traditional BTV system such as bigger sensor resolution and lower signal-to-noise ratio.	24
4.1	Beam parameters and energy results at the LINAC exit, SIRIUS.	56
4.2	Quadrupole Scan QFD510 results (CLEAR). Horizontal plane, I1=QDF520, I2=QDD515, I3=QFD510.	58
4.3	Quad-scan QFD520 results (CLEAR): Vertical plane, I1 = QFD520, I2 = QDD515, I3 = QFD510.	62
4.4	Different dynamic ranges. Different current ranges to analyze until what range the results are similar for both cameras.	64
4.5	Global beam results for normalized emittance and Twiss parameters. Horizontal Plane	65
4.6	Global beam results for normalized emittance and Twiss parameters. Vertical Plane	65

Chapter 1

Introduction

Nowadays, humanity faces a series of major challenges whose solutions are fundamental to its sustainable evolution. Responses to global health, clean water, energy, environment, climate change and food for a global population of about 11 billion¹ by the end of the century are increasing. To deal with these social and economic challenges, strategic areas starting from small scale science such as nanotechnology, biotechnology, polymers, alternative energy, energy consumption to finish with large scale sciences like astrophysics, cosmology are helpful connections to investigate the structure and behaviour of matter at the elementary level, the subatomic level. The new frontier of knowledge brings the scale of the atom to engineering, promoting the development of new technologies and products for solving the significant questions and problems of humanity. Then, it is crucial that policy guidelines for innovation stimulate the creation of scientific infrastructures that openly operate and become available to the academic community and the productive sectors of agriculture, industry and services, allowing the analysis of raw materials in their most varied forms².

Particle accelerator facilities are good examples of open and multidisciplinary research infrastructures and interesting tools for solving challenges relevant to the academy and industry. These are the essential tools by which scientists have been able to probe the nucleus, determine its structure and behaviour³. For the most basic inquiries of dynamics and structure of matter, space and time, scientist seek particle/radiation-matter interactions at several energies ranges. Elementary particle physicists tend to use these machines creating beams of electrons, positrons, protons, or anti-protons interacting with each other at different initial conditions and evaluating the dynamics of the system.

For instance, the versatility of Synchrotron Light Sources enable the development of research in strategic areas such as energy, food, environment, health, defense and many others through the production of high power synchrotron light⁴. In agriculture, the synchrotron light may be used for soil analysis and for the development of more efficient and cheaper fertilizers that are less harmful to the environment and health. In the energy sector, the use of synchrotron

light allows the development of new technologies for the exploration of oil and natural gas and for the understanding and development of materials and systems for solar cells, fuel cells and batteries as well as in the research of new, lighter and more efficient materials. In the health area, synchrotron light is useful for the identification of the structures of proteins and complex intracellular units, a vital step for the development of new drugs, as well as for the development of nanoparticles for the diagnosis of cancer and fighting viruses and bacteria⁵.

On the other hand, Colliders in particle physics are used as a research tool to accelerate particles at relatively high kinetic energies and let them impact other particles⁶. Analysis of the products of these collisions gives scientists good evidence of the structure of the subatomic world and the laws of nature governing it⁷. That's why these technologies become increasingly popular around the world. It is also the reason because countries with strong technology-based economies already either have one or more Particle Accelerator Facilities, or are building them as part of their nation scientific policy and infrastructures⁸.

1.1 Synchrotron Light Facilities

In any accelerator structure, the **e-gun** as indicated in Figure 1.1, begins the acceleration process⁹ by running high voltage (HV) electricity ($\approx 10^5$ V) through a heated cathode which produces pulses of electrons that enter the Linear Accelerator (LINAC). As electricity flows through the cathode, it gets heated ($\approx 10^3$ K) to incandescence which gives electrons enough energy to leave the surface of the cathode, essentially "boiling" electrons off. Meanwhile, a nearby screen is given a faster and strong positive charge which pulls the electrons away from the cathode toward the LINAC. The HV electricity running through the cathode also repels the electrons being produced by the cathode and accelerates them towards the LINAC.

The **LINAC**¹⁰ consists typically of Radio Frequency (RF) cavities with fields able to oscillates up to THz. Electrons produced by the e-gun enter the LINAC and the RF cavities accelerate the electrons to an energy in the MeV order. At this energy, electrons are already traveling in an relativistic limit, at 99.9998% the speed of light (c). The LINAC produces pulses of electrons ranging from 2 up to 140 ns for injection into the **Booster Ring** in which a new RF cavity raises the energy of the electrons from MeV to GeV as they circulate through it¹¹. Electrons are so fast (approximately 99.999998% c) that circulate the Booster Ring approximately 1.5 million times in 0.6 s. Each of the bunches contains pC of charge ($\approx 3 \times 10^8$ electrons).

Following this boost in energy, the electrons are then transferred to the **Storage Ring**¹¹. During normal operations, long pulses are used to produce several ns pulse trains in the Storage Ring, this mode is called "*Multi-Bunch*" injection. After several minutes, enough electrons are accumulated in the Storage Ring in such a way the Synchrotron can operate for several hours and the LINAC can be turned off until more electrons are required to refill the ring. The LINAC can also produce short pulses to fill a "*Single-Bunch*" injection of electrons in the Storage Ring, which is used for more sensitive studies.

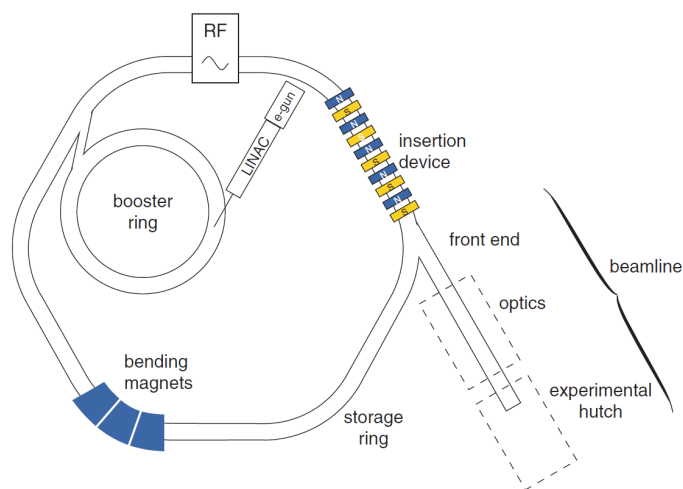


Figure 1.1: **Main components of a modern synchrotron facility**⁹. Electrons from the e-gun are injected and accelerated into a LINAC and evacuated to the Booster Ring, where they undergo further acceleration. Then, they are injected into the Storage Ring being maintained in a closed path using bending magnets. The Beamlines use the radiation emitted from insertion devices and the beam energy lost is restored by a RF supply.

The Storage Ring is almost circular-shaped distributed in magnet lattices, each with dipole (two-pole) magnets and a set of quadrupole (four-pole) and sextupole (six-pole) magnets to narrow and store the electron beam, see Figure 1.2. The magnetic field created by the dipole magnets is used to direct the electrons around the Booster and Storage Ring. The field of the quadrupole and sextupole magnets are used to force bunches of electrons into a narrow beam within the vacuum chamber. The Booster Ring uses dipole and quadrupole magnets, whereas the Storage Ring uses dipole, quadrupole and sextupole magnets¹².

Inside the Storage Ring, electrons travel in a straight line, but their path is bent by Bending Magnets (BMs), which force electrons to emit photons producing synchrotron light typically in a range of 4-12 hours. Over time, the number of electrons stored in the ring will decline inevitably because electrons collide with impurities (the vacuum is not perfect). As a result, the Synchrotron must either empty the ring and re-inject electrons or add more electrons using the Single-Bunch mode to maintain the required current.

The synchrotron accelerator uses two **RF cavities**⁹, one in the Booster Ring and one in the Storage Ring. The purpose of the RF cavities is to boost the energy of electrons using standing microwaves. The Booster Ring has a cavity that delivers a high-energy kick to the electron bunches during each turn around the ring. The Storage Ring uses a RF cavity to compensate the energy lost by electrons as they produce light. The operating temperature of the Storage Ring RF cavity is near absolute zero making possible to eliminate sources of power losses, while RF field is providing energy.

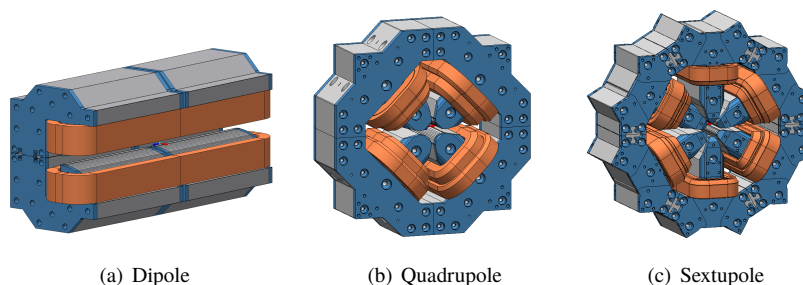


Figure 1.2: **Main elements in a magnet lattice**¹². A dipole bends the electron beam, a quadrupole focuses the beam and a sextupole solves chromaticity problems.

One of the ways that a synchrotron achieves a high quantity of photons is through Insertion Devices (IDs) that increase the brightness of the light produced by the electrons before entering the so-called Beamline. While dipole magnets change the direction of the electrons producing light, the multi-magnets called Wigglers and Undulators placed in the straight section of the Storage Ring move or ‘wobble’ electrons back and forth multiple times creating a narrow beam of highly intense light⁹, see Figure 1.3. As the Wiggler produces a wide range of high energy X-rays, the Undulator produces even higher intensity X-rays with a narrower range of energies.

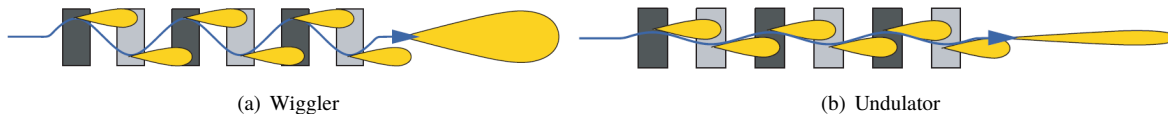


Figure 1.3: **Wigglers and undulators**⁹. In principle they differ only in the size of the radiation excursions from a straight path that they force the electrons to execute.

A **beamline** is an experimental station accessible for scientists using the synchrotron light as part of their research⁹. The beamlines run off tangentially to the storage ring, along the axes of the insertion devices and tangentially at bending magnets. The first hutch section of a beamline has several safety functions. It isolates the beamline vacuum from the storage ring vacuum; it monitors the position of the photon beam; it also filters out the low-energy tail of the synchrotron radiation spectrum (which is strongly absorbed by matter and can damage optical components) and blocks undesirable x-ray and Bremsstrahlung radiation during access to next sections. The beam is then usually focused and monochromated in the optics hutch before it enters the experimental hutch, as depicted in Figure 1.4. For those beamlines generating high-energy x-rays, the hutches are shielded using lead-lined, thick concrete walls, to protect users from x-rays, gamma rays and high-energy neutrons, which can be produced in the storage ring because specific physics processes. In the experimental hutch, the maximum energy radiation is equal to the storage ring energy (few GeV). Due to some radiation penetrate deeply in matter, the effective radiation shields may consist of tens of centimeters of lead blocks. Therefore, experiments in the Beamline are performed remotely outside the radiation area.

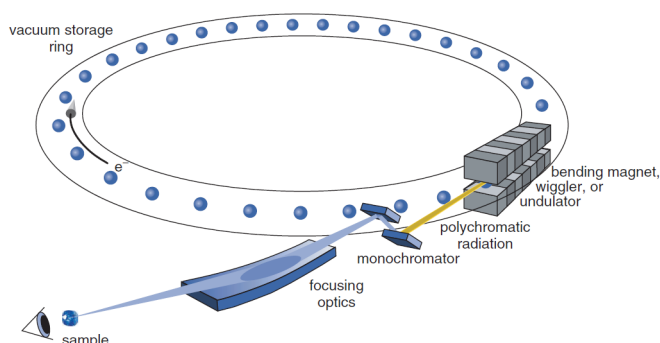


Figure 1.4: **Beamline Structure**⁹. Tangential to the storage ring, the radiation is normally monochromated and focused using x-ray optics onto a sample in the experimental hutch.

1.2 Synchrotron light

Synchrotron light/radiation is the electromagnetic radiation emitted when charged particles are accelerated radially¹³. The major applications of synchrotron light are in condensed matter, materials science, biology and medicine. The majority of experiments using synchrotron light involve probing the structure of matter from the sub-nanometer level of electronic structure to the micrometer and millimeter level.

1.2.1 Radiation from relativistic electrons

The radiation emitted by accelerated electrons moving at a small fraction of the speed ($v \ll c$) of light follows a dipole distribution and the radiation from a relativistic electron ($v \approx c$) moving along a circular arc follows a narrow light beam which radiates in the same direction as the electron motion⁹, see Figure 1.5.

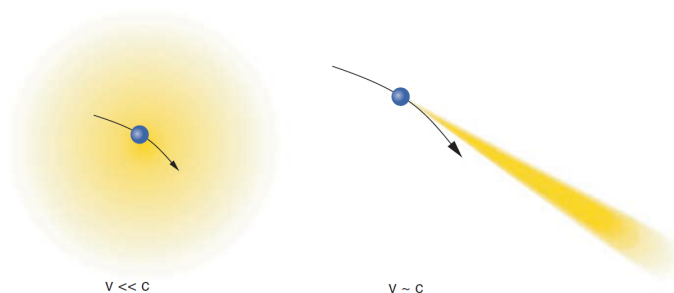


Figure 1.5: **Radiation distribution from relativistic electrons**⁹. Left: Electromagnetic radiation emitted by acceleration of a charged particle travelling at small velocities compared to the speed of light. Right: Relativistically moving charged particles emit narrow radiation beam in the direction in which they are travelling.

The shape and features of the released radiation depend on two parameters: the angular frequency ω_0 which is the number of radians turned by the electrons per second and the electron energy in the Storage Ring or where electrons are confined and forced to produce radiation.

1.2.2 Spectral Flux and Brightness

The spectral flux is defined as the number of photons per second per unit bandwidth passing through a defined area¹⁴, where the optical quality of a photon beam is characterized by the spectral brightness or brilliance defined as the flux per unit source area and unit solid angle or, in other terms, the flux distributed in space and angular divergence range (phase-space) as

$$B = \frac{dN_{ph}}{dt d\Omega dS \frac{d\omega}{\omega}} = \frac{\dot{N}_{ph}}{4\pi\sigma_x \sigma_y \sigma_{x'} \sigma_{y'} \frac{d\omega}{\omega}} \quad (1.1)$$

where \dot{N}_{ph} is the photon flux, $\sigma_x \sigma_y$ is the beam area, $\sigma_{x'} \sigma_{y'}$ is the beam divergence and $d\omega/\omega$ is a relative spectral bandwidth. Usually, B is expressed in units of photons/sec and $d\omega/\omega = 10^{-3}$ (standardized relative spectral bandwidth). Also, B helps to determine the smallest spot onto which a beam can in principle be focused. Brightness is a invariant quantity in perfect optical systems and thus is useful in designing beamlines and synchrotron radiation experiments which involve focusing to small areas¹⁵. The goal of any self-respecting beamline scientist is to approach the machine brightness as best as possible to its upper limit.

1.2.3 Emittance

From Equation 1.1, B is inversely proportional to both the source size and the beam divergence. The product of the linear source size and the beam divergence in the same plane is known as the **emittance** (ϵ)¹⁶. Therefore, to obtain as low emittance as possible the source needs emits radiation almost perfectly parallel and small. This address the challenge to whether emittance can be reduced, thereby increasing B . For a given Synchrotron storage ring, the emittance in a given transverse direction is constant and vary for each facility, being determined primarily by the degree of performance of the magnet lattice. The goal is to make this constant as small as possible. Referring to Figure 1.6, two emittances are usually set, within the plane perpendicular to the electron motion (z -direction), one in a radial direction x (i.e. the orbit plane) and the other, y , perpendicular to the orbital plane:

$$\epsilon_x = \sigma_x \sigma_{x'} \quad (1.2)$$

$$\epsilon_y = \sigma_y \sigma_{y'} \quad (1.3)$$

Experimentally, σ_x and σ_y are calculated using the standard deviations of beam gaussians fits in the x and y directions. Also, the measurement of the emittance is closely related to the measurement of the so-called Twiss parameters (α, β, γ).

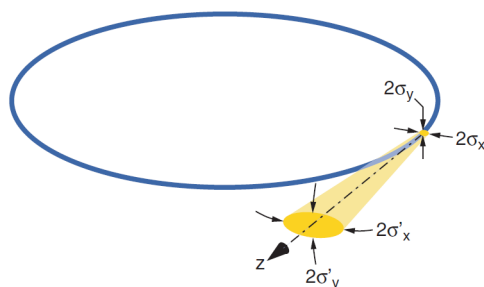


Figure 1.6: **Beam emittance**⁹. The four parameters defining the emittances ϵ_x and ϵ_y of a beam propagating in z direction.

1.3 Brief history of the Synchrotron accelerator facilities

The emission of synchrotron radiation was predicted theoretically by the Ukrainian Dmitri Iwanenko and the Russian Isaak Pomeranchuk in 1944¹⁷. In 24th April 1947, the first observation occurred at the General Electric Research Laboratory in Schenectady, New York. It was performed on a synchrotron particle accelerator, with electrons accelerated up to 99.997% c ¹⁸. The magnetic field produced by the electromagnets is varied in time when each cycle is completed and acts in a synchronized way over the particles, reaching higher velocities and therefore, higher energies. From this synchronous action comes the name synchrotron accelerator. At the beginning, synchrotron radiation was seen as an unwished but inevitable loss of energy in accelerators built (ironically) to produce intense beams of x-rays by directing accelerated electrons onto a target. In 1956, in a synchrotron accelerator at the University of Cornell, USA, Diran Tombouljian and Paul Hartman realized that they could use synchrotron radiation to perform spectroscopy experiments¹⁹. The first experiments were carried out in the ultraviolet region with the use of the radiation produced in the accelerator. Thus was started the use of the synchrotron light as a tool for the study of the composition and structure of materials.

1.3.1 FIRST GENERATION LIGHT SOURCES

By 1950-60's, particle accelerators originally developed for Nuclear Physics research were strategically turned for taking advantage of synchrotron radiation properties. It was the case of Deutsches Elektronen Synchrotron or German Electron Synchrotron (DESY) in Germany²⁰. From the late 60's and early 70's, this particle accelerator based on storage rings was capable of keeping particle beams circulating for long periods of time, replenishing the energy lost by the particles due to the emission of radiation. In nuclear and particle physics experiments, a storage ring in accelerators increases control over where and how the booster particles will collide with each other or with a target. The storage ring also enables the production of synchrotron radiation continuous, guaranteeing long periods of exposure of the samples they wish to analyze. The use of synchrotron radiation under such circumstances was called

"parasitic" operation, as the synchrotrons were primarily designed for high-energy or nuclear physics experiments and these kind of accelerators are considered the first generation of synchrotron light sources. Because most of these early facilities had storage-ring energies around or below 1 GeV allowed experiments in the ultraviolet and soft x-ray regimes.

1.3.2 SECOND GENERATION LIGHT SOURCES

Since the success of synchrotron radiation in target experiments, new facilities for long-term operation and improved equipment for light production began to emerge. In these new light sources, synchrotron light is produced when the electron beam path is bended by magnetic fields produced in dipoles magnets. However, the whole set of magnet machine, called the magnetic lattice, is designed to produce the greatest quantity and best quality of synchrotron radiation possible. This kind of facility became known as the Second Generation of Synchrotron Light Sources²¹.

1.3.3 THIRD GENERATION

Third-generation synchrotrons are characterized by their ability to produce highly parallel and narrow beams of x-rays with high intensity²². This generation is characterized by the advancement in accelerator and brighter designs, built to optimize the use of IDs. The brilliance of a third generation undulator is around 10^{20} photons/s/mrad²/mm²/0.1% bw for a photon energy of 1keV (see Figure 1.7.b), two or three orders of magnitude lower than high-quality visible laser sources⁹. The sources of this generation began to emerge in the 90's and many others were built over the next decade. The first third-generation facility to be completed was the European Synchrotron Radiation Facility (ESRF)²³, a 6 GeV storage ring in Grenoble, France, which began experiments in 1994. At date, the ESRF is undergoing a facility-wide upgrade which promises an enhancement of performance by approximately one order of magnitude.

1.3.4 FOURTH GENERATION SOURCES

Recent technological developments based on storage rings, with machines able to achieve "ultra-high" brightness have allowed the definition of a 4th generation Synchrotron light sources²⁴. These facilities have innovative designs of the magnetic lattice, the set of magnets that controls better the trajectory of the electron beam. In this new generation, MAX-IV²⁵ is one source already in operation and one under commissioning is SIRIUS in Brazil, start-up planned for 2021²⁶. There are also 3rd generation sources around the world already planning upgrades to become 4th generation such as: APS-U (Argonne, USA)²⁷ or SPring8-II (Kotu, Japan)²⁸, among others.

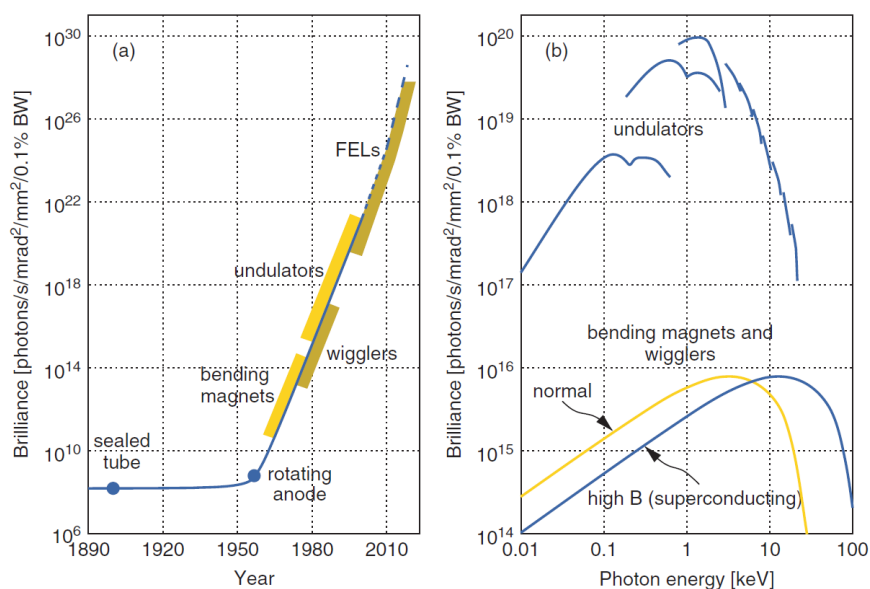


Figure 1.7: **The brilliance/brightness of synchrotron light sources**⁹. a) A historical graph showing the enormous increase in brilliance starting in the second half of the twentieth century. b) Typical spectral brilliance curves of devices commonly used in third-generation synchrotrons.

1.4 SIRIUS: The largest Latin America Synchrotron facility ever built

SIRIUS is a 4th generation synchrotron light source, designed to have one of the best world performance. It was inaugurated recently in November 2018 at CNPEM in Sao Paulo²⁶. It will be the largest and most complex scientific infrastructure ever built in South America at date of 1st running. It is planned to set Brazil in a leading position in the production of synchrotron light and designed to have a powerful brightness, enhancing new horizons for material characterization techniques and expanding the frontier of knowledge in the area¹¹.

After full commissioning, SIRIUS will consist of an electron accelerator with an energy of 3 GeV, which will have 518.4 m of circumference and can hold up to 40 Beamlines. These parameters will allow the new synchrotron to improve quantitatively the characteristics of experiments that are already done in UVX (second-generation 1.5 GeV synchrotron light source), reducing the data acquisition time and increasing the accuracy of the measurement results.

The Synchrotron radiation produced by SIRIUS will be characterized by having a superpower brightness produced by the acceleration of electrons close to c . This brightness will be the second powerful worldwide²⁹ getting over ALS-U³⁰ and MAX IV²⁵, standing only below the ESRF-U²³, see Figure 1.8.

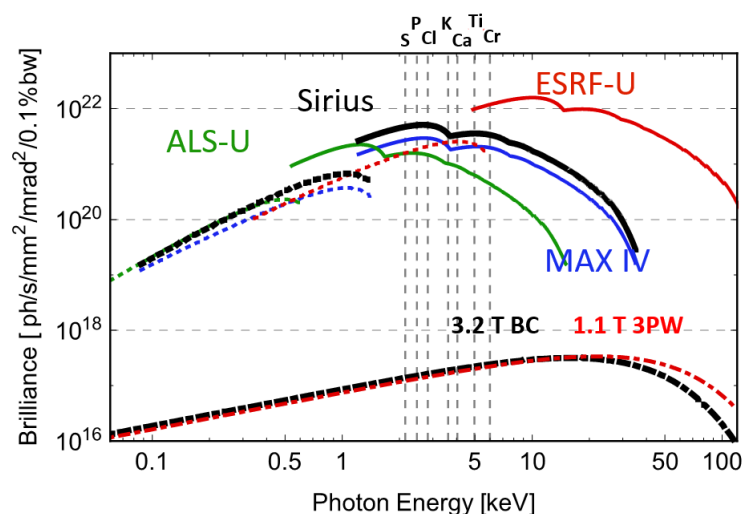


Figure 1.8: **Theoretical brilliance of the most important Synchrotron Light facilities**²⁹. SIRIUS brightness according to the produced photon energy will be the second powerful worldwide only below the ESRF-U and above ALS-U, MAX IV, ESRF-U.

SIRIUS will have twice the UVX energy and an emittance approximately 360 times less than UVX. This combination will make the brightness of the synchrotron light emitted, at certain frequencies, more than a billion times greater than what is available nowadays¹¹. The energy of the UVX light beam reaches only the surface layer of hard and dense materials to be analyzed, since the X-rays produced at that source penetrate these materials with depths of only a few micrometers. The high energy of SIRIUS will allow these same materials to be analyzed at depths of up to a few centimeters.

1.5 CERN Linear Electron Accelerator for Research

The European Organization for Nuclear Research, known as **CERN**, is a research organization operating the largest particle physics laboratory in the world. Established in 1954, the organization is based in Geneva on the Franco-Swiss border. CERN's main function is to provide the particle accelerators and other infrastructure needed for high-energy physics research, as a result, numerous experiments have been constructed at CERN through international collaborations.

Many activities at CERN spans around the Large Hadron Collider (LHC) and associated experiments. The LHC represents a large-scale, worldwide scientific cooperation project. The LHC tunnel is located 100 meters underground, in the region between the Geneva Airport and Jura mountains and consists of a 27 km circumference circular tunnel where seven experiments (CMS, ATLAS, LHCb, MoEDAL, TOTEM, LHC-forward and ALICE) are located along the collider; each of them with different physical perspective and using different detection technologies.

A new user facility focused in accelerator R&D and component studies for future machines at CERN know as CERN Linear Electron Accelerator for Research (CLEAR), see Figure 1.9, was set up in fall 2017. CLEAR aims covers both the prototyping and validation of accelerator equipment for the upgrade of the LHC with its injector chain and research of high-gradient acceleration methods such as X-band studies for LINACs, plasma and THz acceleration³¹. The proposed R&D electron beam facility is a modification of the CALIFES electron LINAC installed in the experimental area of the CLIC Test Facility 3 (CTF3) at CERN.

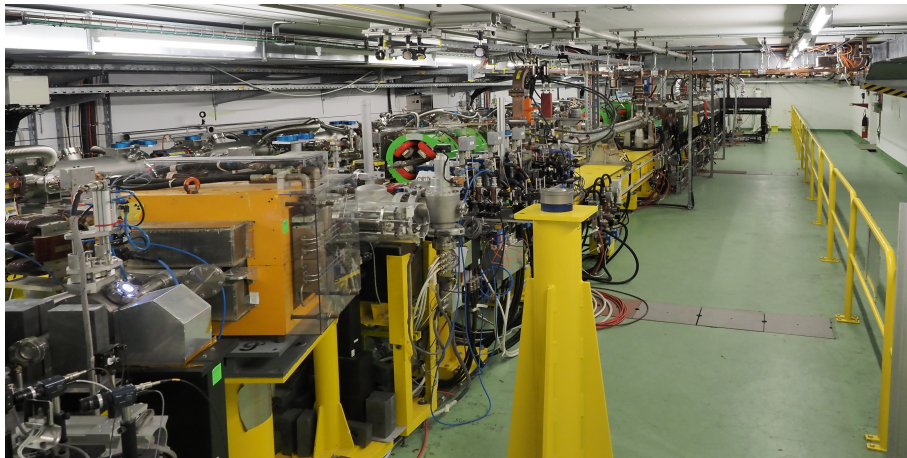


Figure 1.9: **CLEAR accelerator facility**³¹. Located in the experimental area of the CLIC experiment at CERN.

It also has is various programs of electron beam irradiation, including experiments for high-energy electron radiotherapy techniques and tests of electronic components for space applications. This can be achieved by using a flexible, accessible and modifiable beamline with several accessible parameters.

1.6 Problem Statement

This work addresses the commissioning of LINAC facility of SIRIUS and the assessment of the new digital imaging system at CLEAR, the analysis of their first data as a study of the beam dynamics.

In order to achieve a successful SIRIUS commissioning, control of main parameters as low normalized emittance and increasing energy range is mandatory. The LINAC is responsible for beam electron acceleration in a relativistic limit reaching an energy $E \approx 150$ MeV, with an energy spread $\sigma_\delta < 0.5$ % and normalized emittance $\epsilon_N \approx 50$ mm.mrad¹⁰. Beam energy and beam emittance parameters provide initial beam conditions in a transport line, which allows calculating the beam dynamics and optimal configuration of the focusing magnets. These measurements are crucial to minimize and correct the beam losses in the transport line and avoid emittance growth.

On the other hand, CLEAR is a LINAC capable of producing an electron beam generated from a photo-injector gun, by projecting a UV-laser on a Cs₂Te photocathode. The gun can produce low emittance bunches (< 2 mm.mrad) with high charge (up to 1.5 nC), either in trains with a few 100 bunches spaced at 1.5 GHz, or as single bunches. The beam is subsequently accelerated in two S-band accelerating structures to a final energy $E \approx 200$ MeV. One priorities at CLEAR is upgrade the beam data acquisition using a new digital imaging system.

The work presented in this manuscript is the result of the development and optimization of analysis tools for the first data obtained from the LINAC of SIRIUS, looking to characterize the beam dynamics, performing measurements of energy, energy spread and normalized emittance. It also allows to assess uncertainties on such parameters and check if the beam properties satisfy the coupling requirements for the Booster injection. At CLEAR, the commissioning of a novel digital system used for beam imaging (solving trigger and acquisition issues), the assessment performances of the beam data going through emittance and Twiss parameters measurements and the comparison of the results between the newly commissioned imaging system with the standard one are done.

1.7 General and Specific Objectives

The general objective is to carry out the first measurements of beam energy (E), energy dispersion (σ_δ), normalized emittance (ϵ_N) and Twiss parameters (α, β, γ) of the LINAC of SIRIUS and studying its beam dynamics. Based on the first part of the work an extension of the study is moved to CLEAR, where the measurement of beam parameters helps in the commissioning of novel digital cameras to improve the data acquisition system of CLEAR.

In order to achieve the general objective, specific objectives involve:

- Study theoretical and technical issues about the dynamics of the electron beam.
- Write, implement and optimize Software tools for data acquisition and analysis for LINACs.
- Perform measurements, corrections, data analysis, calibration and uncertainty analysis.
- Compare beam results between new imaging system and the standard one at CLEAR.

Chapter 2 is focusing in the theoretical background for the LINAC operation and calibration, covering the equations of motion, normalized emittance, energy and energy dispersion of the beam. It will be complemented by the Chapter 3 going from the code scripting and implementation to measure parameters as normalized emittance, Twiss parameters, energy and energy dispersion. Chapter 4 will be dedicated to discuss the obtained data and uncertainty studies. Conclusions of the work are summarized and discussed in Chapter 5.

Chapter 2

Theoretical Background

A LINAC is a particle accelerator for charged subatomic particles or ions to a high speed by using a series of oscillating electric potentials along a linear beamline whose structure is defined by the type of particle that is under acceleration. In particular, electron LINAC utilizes travelling waves rather than standing waves in the cavities. Because of their small mass, electrons travel close to c at energies as low as 5 MeV. They can, therefore, travel along the LINAC with the accelerating wave, in effect riding the crest of the wave and thus always experiencing an accelerating field.

LINACs have many applications, as generators of X-rays and high energy electrons for medicinal purposes in radiation therapy³², as particle injectors for higher-energy accelerators (like the LINAC of SIRIUS) or are used directly to achieve the highest kinetic energy for light particles, electrons and positrons, for particle physics (like CLEAR). Specially, the smallest LINACs, both proton and electron types, have important practical applications in medicine and in industry.

2.1 SIRIUS Injection system and LINAC

Most of the 3rd generation synchrotron radiation facility consists of a low energy LINAC, a Booster synchrotron and a Storage Ring. The injection system of SIRIUS is composed of a LINAC of 150 MeV, a Booster synchrotron with 3 GeV of total energy and 2 transport lines, one from the LINAC to Booster (LTB) and another from Booster to Storage Ring (BTS). The Booster and the Storage Ring are concentric and share the same tunnel. The injection sections are placed together to restrict the waste of radiation in the same area³³. A general design of the SIRIUS injection system is shown in Figure 2.1.

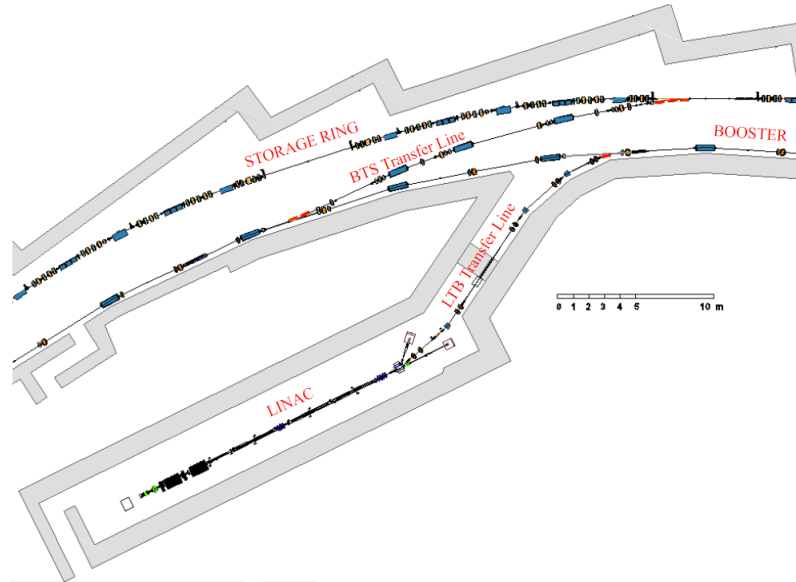


Figure 2.1: **Layout of the SIRIUS injection system**³³. It has a 150 MeV LINAC and a 3-GeV Booster in the same tunnel as the Storage Ring. The Booster and Storage Ring injection sections are placed close together to restrict the 'dirty' area in terms of radiation.

At the beginning of the LINAC a thermionic cathode grid e-Gun provides two modes of electron bunch with fixed bunch length and various bunch charges: the **Single-Bunch** and **Multi-Bunch** as described in Section 1.1. Those modes of LINAC are designed for the fast injection and single bunch operation of the Storage Ring. Multi-Bunch mode increases significantly the injection speed and reduces the injection time compared to the Single-Bunch mode.

The design of the LINAC has key characteristics. The LINAC installed at SIRIUS with S-Band RF technology provides an electron beam with a beam energy of 150 MeV, low emittance (≈ 50 mm.mrad per plane), low energy spread (< 0.5 %), fast switching between the Single-Bunch and Multi-bunch operation modes and tunable bunch charge for the SIRIUS injector¹⁰, which meets the requirement for a correct injection in the Storage Ring.

Several beam diagnostic sectors are installed along the LINAC. Beam parameters like bunch charge, emittance, beam profile, beam position, energy and energy spread can be measured at different positions, specially at exit where charge, profile, transverse position, energy, energy spread and emittance are measured. As reference, Sector-02 and Sector-03 (see Figure 2.2) located at the LINAC exit are the experimental locations where measurements of beam emittance and beam energy are carried out respectively.

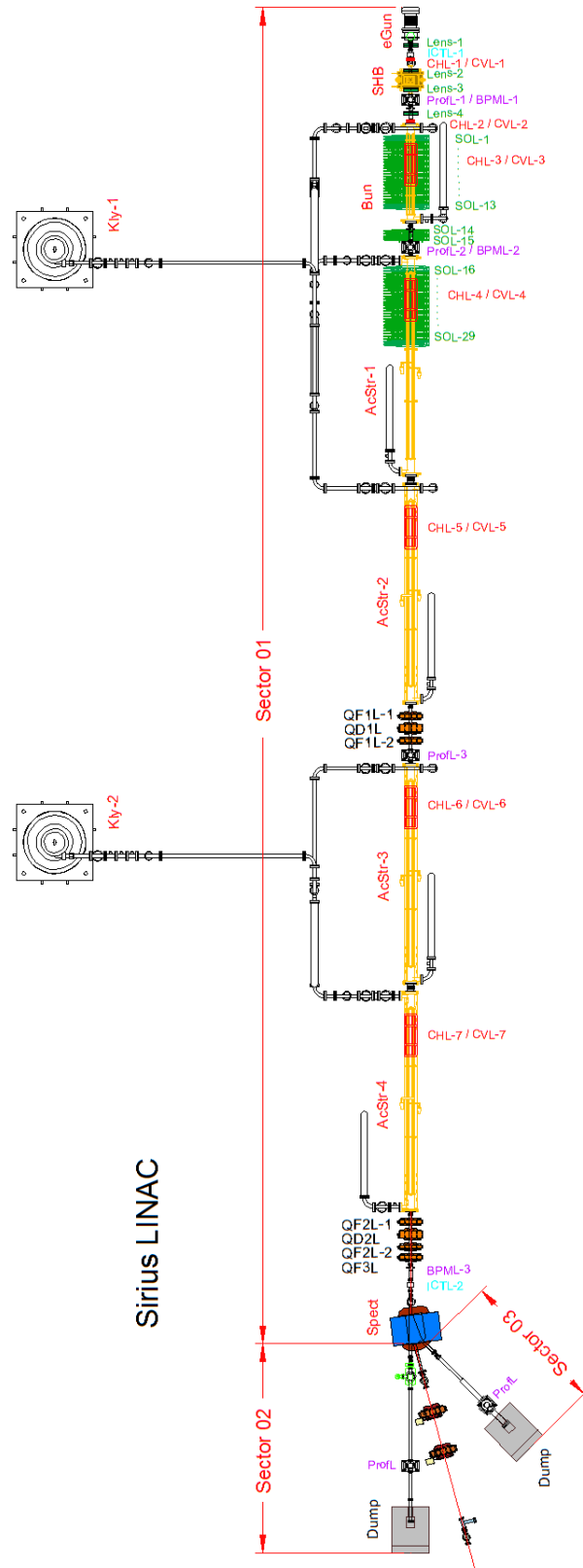


Figure 2.2: LINAC sectors of SIRIUS³³. Sector 01 is responsible for electron acceleration. Sector 02 and Sector 03 are experimental stations to measure beam emittance and beam energy respectively.

The design parameters of the LINAC of SIRIUS are summarizing in Table 2.1.

Beam Parameter	Nominal range	
Energy	≥ 150 MeV	
Relative RMS energy dispersion	≤ 0.5 %	
RMS Normalized emittance in each plane	$\leq 50 \pi$.mm.rad	
Pulse-to-pulse energy variation	≤ 0.25 %	
Pulse-to-pulse time fluctuation	≤ 100 ps	
Beam position variation pulse-to-pulse	≤ 0.2 mm	
Beam profile	Pulse load	Pulse duration
Multi-Bunch Mode	≥ 3 nC	$150 \approx 300$ ns
Single-Bunch Mode	≥ 1 nC	≤ 1 ns
Frequency of operation	2997.948 MHz, 499.658 MHz	
Repetition rate	≤ 10 Hz	

Table 2.1: **Design parameters of the LINAC of SIRIUS**¹⁰. It operates at energies bigger than 150 MeV with emittances around 50 mm.rad in two different operation modes.

Beam Parameter	Nominal range	
Energy	≥ 150 MeV	
Relative RMS energy dispersion	≤ 0.5 %	
RMS Normalized emittance in each plane	≤ 50 mm.mrad	

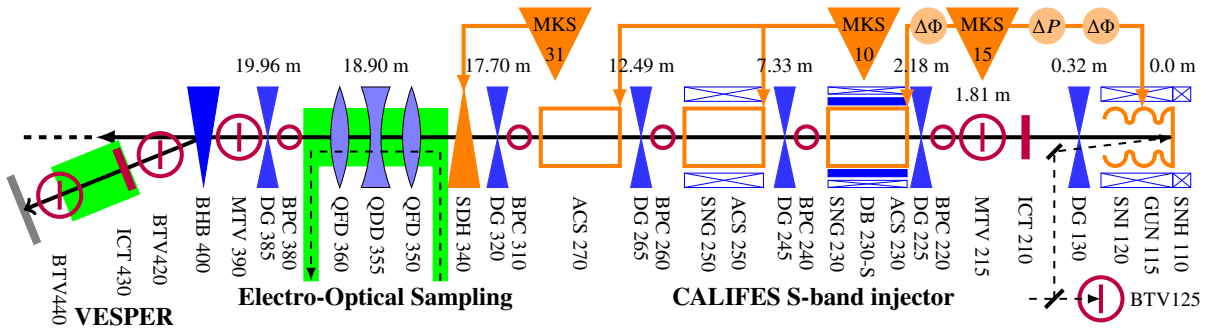
Table 2.2: **Design parameters of the LINAC of SIRIUS**¹⁰. It operates at energies bigger than 150 MeV with emittances around 50 mm.rad in two different operation modes.

2.2 CERN Linear Electron Accelerator for Research

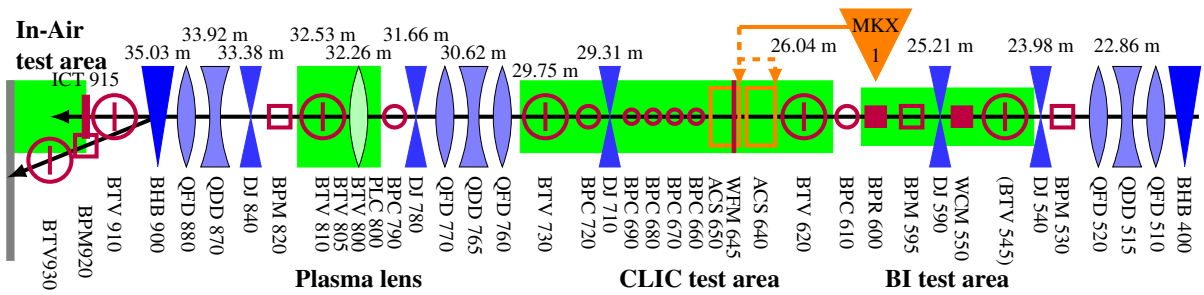
The CERN Linear Electron Accelerator for Research (CLEAR) is a new stand-alone user facility³⁴, aiming to: provide unique test capabilities to an international user community in key areas of accelerator R&D; support the development of high-gradient acceleration concepts, including the continuation of CLIC technology studies, but also to explore the potential of plasma acceleration technology; create a test bench for beam instrumentation and components for the consolidation and upgrade of the CERN and boost the collaboration with other scientific fields that need electron-beam test capability, including X-ray FELs, medical, space and industrial communities.

2.2.1 CALIFES injector and Experimental Beamline

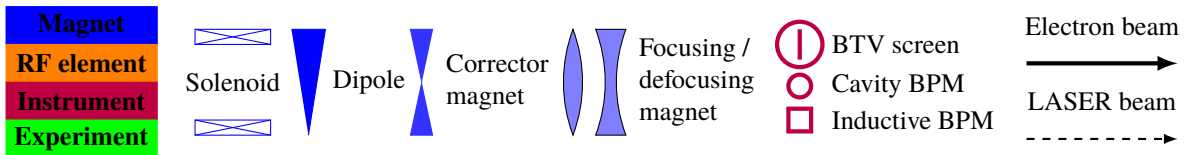
The CLEAR facility is hosted in the previous CLEX experimental area, building 2010 on CERN. The accelerator hall is approximately 42 m long and 7.8 m wide. The CLEAR beamline is installed along the middle of the hall, and it is composed of the CALIFES injector³⁵ (≈ 25 m long), followed by a beamline (16 m-long) that can be easily adapted to suit the requirements of the users.



(a) Layout of the CLEAR injector (CALIFES). The electron beam travels from right to left.



(b) Layout of the CLEAR experimental beamline. The electron beam, coming from the CALIFES injector, travels from right to left.



(c) Symbols

Figure 2.3: **CLEAR beamline scheme**³¹: elements directly interacting with the beam, and the location of the experimental stations. Element positions indicate the middle of each element, rounded to the nearest cm.

CALIFES injector

The CLEAR injector is basically unchanged with respect to CALIFES, except for major modification of the RF network and klystron sources. The actual layout installation is depicted in Figure 2.3.a, in which the electron beam is generated on a Cs₂Te photo-cathode pulsed by an UV (converted from IR) laser³⁶ and travels from right to left. The main laser parameters are summarised in Table 2.3, left side.

As Figure 2.3.a illustrates from right to left, three main section are identified: S-band injector, electro-optical sampling and VESPER. From the beginning the RF-gun (GUN 115) is followed by three LEP Injector Linac (LIL)³⁷ 4.5 m-long accelerating structures³⁸ (ACS 230, ACS 250 and ACS 270). This first structure can be used to tune the bunch length from 300 μm to 1.2 mm r.m.s. by means of velocity bunching. Both the gun, buncher and first accelerating structure are immersed in a tuneable solenoid field for focusing and space charge compensation. A matching section with three tuneable quadrupoles (QFD 350, QDD 355 and QFD360) dedicated mainly to beam emittance measurements and a VESPER spectrometer line for energy measurements complete the injector. The VESPER is also used as an irradiation test and to continue the studies on very high electron energy for medical application³⁹ and single event upset effects on electronics to future space missions⁴⁰.

CALIFES is also equipped with a rich set of beam diagnostic systems⁴¹. An Integrated Current Transformer (ICT) and a ceramic screen are installed right after the RF-gun to allow RF-gun characterization. Along the LINAC BPMs based on a coaxial re-entrant cavities⁴² are installed for transport optimization. Bunch length measurements are possible by means of an Electro-Optical Spectral Decoding (EOSD) system⁴³, streak camera measurements⁴⁴ or by using a dedicated S-BEND RF deflector⁴⁵. A transverse beam profile monitor⁴⁶ equipped with Yttrium Aluminium Garnet (YAG) scintillator and OTR screen is installed before the spectrometer. An additional ICT and YAG screen in the spectrometer line complete the longitudinal beam diagnostic capabilities.

The range of beam parameters of CALIFES exit are summarised in right side of Table 2.3.

Laser Parameter	Nominal range	Beam Parameter	Nominal range
Energy onto the cathode [nJ/bunch]	up to 270	Beam energy	60 MeV – 220 MeV
Intensity stability RMS	$\leq 3\%$	Bunch charge	10 pC – 2.0 nC
Spot size onto the cathode FWHM	1 mm	Bunch length	1 ps – 4 ps
Pointing stability onto the cathode rms	≤ 2 mm	Bunch frequency	1.5 GHz
Wavelength	262 nm	RF frequency	3.0 GHz
Micro bunch length FWHM	8 ps	Number of bunches	1 – 200
Micro bunching frequency	1.5 GHz	Beam repetition rate	1/(1.2 s) – 10 Hz
Number of micro bunches	0 to 300	RMS energy spread	$< 0.2\%$
Repetition rate	0.833 to 5 Hz	RMS ϵ_N at QFD350 entrance	1 μm –20 μm

Table 2.3: **Beam and laser properties at CLEAR**)³¹. Left: CALIFES photo-injector laser properties. Right: General beam parameters at CLEAR.

2.2.2 Experimental beamline

The CLEAR the experimental beamline layout is depicted in Figure 2.3.b, in which the beam travels also from right to left. After a matching section composed of three adjustable quadrupoles (QFD 510, QDD 515 and QFD 520), a two-meter-long section is dedicated to beam instrumentation tests (BI test area). Presently, it hosts a chamber (DI 590) for Optical (Diffraction) Transition Radiation Interferometry (OTRI/OTDRI) studies⁴⁷. Moreover, a few diagnostic taken from the now discontinued Drive Beam lines have been adapted and installed to fit the CLEAR beam specifications. This includes a high bandwidth Wall Current Monitor (WCM), two Drive Beam Inductive BPMs⁴⁸ and a wave guide pickup (BPRW) for non-destructive bunch length measurements⁴⁹.

The following CLIC Test area consists of the existing CLIC Two Beam Module (about 3 m long) on which a CLIC accelerating structure and three CLIC cavity BPM (BPC 660, BPC 670 and BPC 680) prototypes plus one older BPM (BPC 690) prototype are installed allowing the continuation of Wake Field Monitor (WFM)⁵⁰, and BPMs⁵¹ studies. The transverse position of the three new prototype CLIC cavity BPMs and of the CLIC structure is remotely adjustable to allow for precise relative positioning. After the CLIC Module, a matching section allows adjusting the beam before injecting it into a Plasma Test Stand which currently hosts a plasma lens experiment⁵².

Before the final spectrometer, about 1.5 m-long space is available for users, for example for planned impedance studies⁵³. The spectrometer line is mounted on a 1.2 m long and 0.9 m wide optical table. The straight line ends about 20 cm after the dipole with a 100 μm thick aluminium window, leaving about 1 m long in-air path for the beam. This area is well suitable for fast installation and test of equipment that does not necessarily need to be operated under vacuum.

2.2.3 Optical Diagnostic System

Optical diagnostic cameras in accelerator science and technology are essential hardware for both machine operation and experiments. For machine operation, beam cameras are able to determine beam position and profile, on straight sectors and in spectrometers. The beam position helps to verify that the bunches are on similar orbits, energy, and energy spread. Furthermore, cameras are used for measurements of bunch length, emittance and Twiss Parameters using a RF deflecting cavity and quadrupole scan technique. All these measurements require high coordination between the cameras and the involved instrumentation. For the experiments, they are mostly used to measure beam position and size as a function of different machine parameters such as mover positions and trigger timing.

Optical diagnostic provides images of accelerated particle beams by using radiation emitted by particles impinging a radiator (fluorescent screen), has been extensively used, especially on LINACs⁵⁴. Nowadays, higher intensity beams boost the use of beam imaging techniques to carry out precise measurements of relevant beam parameters such as emittance and energy by using optical transition radiation (OTR). It is well known that OTR is emitted when a

charged particle with constant velocity crosses two media with different dielectric constant, such as from vacuum to dielectric or vice-versa⁵⁵. In this sense, the single-particle spectral angular distribution for N photons, per unit frequency ($d\omega$) and solid angle ($d\Omega$) is⁵⁵

$$\frac{d^2N}{d\omega d\Omega} = \frac{2q^2}{\pi h c \omega} \frac{(\theta_x^2 + \theta_y^2)}{(\gamma^{-2} + \theta_x^2 + \theta_y^2)^2} \quad (2.1)$$

where q is the particle charge, h is Planck's constant, c is the speed of light, γ is the Lorentz factor of the particle, and θ_x and θ_y are the angles from the OTR emission axis.

Accelerator Science has developed several analytic and experimental techniques to measure the divergence and emittance of charged particle beams, by using OTR radiation generated from thin intercepting foils⁵⁶, see Figure 2.4. OTR's directionality, promptness, linearity, polarization, and the sensitivity of its angular distribution to energy and divergence can be used to diagnose the spatial distribution, energy, emittance and Twiss parameter of a charged particle beam.

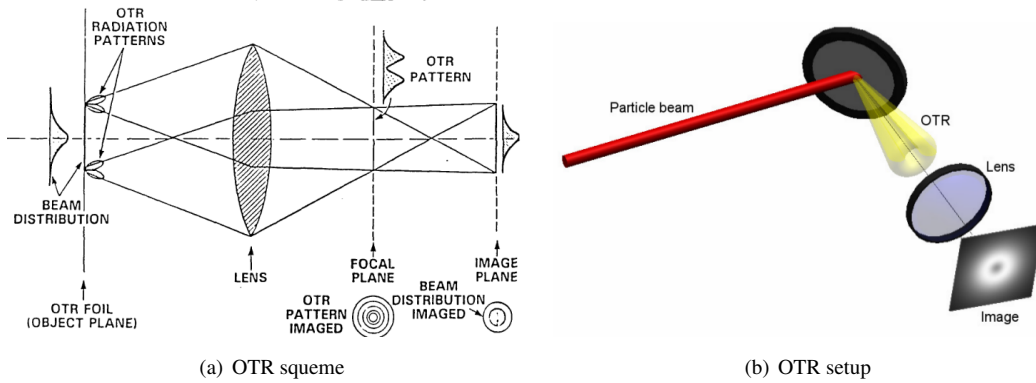


Figure 2.4: **OTR Optical Ray Diagram**⁵⁶. The interference pattern is seen at the focal plane and the beam distribution is seen at the image plane.

2.2.4 Beam Imaging system: Basler and BTV cameras

At CLEAR, there are installed six Basler cameras, one in position 620 (CLIC test area), three at the In-Air test stand (close the dump), and two on the Electro-Optical sampling section, see Figure 2.3.

The new Basler beam imaging system is built at 620 position with a beam splitting mirror to share the OTR light between the traditional Beam Observation TV (BTV) WAT-221S2 camera⁵⁷ and the Basler ac U acA1920-40gm camera⁵⁸ separated by 90 degrees, creating a mechanism to share the same images in both cameras, for direct comparison, see Figure 2.5.a. Also, the Basler camera is connected through Ethernet cable and trigger directly

connected to the relevant crate, where the lead shielding is to protect from undesired beam losses; unfortunately, the Basler camera is still exposed to radiation coming from the beam hitting the OTR screen, see Figure 2.5.b. Finally, the main differences between BTV and Basler cameras are summarized in Table 2.4, note that Basler camera has twice the BTV camera resolution.

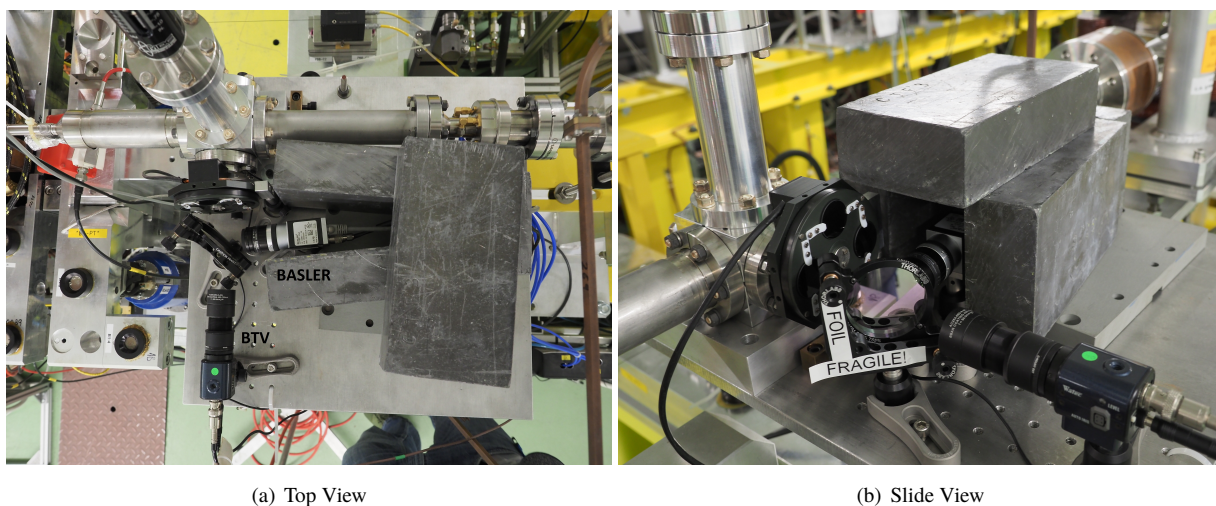


Figure 2.5: **Beam Imaging system at CLEAR.** BTV and Basler cameras installed at 620 position at CLEAR beamline. BTV camera is perpendicular to the Beamline and Basler camera is at 90° from BTV camera and parallel to the Beamline.

2.2.5 The new Basler Ace U acA1920-40gm camera.

The Basler Ace U acA1920-40gm camera supplies 1920 x 1200 resolution with surprising image quality with high quantum efficiency, wide dynamic range and extremely low noise. When this camera is configured to use the sensor full resolution, it is capable of delivering 40 frames/second (fps). This camera has relatively large $5.86 \mu\text{m}$ pixels allowing greater light sensitivity and field depth, and also requires less performance from a lens. To use its full resolution, an image circle of 13.27 mm and a 1/1.2" lens is needed and for lower resolution and cost a 2/3" (11 mm) is required.

This camera has a global shutter for “stop-action” imaging and can output a flash window signal to control the light source. Since the Basler camera and analog standard cameras use the same 29 x 29 mm footprint, the full replacement of analog cameras by a Basler camera is relatively easy. Using a Power over Ethernet (PoE) configuration, a single cable may be used to apply camera power and to transfer data between this camera and a CPU. The input is set-up to trigger image acquisition, reset the frame counter, or reset the software trigger count. The output is set-up to manage

SPECIFICATIONS	BTV WAT-221S2	Basler Ace U acA1920-40gm
Sensor Resolution	811(H) × 508(V), 550 TVL	1920 (H) x 1200 (V) pixels
Sensor Size:	8.4 μm(H) × 9.8 μm(V)	13.27 mm (1/1.2")
Sensor Model	1/2" interline transfer CCD image	Sony IMX249LLJ
Frame Rate (full resolution)	60 - 100.000 fps	40 fps
Quantum Efficiency		70.0 %
Dark Noise		6.7 e-
Saturation Capacity		31.9 ke-
Dynamic Range	WDR	73.6 dB
Signal-to-Noise Ratio	>55dB	45.0 dB
Lens Mount	CS - Mount	C-Mount

Table 2.4: **BTV⁵⁷ and Basler⁵⁸ cameras differences.** The Basler camera has better qualities than the traditional BTV system such as bigger sensor resolution and lower signal-to-noise ratio.

acquisition trigger wait, exposure active, flash window, or timer active. The output is controlled via CPU. Finally, the auxiliary connector should be used to power the camera if PoE is not available.

2.2.6 Trigger System

The 620 Bessler digital camera can be triggered with a TTL signal for beam-synchronous acquisition. The rate/interval should be synchronous with the beam, i.e. at the same rate as the probe beam gun frequency / CX.SLASER-PP. This trigger is set up as CX.DIGTRIG-BTVCLEX1 and created using a delayed version of the other triggers. Testing the trigger for the digital camera was observed that the main BTV camera trigger is delayed by almost one beam cycle (1.2 s). At minimum delay, when set to 0 (x 1 kHz) unfortunately 2 μs delay is recovered, measured by comparing to an alternative camera trigger used for the two final digital cameras using an oscilloscope, for seeing OTR beam. It has therefore been set to count for just below one whole cycle, i.e. triggering at the next beam.

2.3 Beam Dynamics

This section is dedicated to explain fully the beam electron dynamics, the equations that govern its behaviour with special emphasis in the equations inside the LINAC and its connection with the beam emittance and Twiss parameters. Then, Python scripts have been developed to do these calculations including error estimation and statistical analysis.

2.3.1 Basic Phenomenology

The starting point at LINAC is the production of short electron or proton beam pulses injected into a vacuum chamber embedded in a linear or a more or less circular magnetic guide field. The guide field focus the beam linearly or in closed paths to create a 'stored' beam. Its focusing properties conduct all electrons towards an ideal design orbit and cause them to execute lateral betatron oscillations (radial and vertical) around the ideal closed path⁵⁹. The electron beam looks like a strip of ribbon that has a stationary 'size' and 'shape', with a Gaussian distribution of amplitudes at each of the transverse and longitudinal coordinates. The shape of the beam will be different at each azimuthal position because the focusing properties of the guide field vary from one place to another⁵⁹.

Electrons are held inside the accelerating structure by the forces exerted by the magnetic guide field. Magnets are disposed along the ideal orbit. In practice, when the magnetic currents are adjusted to any particular set of consistent values, the designed fields are planned to be such that an electron of a nominal energy E_0 , once optimally injected, will move for long scheduled periods of time along the ideal orbit. Other stored electron bunches are limited by the guide field to move in quasi-periodic and stable trajectories in the vicinity of the ideal orbit. However, the treatment will be limited to the so-called linear approximation and will be applied only to electrons of constant energy, ignoring effects due to loss of radiation and accelerating fields. In most cases, the ideal orbit is in a plane, although the extension to more general cases is relatively simple. The discussion will be simplified assuming that the plane of the ideal orbit is horizontal⁵⁹.

The instantaneous position of an electron will be specified with (s, x, y) where s is the azimuth coordinate and represents the distance along the ideal orbit from some arbitrary reference point to the point closest to the electron. Both x and y are the horizontal (radial) and vertical distances from the ideal orbit, see Figure 2.6. The horizontal and vertical displacements are, of course, the displacements locally perpendicular to the design orbit.

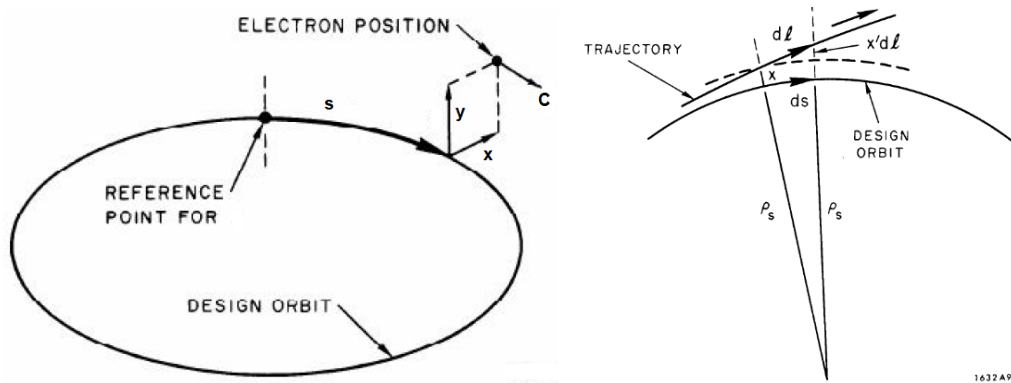


Figure 2.6: **Electron reference frame.** Coordinates (s, x, y) describes the motion of a particle inside a storage ring around the design orbit. Images adapted from Sands (1970)⁵⁹.

The coordinates x and y are always much smaller than the local curvature radius ρ_s of the trajectory. Thus, linear terms of the magnetic guide field variations in the vicinity of the ideal orbit must be preserved. These conditions are in the linear approximation.

2.3.2 The Guide Field

The guide field is assumed static, so the movement of an electron is determined only by the magnetic field strength \mathbf{B} at each point of its trajectory. As the ideal orbit has to be always horizontal, \mathbf{B} must be purely vertical everywhere in the mentioned orbit. Another assumption is that the setup of the magnetic field is ideally symmetric with respect to the ideal orbit plane⁵⁹. Taking into account all the assumptions, the magnetic guide field can be completely characterized by two essential quantities for each azimuthal position s , defining $B_0(s)$ the magnitude of the magnetic field on the ideal orbit and $(\partial\mathbf{B}/\partial x)_{0s} = (\partial\mathbf{B}/\partial y)_{0s}$ by Maxwell's relations, the horizontal gradient of the field strength evaluated at ideal orbit ($x = 0$). Since the field is symmetric with respect to the plane of the ideal orbit, $\mathbf{B}_0(s)$ and $\partial\mathbf{B}/\partial x$ have only vertical components, and only their magnitudes are enough to characterize the dynamics of the field.

In this sense, the two transverse components of the magnetic field acting over the electron in (s, x, y) coordinates can be written as

$$B_y(s, x, y) = B_0(s) + \left(\frac{\partial B}{\partial x}\right)_{0s} x, \quad (2.2)$$

$$B_x(s, x, y) = \left(\frac{\partial B}{\partial x}\right)_{0s} y. \quad (2.3)$$

The linear properties of the guide field can be defined by the following two functions⁵⁹

$$G(s) = \frac{qcB_0(s)}{E_0}, \quad (2.4)$$

$$K(s) = \frac{qc}{E_0} \left(\frac{\partial B}{\partial x}\right)_{0s} \quad (2.5)$$

where E_0 is the nominal energy, c is the speed of light and q is the electric charge. These two functions have a simple physical meaning, as the electrons are highly relativistic for which $E \approx cp$, thus $G(s)$ is only the inverse of the radius of curvature ρ_s of the electron nominal energy at $x = 0$ and $y = 0$ as

$$G(s) = \frac{1}{\rho_s} \quad (2.6)$$

Then, $G(s)$ represents the *curvature function* and $K(s)$ quantifies the rate of change of the inverse radius with radial displacement, better known as the *focusing function*.

2.3.3 Equations of motion

Electrons in a accelerator are moving on a trajectory near the design orbit with energy not necessarily at the design energy. The electron energy E in terms of the deviation δE of the nominal energy E_0 is defined as:

$$\delta E = E - E_0 \quad (2.7)$$

Assuming an electron moving in x with slope $x' = dx/ds$ where the slope represents the angle between the direction of motion of the electron and the tangent to the design orbit, see Figure 2.6. Setting θ_0 as the angle between the tangent and some arbitrary reference direction and θ the angle made by the path with the same reference direction:

$$x' = \tan(\theta - \theta_0) \approx \theta - \theta_0, \quad (2.8)$$

and

$$x'' = \frac{d(\theta - \theta_0)}{ds}. \quad (2.9)$$

The change $d\theta_0$ in the direction of the tangent to the ideal orbit in an azimuthal interval ds after some simplifications⁵⁹ is

$$-d\theta_0 = \frac{1}{\rho_s} ds = G(s)ds, \quad (2.10)$$

and in a trajectory element dl of the trajectory the change in the angle is

$$d\theta = -\frac{1}{\rho} dl = -\frac{qcB}{E} dl. \quad (2.11)$$

Due to the fact that

$$\frac{dl}{ds} = \frac{dl}{d\theta} \frac{d\theta}{d\theta_0} \frac{d\theta_0}{ds}, \quad (2.12)$$

it is possible to write

$$\frac{dl}{ds} = (-\rho) \frac{d\theta}{d\theta_0} \left(-\frac{1}{\rho_s} \right). \quad (2.13)$$

By writing in terms of the radius of curvature $\rho \approx \rho_s + x$ in the first order. Hence:

$$dl = \frac{\rho_s + x}{\rho_s} ds = \left(1 + \frac{x}{\rho_s} \right) ds = [1 + G(s)x]ds. \quad (2.14)$$

Next, writing for B

$$B = B_0 + \frac{\partial B}{\partial x} x = \frac{E_0}{ec} (G + Kx). \quad (2.15)$$

By putting these last two equations in Equation 2.11, together with $E_0 + \delta E = E$ and keeping only the first-order terms:

$$d\theta = [-G - (G^2 + K)x + G\delta]ds, \quad (2.16)$$

where $\delta = \delta E/E_0$. Then, Equation 2.9 turns to

$$x'' = -(G^2 + K)x + G\delta, \quad (2.17)$$

The corresponding equation for vertical motion is

$$y'' = Ky \quad (2.18)$$

Through the first approximation, the motion in x and y become independent. Finally, using the standard form, the equation of motion for an electron moving in x and y as function of s leads to

$$x'' = -K_x(s)x + G(s)\delta, \quad (2.19)$$

$$y'' = -K_y(s)y, \quad (2.20)$$

where the focusing properties are

$$K_x(s) = G^2(s) + K(s) \quad (2.21)$$

$$K_y(s) = -K(s) \quad (2.22)$$

In this way, the focusing functions should be necessarily periodic in s in a periodic path, the minimum period is a revolution of the ideal orbit, that is, for K_x and K_y (as well as for G), $K(s + L) = K(s)$ where L is the length of the ideal orbit. But, as a LINAC is not periodic this condition is not necessary.

2.3.4 Separation of radial movement.

Conceptually, it is convenient to split the radial movement into a displaced closed length x_ϵ out of the equilibrium orbit and the free transverse oscillation x_β over this orbit⁵⁹. If x is written as

$$x = x_\epsilon + x_\beta, \quad (2.23)$$

then, Equation 2.21 is fulfilled if the following equations are true:

$$x_\epsilon'' = -K_x(s)x_\epsilon + G(s)\delta, \quad (2.24)$$

$$x_\beta'' = -K_x(s)x_\beta. \quad (2.25)$$

The displacement x_ϵ is proportional to the deviation of energy δ , and as a function of s is convenient to express as

$$x_\epsilon(s) = \eta(s)\delta \quad (2.26)$$

where $\eta(s)$ is the dispersion function and characterizes the total guide field⁵⁹.

2.3.5 Pseudo-harmonic betatron oscillations

Around the accelerator K is not always constant and depends on s , so

$$x_{\beta}''(s) + K(s)x_{\beta}(s) = 0 \quad (2.27)$$

reaching the Hill's equation, which describes a quasi-harmonic oscillation. Then amplitude and phase depend on the particle position s in the accelerator¹⁵ with general solutions:

$$x_{\beta}(s) = \sqrt{\epsilon\beta(s)} \cos(\varphi(s) - \vartheta), \quad (2.28)$$

where $\beta(s)$ is determined by the focusing properties of the lattice, ϵ and ϑ are constants (from initial conditions) that determine a particular trajectory, $\varphi(s)$ is the *phase advance* of the oscillation between the point s_0 and point s in the lattice and defined as

$$\varphi(s) = \int_0^s \frac{d\bar{s}}{\beta(s)} \quad (2.29)$$

where $\beta(s)$ is known as the *betatron function*, describing completely the lateral focus properties of the guide field. The betatron oscillations in x or y are described by a pseudo-harmonic oscillator whose representative form is described in Equations 2.28 and 2.29. By its nature, $\beta(s)$ must always be positive and has an 'amplitude' and periodic correlations with the beam motion, see Figure 2.7.a.

As the Equation 2.27 is pseudo-harmonic, the electron experiences a lateral oscillation neither harmonic nor periodic. The movement is distorted sinusoidal-like wave with a variable amplitude ($\sqrt{\epsilon\beta}$), with 'phase' ($\varphi - \vartheta$) changing with s at a variable rate proportional to $1/\beta$. The nature of the movement is illustrated in Figure 2.7.b and Figure 2.7.c for different initial phases. Figure 2.7.d describe the electron path of many successive electron revolutions around a closed ring for some initial conditions ϵ and ϑ or for a bunch of electrons, where the amplitude-like characteristic of the betatron movement is always below a limit value $X(s)$ obtained by setting $\cos(\varphi - \vartheta) = 1$, such that

$$X_{\beta}(s) = \sqrt{\epsilon\beta(s)}, \quad (2.30)$$

where the trajectory of the electron fall within an *envelope* defined by $\pm X(s)$. The aperture required to contain an electron with a given oscillation amplitude varies around the accelerator as $X(s)$.

Finally, the total electron motion around the ideal orbit can be expressed as

$$x = x_{\epsilon} + x_{\beta} = \eta(s)\delta + \sqrt{\epsilon\beta(s)} \cos(\varphi(s) - \vartheta) \quad (2.31)$$

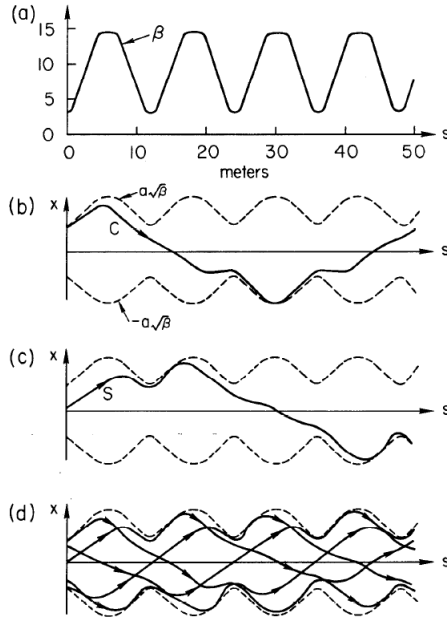


Figure 2.7: **Some beam trajectories with different initial conditions**⁵⁹. a) Betatron $\beta(s)$ function. b) Cosine-like trajectory for $s = 0$. c) Sine-like trajectory for $s = 0$. d) A particular trajectory after several revolutions.

2.3.6 Betatron trajectories

Starting with the same representative form as Equation 2.21,

$$x'' = -K(s)x, \quad (2.32)$$

which looks like the equation for the harmonic oscillator with spring 'constant' K . Depending on the value of K in a particular segment of s , the movement in x will have one of the forms⁵⁹

$$x = \begin{cases} a_1 \cos(\omega s) + a_2 \sin(\omega s) & \text{if } K > 0 \\ a_1 s + a_2 & \text{if } K = 0 \\ a_1 \cosh(\omega s) + a_2 \sinh(\omega s) & \text{if } K < 0 \end{cases} \quad (2.33)$$

Because Equation 2.32 is linear in x , any linear combination of cosine $C(s)$ and sine $S(s)$ functions will also describe a possible path. Then for any path:

$$x(s) = C(s, s_0)x_0 + S(s, s_0)x'_0, \quad (2.34)$$

$$x'(s) = C'(s, s_0)x_0 + S'(s, s_0)x'_0. \quad (2.35)$$

By using a matrix formalism, it turns to:

$$\mathbf{x}(s) = \mathbf{M}(s, s_0)\mathbf{x}(s_0), \quad (2.36)$$

where \mathbf{M} is the **Transfer Matrix (TM)** from s_0 to s , which depends only on the focusing property of the element in the guide field. For example, the TM for a segment¹⁶ from s_0 to $s_1 = s_0 + l$ with a constant K is

$$M(s_1, s_0) = \begin{cases} \begin{pmatrix} \cos(\sqrt{K}l) & \frac{1}{\sqrt{K}} \sin(\sqrt{K}l) \\ -\sqrt{K} \sin(\sqrt{K}l) & \cos(\sqrt{K}l) \end{pmatrix} & \text{if } K > 0 \\ \begin{pmatrix} 1 & l \\ 0 & 1 \end{pmatrix} & \text{if } K = 0 \\ \begin{pmatrix} \cosh(\sqrt{-K}l) & \frac{1}{\sqrt{-K}} \sinh(\sqrt{-K}l) \\ -\sqrt{-K} \sinh(\sqrt{-K}l) & \cosh(\sqrt{-K}l) \end{pmatrix} & \text{if } K < 0 \end{cases} \quad (2.37)$$

Moreover, the TM for any s interval can be written conveniently in terms of matrices for n segments (elements) of the interval, so for s_n segments between s_0 and s ¹⁵

$$M(s, s_0) = M(s, s_n)M(s_n, s_{n-1}) \dots M(s_1, s_0). \quad (2.38)$$

This is a widely used formalism for the calculation of solutions for equations of motion and experimental assembly in accelerator physics.

2.4 Beam Emittance

Some novel scientific applications and experimental methods can only be carried out in light facilities with high/ultra-high brightness. As mentioned before, while better the electron beam is collimated, the lower the emittance and the greater the brightness of the source. That is why the interest in building accelerators with smaller emittance.

2.4.1 Phase Space

Starting with the equation of motion for an electron inside the transport line and with initial condition $\vartheta = 0$,

$$x(s) = \sqrt{\epsilon\beta(s)} \cos(\varphi(s)), \quad (2.39)$$

whose derivative is

$$x'(s) = -\sqrt{\frac{\epsilon}{\beta(s)}} \left[\sin(\varphi(s)) - \frac{1}{2}\beta'(s) \cos(\varphi(s)) \right], \quad (2.40)$$

which can be written as

$$x'(s) = -\sqrt{\frac{\epsilon}{\beta(s)}} [\sin(\varphi(s)) + \alpha(s) \cos(\varphi(s))], \quad (2.41)$$

where

$$\alpha(s) = -\frac{1}{2}\beta'(s). \quad (2.42)$$

Considering a bunch of particles, the statistical moments of the beam are

$$\langle x^2 \rangle = \beta \langle \epsilon \cos^2(\varphi) \rangle = \epsilon_{RMS} \beta, \quad (2.43)$$

$$\langle x'^2 \rangle = \frac{1}{\beta} \langle \epsilon (\sin^2(\varphi) + \alpha^2 \cos^2(\varphi)) \rangle = \epsilon_{RMS} \frac{1 + \alpha^2}{\beta} = \epsilon_{RMS} \gamma, \quad (2.44)$$

$$\langle xx' \rangle = \langle \epsilon (\cos(\varphi) \sin(\varphi) + \alpha \cos^2(\varphi)) \rangle = \epsilon_{RMS} \alpha, \quad (2.45)$$

where $\langle \cos^2(\varphi) \rangle = \langle \sin^2(\varphi) \rangle = 1/2$, $\langle \cos(\varphi) \sin(\varphi) \rangle = 0$, and assuming a Gaussian particle distribution, $\epsilon/2 = \epsilon_{RMS}$ and

$$\gamma = \frac{1 + \alpha^2}{\beta}. \quad (2.46)$$

By squaring Equation 2.39 plus the square of the Equation 2.40 results in

$$\gamma x^2 + 2\alpha xx' + \beta x'^2 = \epsilon \quad (2.47)$$

which is exactly the equation of an ellipse in phase space for a single particle as depicted in Figure 2.8. The area enclosed by the ellipse is called the **emittance** ϵ of the beam quantified through:

$$\int_{\text{ellipse}} dx dx' = \pi \epsilon. \quad (2.48)$$

All the terms in the LHS of Equation 2.47 are not constant and depend on s , while in the RHS the ϵ term remain constant. In consequence, the ellipse shape and orientation is changing along the path but its area remains constant. In particular α, β, γ are known as **Twiss parameters** and help to determine the shape and orientation of the beam ellipse, where $\sqrt{\beta\epsilon}$ is the beam width, $\sqrt{\gamma\epsilon}$ is the beam divergence and α is how strong x and x' are correlated.

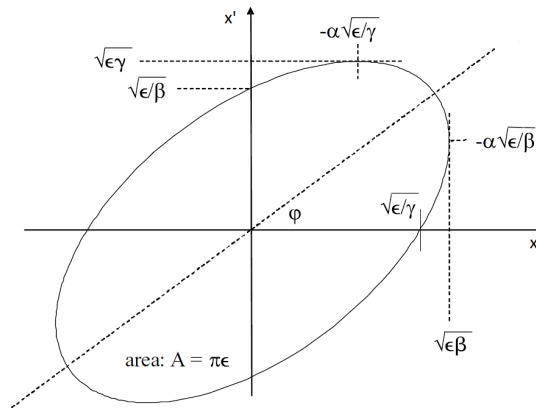


Figure 2.8: **Beam Phase Space Ellipse**¹⁵. (x, x') phase space coordinates for an electron moving in s direction. α, β, γ are Twiss parameters and determine the ellipse shape and orientation.

2.4.2 Beam Emittance

The phase space of an electron beam is usually composed of a bunch of particles distributed in the phase space. According to Liouville's Theorem¹⁵, which states that under the influence of conservative forces the particle density in the phase space remains constant, then the emittance is always the same throughout the path of the beam. Given a normalized distribution function $\rho(x, x')$ (see Figure 2.9) that satisfies $\int \rho(x, x') dx dx' = 1$, the statistical moments of the beam distribution for both x and x' are¹⁶:

$$\langle x \rangle = \int x \rho(x, x') dx dx', \quad (2.49)$$

$$\sigma_x^2 = \langle x'^2 \rangle = \int (x - \langle x \rangle)^2 \rho(x, x') dx dx', \quad (2.50)$$

$$\sigma_{xx'} = \langle xx' \rangle = \int (x - \langle x \rangle)(x' - \langle x' \rangle) \rho(x, x') dx dx' = r \sigma_x \sigma_{x'}, \quad (2.51)$$

where, σ_x and $\sigma_{x'}$ represent the RMS amplitude and divergence of the beam respectively and r is the correlation coefficient. According to equations 2.43, 2.44 and 2.45 by equivalence:

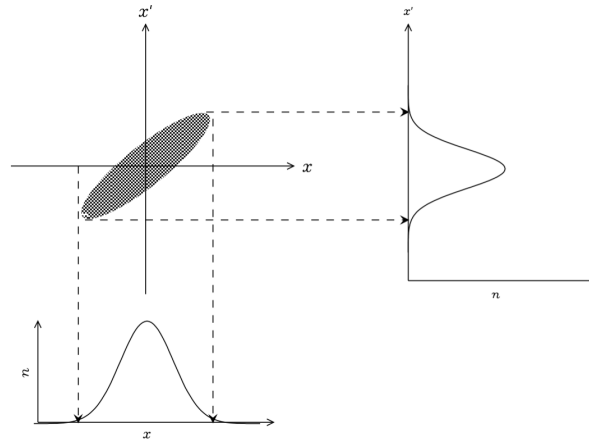


Figure 2.9: **Beam distribution in phase space**¹⁵. The beam distribution has a gaussian-like shape in x and x' planes.

$$\sigma_x = \sqrt{\epsilon_{RMS} \beta}, \quad (2.52)$$

$$\sigma_{x'} = \sqrt{\epsilon_{RMS} \gamma}, \quad (2.53)$$

$$\sigma_{xx'} = -\epsilon_{RMS} \alpha, \quad (2.54)$$

where the RMS area can be deduced as

$$\epsilon_{RMS} = \sqrt{\sigma_x^2 \sigma_{x'}^2 - \sigma_{xx'}^2} = \sigma_x \sigma_{x'} \sqrt{1 - r^2}. \quad (2.55)$$

Writing in matrix formalism leads to

$$\sigma = \begin{pmatrix} \sigma_x^2 & \sigma_{xx'} \\ \sigma_{xx'} & \sigma_{x'}^2 \end{pmatrix} = \begin{pmatrix} \sigma_{11} & \sigma_{12} \\ \sigma_{21} & \sigma_{22} \end{pmatrix} = \epsilon_{RMS} \begin{pmatrix} \beta & -\alpha \\ -\alpha & \gamma \end{pmatrix} \quad (2.56)$$

where

$$\det(\sigma) = \epsilon_{RMS}^2, \quad (2.57)$$

$$\sigma_{12} = \sigma_{21}. \quad (2.58)$$

Actually in accelerators, the emittance does not remain constant due to relativistic effects. However, the normalized emittance⁶⁰ is always constant and defined as

$$\epsilon_N = \beta_{rel} \gamma_{rel} \epsilon_{RMS}, \quad (2.59)$$

where β_{rel} and γ_{rel} are relativistic factors.

2.4.3 Phase space transformation

Since all the particles enclosed by a phase ellipse remain within the ellipse in order to describe the whole particle beam, it is only necessary to know how the parameters of the ellipse are transformed along the beam trajectory. The equation of the phase ellipse at the starting point $s = 0$ of the beamline can be stated as

$$\gamma_0 x_0^2 + 2\alpha_0 x_0 x_0' + \beta_0 x_0'^2 = \epsilon, \quad (2.60)$$

where any particle trajectory is transformed from the starting point $s = 0$ to any other point $s \neq 0$ using the formalism described in Equation 2.36, by transforming

$$\begin{pmatrix} x(s) \\ x'(s) \end{pmatrix} = \begin{pmatrix} C(s) & S(s) \\ C'(s) & S'(s) \end{pmatrix} \begin{pmatrix} x_0 \\ x_0' \end{pmatrix} = \begin{pmatrix} M_{11} & M_{12} \\ M_{21} & M_{22} \end{pmatrix} \begin{pmatrix} x_0 \\ x_0' \end{pmatrix} = M(P_1|P_0) \begin{pmatrix} x_0 \\ x_0' \end{pmatrix}. \quad (2.61)$$

Solving for x_0 and x_0' and replacing into Equation 2.60, and after ordering coefficients

$$\begin{aligned} \epsilon = & (M_{21}^2 \beta_0 - 2M_{21} M_{22} \alpha_0 + M_{22}^2 \gamma_0) x^2 \\ & + 2(-M_{11} M_{21} \beta_0 + M_{11} M_{22} \alpha_0 + M_{12} M_{21} \alpha_0 - M_{12} M_{22} \gamma_0) x x' \\ & + (M_{11}^2 \beta_0 - 2M_{11} M_{12} \alpha_0 + M_{12}^2 \gamma_0) x'^2. \end{aligned} \quad (2.62)$$

This equation can be rewritten in the form of Equation 2.60 noting that

$$\gamma = M_{21}^2 \beta_0 - 2M_{21} M_{22} \alpha_0, \quad (2.63)$$

$$\alpha = -M_{11} M_{21} \beta_0 + M_{11} M_{22} \alpha_0 + M_{12} M_{21} \alpha_0 - M_{12} M_{22} \gamma_0, \quad (2.64)$$

$$\beta = M_{11}^2 \beta_0 - 2M_{11} M_{12} \alpha_0 + M_{12}^2 \gamma_0. \quad (2.65)$$

The resulting ellipse equation at s still has the same area $\pi\epsilon$ but with different parameters γ, α, β . This new ellipse has a different orientation, shape and will continuously change along the transport beam line, but not its area. In the matrix formulation, the ellipse parameters, which are also called **Twiss parameters**, are transformed consequently as

$$\begin{pmatrix} \beta(s) \\ \alpha(s) \\ \gamma(s) \end{pmatrix} = \begin{pmatrix} M_{11}^2 & -2M_{11}M_{12} & M_{12}^2 \\ -M_{11}M_{21} & M_{11}M_{22} + M_{21}M_{12} & -M_{12}M_{22} \\ M_{21}^2 & -2M_{21}M_{22} & M_{22}^2 \end{pmatrix} \begin{pmatrix} \beta_0 \\ \alpha_0 \\ \gamma_0 \end{pmatrix} = M_{\sigma}(s, s_0) \begin{pmatrix} \beta_0 \\ \alpha_0 \\ \gamma_0 \end{pmatrix}. \quad (2.66)$$

Considering the ellipse evolution, the equation for a n-dimensional ellipse can be written in the form

$$u^T \sigma^{-1} u = 1, \quad (2.67)$$

where the symmetric matrix σ is still to be determined, u^T is the transpose of the coordinate vector u defined by

$$u = \begin{pmatrix} x \\ x' \\ y \\ y' \end{pmatrix}. \quad (2.68)$$

As in the 2D case, the evolution of the n-dimensional phase ellipse along a beam transport line is wanted. With $M(P_1|P_0)$ the matrix transformation from the point P_0 to P_1 , $u_1 = M(P_1|P_0)u_0$ is obtained and the phase ellipse equation at point P_1 leads to

$$(M^{-1}u_1)^T \sigma_0^{-1} (M^{-1}u_1) = u_1^T \sigma_1^{-1} u_1 = 1 \quad (2.69)$$

as $(M^T)^{-1} \sigma_0^{-1} M^{-1} = [M \sigma_0 M^T]^{-1}$ the beam matrix is finally transformed, therefore, as

$$\sigma_1 = M \sigma_0 M^T. \quad (2.70)$$

This formalism will be useful for the experimental determination of the beam emittance.

Chapter 3

Methodology

As previously mentioned, one of the main goals of SIRIUS is to determine if the beam characteristics at the LINAC exit meet the requirements for its injection into the Booster. In this chapter, an experimental and computational mechanism to measure both the energy and the normalized emittance of the beam is described. On the other hand, CLEAR seeks to characterize the new BASLER camera and compare it with the standard BTV camera, to test if it represents significant improvements in data acquisition (triggering the beam) I will measure the normalized beam emittance using these two cameras. As can be seen, for both SIRIUS and CLEAR the same experimental mechanisms will be used with slight modifications.

3.1 Measurement of beam Emittance and Twiss Parameters

Experimentally thanks to the help of a OTR monitor, the beam size can be measured, but not beam divergence. Remember that beam emittance is a measure of both beam size and beam divergence. Unfortunately, the beam divergence cannot be measured directly and thus beam emittance. However, by manipulating the orientation and shape of the beam phase ellipse in a controlled and measurable way gives a tool to experimentally determine the Twiss parameters. For example, if the beam size is measured under different locations or under different quadrupole focusing conditions with the same initial conditions, see Fig. 3.1.

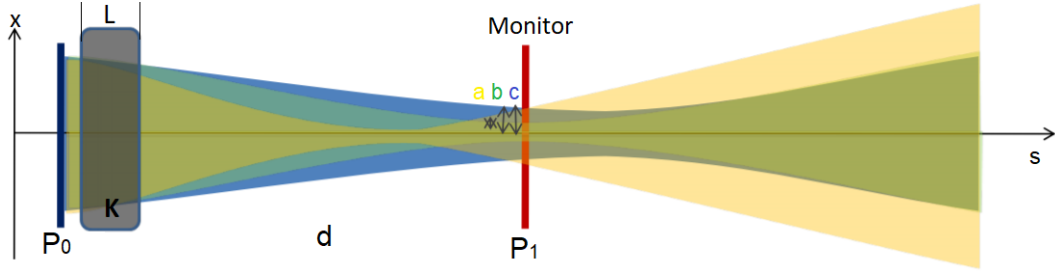


Figure 3.1: **Set-up for emittance measurement at LINAC exit of SIRIUS, sector 02.** Varying the current of the quadrupole, the quadrupole strength will change to have a different focusing condition.

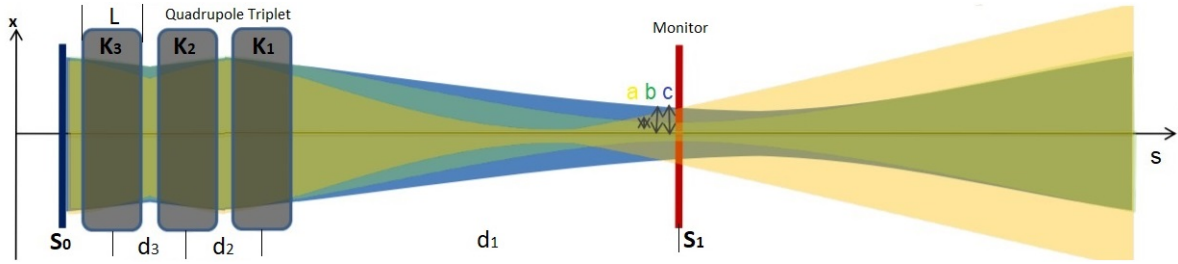


Figure 3.2: **Set-up for emittance measurement at CLEAR.** Varying the current of any quadrupole of the quadrupole triplet to have a different focusing condition.

3.1.1 Transfer Matrix Method

The Figure 3.1 represents an elect beam moving in the s direction, which passes through a point P_0 and then crosses a quadrupole set-up being focused on a OTR monitor located at P_1 , which measures the size of the beam. Making several measurements under different focusing conditions (varying the quadrupole current) will create an experimental mechanism to know the moments of the beam before crossing the quadrupole in the reference point P_0 .

In this way Equation 2.70 sets the starting point

$$\begin{pmatrix} \sigma_{1,11} & \sigma_{1,12} \\ \sigma_{1,21} & \sigma_{1,22} \end{pmatrix} = \begin{pmatrix} M_{11} & M_{12} \\ M_{21} & M_{22} \end{pmatrix} \begin{pmatrix} \sigma_{0,11} & \sigma_{0,12} \\ \sigma_{0,21} & \sigma_{0,22} \end{pmatrix} \begin{pmatrix} M_{11} & M_{21} \\ M_{12} & M_{22} \end{pmatrix}, \quad (3.1)$$

where the components of the M matrix are those described in Equation 2.37 for different focusing forces. So, the size of the beam $\sigma_{i,11}$ on the P_i site is

$$\sigma_{i,11} = M_{11}\sigma_{0,11} + 2M_{11}M_{12}\sigma_{0,12} + M_{12}^2\sigma_{0,22} = \begin{pmatrix} M_{11}^2 & 2M_{11}M_{12} & M_{12}^2 \end{pmatrix} \begin{pmatrix} \sigma_{0,11} \\ \sigma_{0,12} \\ \sigma_{0,22} \end{pmatrix}. \quad (3.2)$$

Note that the analysis will done only using the element $\sigma_{i,11}$ because it represents the measurement of the beam

size. These measurements are in function of the quadrupole strength $K(I)$, which in turn, depends on its current I . Then, experimentally the quadrupole strength is changed depending on the current administered in the quadrupole, and is equivalent to perform measurements in different locations. Expressing the results for n different beam size measurements

$$\begin{pmatrix} \sigma_{1,11} \\ \sigma_{2,11} \\ \vdots \\ \sigma_{n,11} \end{pmatrix} = \begin{pmatrix} M_{1,11}^2 & 2M_{1,11}M_{1,12} & M_{1,12}^2 \\ M_{2,11}^2 & 2M_{2,11}M_{1,12} & M_{2,12}^2 \\ \vdots & \vdots & \vdots \\ M_{n,11}^2 & 2M_{n,11}M_{n,12} & M_{n,12}^2 \end{pmatrix} \begin{pmatrix} \sigma_{0,11} \\ \sigma_{0,12} \\ \sigma_{0,22} \end{pmatrix} = M_{\sigma,n} \begin{pmatrix} \sigma_{0,11} \\ \sigma_{0,12} \\ \sigma_{0,22} \end{pmatrix}. \quad (3.3)$$

The solution at P_0 , from simple matrix multiplications, which represent the pseudoinverse of $M_{\sigma,n}$ or its equivalent least squares¹⁶, is

$$\begin{pmatrix} \sigma_{0,11} \\ \sigma_{0,12} \\ \sigma_{0,22} \end{pmatrix} = (M_{\sigma,n}^T M_{\sigma,n})^{-1} M_{\sigma,n}^T \begin{pmatrix} \sigma_{1,11} \\ \sigma_{2,11} \\ \vdots \\ \sigma_{n,11} \end{pmatrix}. \quad (3.4)$$

An experimental procedure that allows to determine the emittance of the beam through various measurements of beam sizes depending on the quadrupole strength has been derived.

3.1.2 Thin lens approximation

A more simplified arrangement consists of a single quadrupole and a screen/monitor at a distance d . Assuming that the length L and the strength of the quadrupole K are such that $1/f = KL \ll 1$, a thin lens approximation¹⁶ can be used and the total TM from the point P_0 to P_1 (using the LINAC of SIRIUS as reference, Fig. 3.1) would be

$$M = M_d M_q = \begin{pmatrix} 1 & d \\ 0 & 1 \end{pmatrix} \begin{pmatrix} 1 & 0 \\ -1/f & 1 \end{pmatrix} = \begin{pmatrix} 1 - d/f & d \\ -1/f & 1 \end{pmatrix}, \quad (3.5)$$

where M_d is the transfer matrix in drift space and M_q is the transfer matrix of the quadrupole as a thin lens. The eqn. 3.2 becomes

$$\sigma_{1,11}(K) = (1 - dLK)^2 \sigma_{0,11} + 2(1 - dLK)d\sigma_{0,12} + d^2 \sigma_{0,22} \quad (3.6)$$

and rearranging terms it becomes quadratic with respect to K ,

$$\sigma_{1,11}(K) = (d^2 L^2 \sigma_{0,11}) K^2 - 2(dL\sigma_{0,11} + d^2 L\sigma_{0,12})K + (\sigma_{0,11} + 2d\sigma_{0,12} + d^2 \sigma_{0,22}). \quad (3.7)$$

Fitting the n measurements of beam size $\sigma_{n,1,1}(K)$ by a parabola ($aK^2 + bK + c$) allows to determine the full beam matrix σ_0 as

$$\sigma_{0,11} = \frac{a}{d^2 L^2}, \quad (3.8)$$

$$\sigma_{0,12} = \frac{-b - 2dL\sigma_{0,11}}{2d^2 L}, \quad (3.9)$$

$$\sigma_{0,22} = \frac{c - \sigma_{0,11} - 2d\sigma_{0,12}}{d^2}. \quad (3.10)$$

With this measurement a complete set of initial beam parameters ($\alpha_0, \beta_0, \gamma_0, \epsilon$) can be obtained and now the beam parameters can be calculated at any point along the transport line or for injection into the Booster.

In addition, for the case of CLEAR a quadrupole triplet is used to calculate the beam emittance, see Figure 3.2. Then, the transfer matrix would be

$$M = M_{d1} M_{q1} M_{d2} M_{q2} M_{d3} M_{q3} = \begin{pmatrix} 1 & d_1 \\ 0 & 1 \end{pmatrix} \begin{pmatrix} 1 & 0 \\ -K_1 L & 1 \end{pmatrix} \begin{pmatrix} 1 & d_2 \\ 0 & 1 \end{pmatrix} \begin{pmatrix} 1 & 0 \\ -K_2 L & 1 \end{pmatrix} \begin{pmatrix} 1 & d_3 \\ 0 & 1 \end{pmatrix} \begin{pmatrix} 1 & 0 \\ -K_3 L & 1 \end{pmatrix}, \quad (3.11)$$

where the first left matrix M_{d1} is the first drift matrix when looking upstream from the screen, the next is the transfer matrix of the quadrupole as a thin lens and so on. Therefore, the same approximations to calculate the beam emittance can be used.

3.2 Error propagation and uncertainties

For each i 'th quad scan measurement there is an equivalent transfer matrix $M(i)$, RMS beam size $\sigma(i)$, and standard error of the mean of the beam size $\delta\sigma(i)$. Also, To calculate the error in the emittance and Twiss parameters, there are several ways. One is using error propagation⁶¹ of a function $g(x_1, x_2, \dots, x_n) = \epsilon(\sigma_{0,11}, \sigma_{0,12}, \sigma_{0,22})$:

$$\sigma^2(g) = \sum_{i=1}^n \left(\frac{\partial g}{\partial x_i} \right) \sigma_{x_i}^2 + \sum_{i=1}^n \sum_{j=1, j \neq i}^n \frac{\partial g}{\partial x_i} \frac{\partial g}{\partial x_j} \text{cov}(i, j). \quad (3.12)$$

Another way⁶² is calculating:

$$\sigma^2(f) = (\nabla_{x_i} f)^T C (\nabla_{x_i} f) = \begin{pmatrix} \sigma_\beta^2 & \dots & \dots \\ \dots & \sigma_\alpha^2 & \dots \\ \dots & \dots & \sigma_\epsilon^2 \end{pmatrix}, \quad (3.13)$$

where C is the variance matrix and $f = (\beta, \alpha, \epsilon)$

Another method to calculate the emittance error using the quadratic fit⁶³ is obtained from the covariance matrix produced when performing parabolic fits with the beam sizes:

$$\sigma^2(aK^2 + bK + c) = \begin{pmatrix} \sigma_a^2 & \dots & \dots \\ \dots & \sigma_b^2 & \dots \\ \dots & \dots & \sigma_c^2 \end{pmatrix}. \quad (3.14)$$

Finally, the beam data uncertainty obtained at SIRIUS and CLEAR can be treated through **Monte Carlo error propagation**⁶⁴. The idea behind the Monte-Carlo technique is to generate many possible solutions of the emittance and Twiss parameters, each time varying the input data (beam size σ) randomly within their stated limits of precision ($\delta\sigma$). Using the results to look at the overall results. This method will be used in this work to calculate uncertainties.

3.3 Statistical data analysis

To compare the estimates from the two cameras is necessary to compare the two means and the two variances. First, it necessary test if the two distributions have the same variance. To test this hypothesis, a F -test of two variances⁶⁵ is performed taking into account that the populations are approximately normally distributed and independent of each other as follow: Let X_1, X_2, \dots, X_n be a random sample of a distribution $N(\mu_1, \sigma_1^2)$ and Y_1, Y_2, \dots, Y_n a random sample of a distribution $N(\mu_2, \sigma_2^2)$ and independent of each other. An estimator to test the hypothesis $H_0 : \sigma_1^2 = \sigma_2^2$ is

$$f = \frac{s_1^2}{s_2^2}. \quad (3.15)$$

If the ratio of the sample variances f is between 0.5 and 2 (one variance is no more than double the other) the assumption of equality of population variances is reasonable.

After calculate if two distributions have or not the same variance a t -test is useful to determine if the two distributions are statistically the same (Null hypothesis). A t -test⁶⁶ is especially useful in the case of time series data to assess a 'before and after' comparison of some system to see if there has been effect. Difference in terms of significance is given as follow: Let X_1, X_2, \dots, X_n be a random sample of a distribution $N(\mu_1, \sigma_1^2)$ and Y_1, Y_2, \dots, Y_n a random sample of a distribution $N(\mu_2, \sigma_2^2)$ and independent of each other. Let $\bar{X} - \bar{Y}$ with distribution $N(\mu_1 - \mu_2, S_p^2)$, an estimator to test the hypothesis $H_0 : \mu_1 - \mu_2 = \Delta_0$ for significantly equal variances is

$$t = \frac{\bar{X} - \bar{Y} - \Delta_0}{S_p \sqrt{\frac{1}{n_1} + \frac{1}{n_2}}}, \quad (3.16)$$

where

$$S_p^2 = \frac{(n_1 - 1)s_1^2 + (n_2 - 1)s_2^2}{n_1 + n_2 - 2}. \quad (3.17)$$

On the other hand, for significantly different variances, the t -test statistic is

$$t = \frac{\bar{X} - \bar{Y} - \Delta_0}{\sqrt{\frac{s_1^2}{n_1} + \frac{s_2^2}{n_2}}}. \quad (3.18)$$

If the two distributions of the means are the same, the distribution of the difference would be roughly centered at zero⁶⁷, $\Delta_0 = 0$. In addition, to reject the null hypothesis a significance level of $\alpha = 0.05$ is used.

3.4 Beam Energy Measurement

The beam energy is measured using a spectrometer which bend the electron beam an angle of $\theta = 45^\circ$, as in Figure 3.3, where electrons with different energy enter in a different orbit due to energy spread, see Figure 3.3.a. Later, electrons collide with a OTR screen that emits perpendicular OTR radiation towards a beam profile monitor which record the beam sizes.

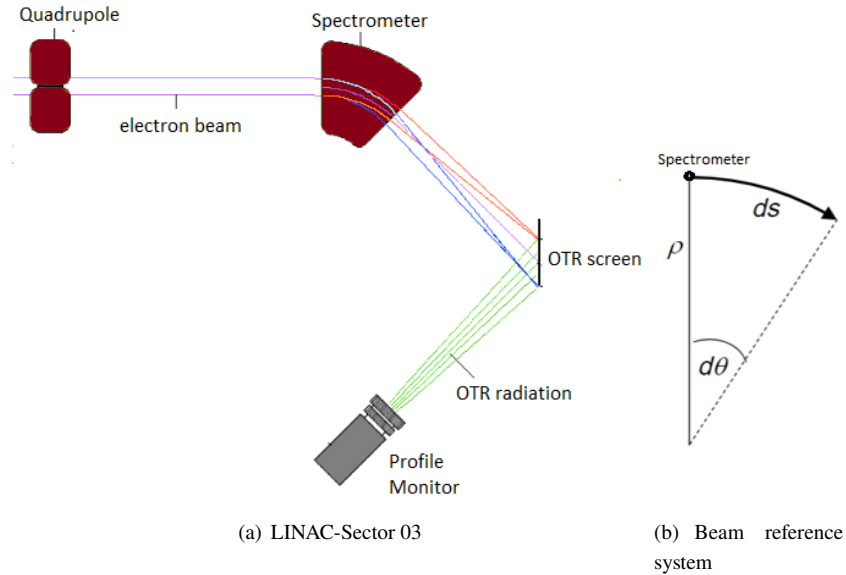


Figure 3.3: **Experimental set-up for Energy and Dispersion measurement, LINAC-Sector 03.** The spectrometer bends the beam 45° through a OTR screen to emit the OTR radiation towards a profile monitor/camera.

The electron beam motion after the spectrometer is

$$d\theta = \frac{ds}{\rho(s)} = \frac{eB(s)}{P_0} ds, \quad (3.19)$$

where ρ is the spectrometer radius and P is the momentum of the beam. Integrating both sides,

$$\theta = \frac{e \int B(s) ds}{P_0}. \quad (3.20)$$

Finally, after arrange terms, the equation describing the nominal beam energy is

$$P_0 = \frac{BL}{\theta} e, \quad (3.21)$$

where $BL = \int B(s) ds$ is the "integrated magnetic field" which can be obtained through the measurement of the excitation curve of the spectrometer (dependence of magnetic field under a certain current).

Using the fact that

$$\frac{x_\epsilon}{\eta} = \frac{\Delta E}{E_0} \approx \frac{\Delta P}{P_0}, \quad (3.22)$$

the electron momentum is

$$P = P_0 + \Delta P = P_0 \left(1 + \frac{x_\epsilon}{\eta} \right) \quad (3.23)$$

and the electron energy is

$$E^2 = E_0^2 + P^2 c^2. \quad (3.24)$$

For a electron beam, the energy spread can be calculated from the expectation value of x_ϵ as

$$\sigma_\epsilon^2 = \langle x_\epsilon^2 \rangle = \langle (\eta\delta)^2 \rangle = (\eta\sigma_\delta)^2. \quad (3.25)$$

After simplification, the energy spread is

$$\sigma_\delta \approx \frac{\sigma_\epsilon}{\eta}. \quad (3.26)$$

3.5 Software Implementations

In order to characterize the electron beam of LINAC exit at SIRIUS and assess performances of the newly commissioned Basler 620 imaging system at CLEAR and comparing the results with the standard BTV system, new PYTHON-based quad-scan and emittance calculator tool scripts were implemented for each case. In the case of SIRIUS, the script is used to measure the Emittance and Twiss parameters to do beam dynamics at the Booster entrance.

3.5.1 CLEAR Software Set-up

In order to assess performances of the newly commissioned Basler 620 imaging system and uses it for emittance measurements, comparing the results with the ones obtained with the standard BTV system, two PYTHON-based scripts were implemented, one data acquisition script and one data analysis script with 5 main modules. These scripts are uploaded in the CLEAR GitLab*.

Data Acquisition Script

This first script (`get_data.py`) script is responsible for extracting beam images at the same time using both Basler and BTV 620 cameras, using Java API for Parameter Control (JAPC)⁶⁸ as main resource. JAPC is a framework to design Java applications that manipulate accelerator components⁶⁸. It can be seen as a parameter which represents a control value of any device property, physical equipment, databases, timing events, and others. Client programs can easily check and modify the status of JAPC parameters with **get** and **set** functions:

- `getParam(parameterName, getHeader=False, unixtime=False, **kwargs)`
- `setParam(parameterName, parameterValue, checkDims=True, **kwargs)`.

Then, they can subscribe for automatic notification of its value changes:

- `startSubscriptions(parameterName=None)`
- `stopSubscriptions(parameterName=None)`
- `subscribeParam(parameterName, onValueReceived=None, **kwargs)`

This first script uses JAPC for two specific tasks. First, set a specific current in the quadrupole scan; second, get 10 beam images using both cameras at the same time after setting the desired current, see Figure 3.4. Where the parameter names takes the following form

- `parameterName = device / property [# field]`

Data Analysis Script

This second script (`analyze_data.py`) is responsible for analyzing the data obtained with the Basler and BTV cameras and is made of 5 main modules:

1. **Fit Data.** This module takes the beam images and perform gaussian fittings of the beam in both planes, horizontal and vertical of both cameras BTV (see Figure 3.5.a) and Basler (see Figure 3.5.b), to return the beam sizes mean (σ_x and σ_y) and the standard error of the mean per each current.

*https://gitlab.cern.ch/CLEAR/Digital_BTV_tester

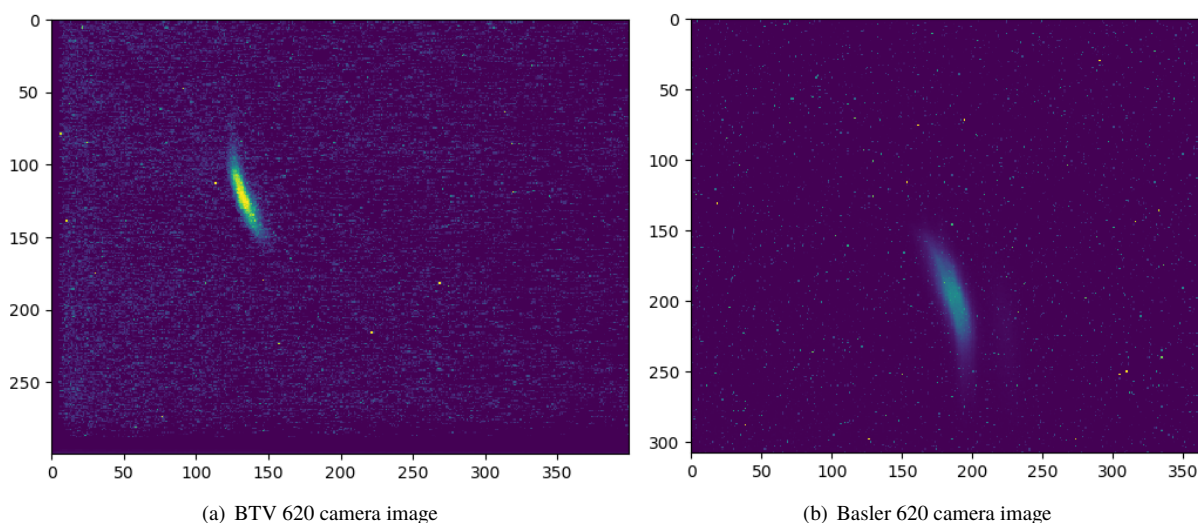


Figure 3.4: **Beam images for 620 BTV and Basler cameras.** Under a certain quadrupole current, the image from the Basler cameras presents better quality images as reduced noise and better resolution.

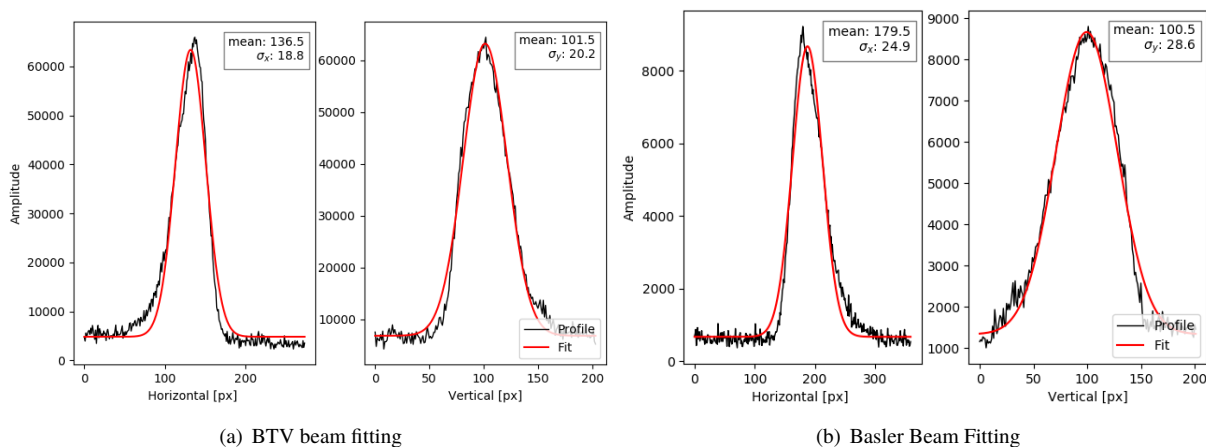


Figure 3.5: **Beam Fittings for BTV and Basler cameras.** Example of beam size fittings using the script done for vertical and horizontal planes.

2. **Twiss Parameters and Emittance Calculation.** This module uses the beam mean sizes obtained after the fittings and the current of each quadrupole of the triplet. Using the currents, it's possible to calculate the transfer matrix between S_0 and S_1 , see Figure 3.2. Then, the module calculates the pseudo-inverse of the transfer matrix and it multiplies with the beam sizes obtained in the fitting, see Equation 3.4. After the multiplication, the components of the sigma matrix at S_0 ($\sigma_{0,11}$, $\sigma_{0,12}$, $\sigma_{0,22}$) are obtained. With this values is easily to calculate Twiss parameters (see Equation 2.56) and normalized emittance (see Equation 2.59).

3. **Error Calculations.** This module propagates uncertainties with a Monte-Carlo method by doing the following:

- Generate randomly sample values of σ at each different quadrupole set current, $N = 10000$ times, using σ mean and $\delta\sigma$ mean:

```
sigma = random.normal(sigmastat[i], error[i], N)
```

- Compute the Twiss parameters and beam emittance for each set of values:

```
emittance, beta, alpha, gamma = twiss(I1, I2, I3, sigma)
```

4. **Statistical Analysis.** This module tests the hypothesis that the estimated normalized emittance for both cameras are actually correct and if they come from the same event doing the following:

- Perform the F -test for the normalized emittance distributions for the BTV and Basler cameras :

```
f = F_test(emittance_BTV, emittance_BASLER)
```

- Using the f value perform the t -test:

```
t, p = t_test(emittance_BTV, emittance_BASLER, f)
```

This module also plots the difference between the BTV and Basler normalized emittance distributions, see Figure 3.6. In addition, it calculates useful information as the mean μ , the standard deviation of the mean σ_μ and the area a between one tail and zero (shaded region).

5. **Dynamic Range Analysis.** This module tests the emittance and Twiss parameters results for different dynamic ranges of quadrupole currents.

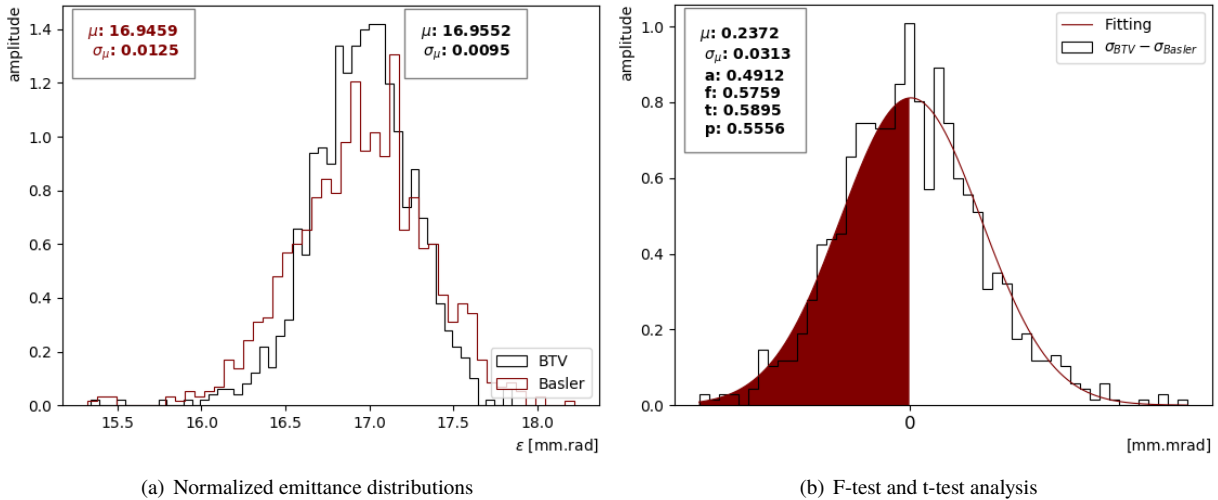


Figure 3.6: **t-test using the Basler and BTV results.** The normalized emittance distributions for both cameras presents quite similar distributions with a p -value bigger than the acceptance level.

3.5.2 SIRIUS Software Set-up

This software for SIRIUS data is basically the same that the CLEAR software with small adaptations as sorted below.

1. **Data Acquisition.** This first module is responsible for extract the beam images creating a software connection between the profile monitor installed in the sector-02 and sector-03 at the LINAC exit and the control room PCs. The beam images coming from the profile monitor are plotted using a *PyDMImageView* widget⁶⁹, see Figure 3.7. This module operates for the two modes of LINAC operation.

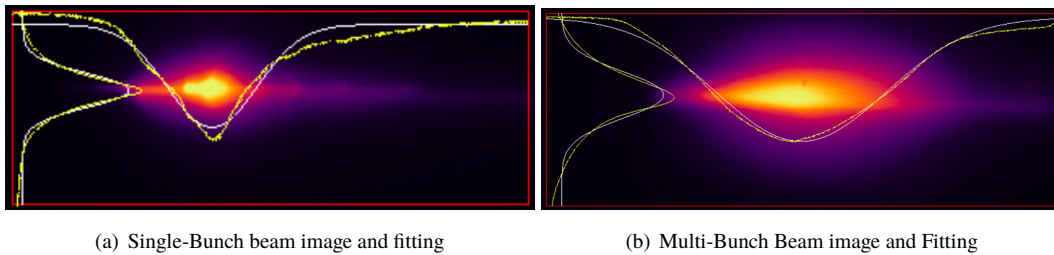


Figure 3.7: **Beam images coming from the profile monitor.** The script perform gaussian beam fittings in horizontal and vertical planes over the beam images for the two modes of LINAC operationm.

2. **Data Analysis.** This module takes the beam images and performs gaussian fittings of the beam simultaneously in both planes, horizontal and vertical (see Figure 3.7) and store the beam mean sizes (σ_x and σ_y) for future calculations.
3. **Energy measurement.** This module measure the beam energy and energy spread of the beam using the beam mean sizes coming from the data analysis module. This module also uses *PyDMImageView* widget to plot the energy and energy spread.
4. **Twiss Parameters and Emittance Calculation.** This modules is also coupled with the data analysis module using the beam mean sizes obtained after the fittings and their corresponding quadrupole currents. Using the quadrupole current, its possible to calculate the transfer matrix between S_0 and S_1 for one quadrupole set-up. Then, Twiss parameters and normalized emittance are calculated using the same procedure as in the CLEAR software.
5. **Error Calculations.** This module calculates the errors for the beam emittance and Twiss parameters using Monte-Carlo method.
6. **Statistical Analysis.** This modules tests the hypothesis that the estimated normalized emittance and Twiss parameters for both Transfer method and Thin lens method are actually significantly the same using the t -test described before.

Chapter 4

Results & Discussion

In this chapter the beam energy, beam energy spread, normalized emittance and the Twiss parameters results will be presented in two different sections. First, the results obtained in the SIRIUS LINAC will be addressed. Then, the results of the new optical diagnostic system of CLEAR will be presented and discussed.

4.1 Beam dynamics with first data of the LINAC of SIRIUS*.

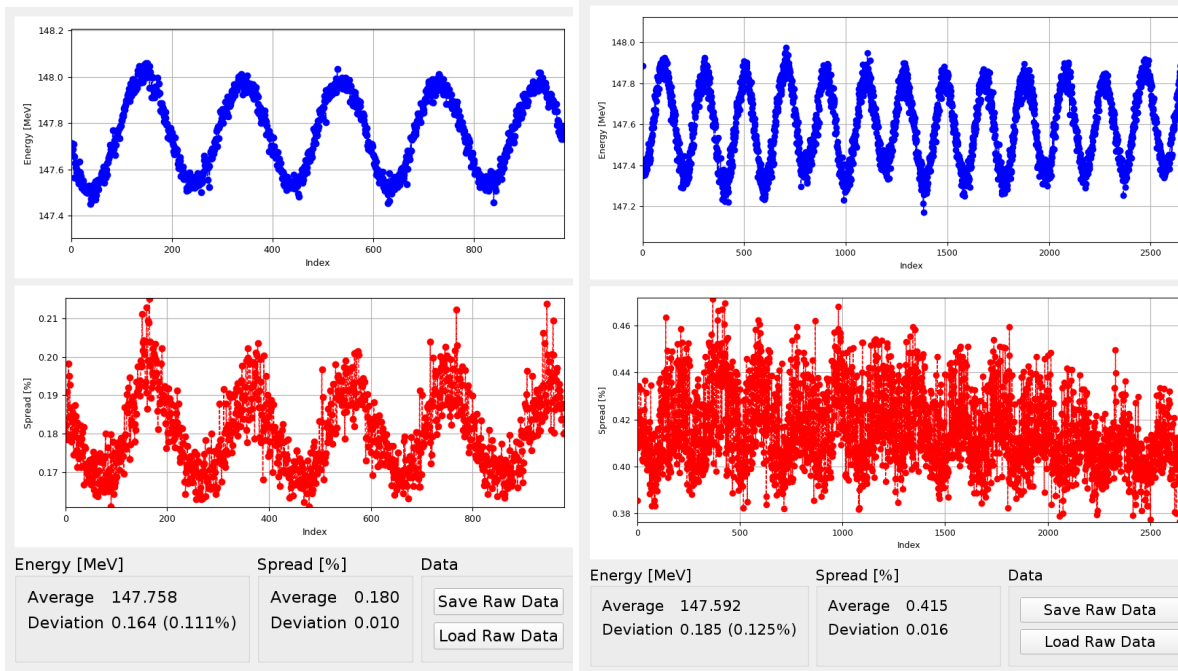
The beam dynamics studies are addressed in this section from first measurements of beam energy, beam energy spread and beam emittance at the LINAC exit for the Single-bunch mode and Multi-bunch mode of SIRIUS.

4.1.1 Beam energy and beam energy spread results

The beam energy and energy spread are firstly calculated as inputs for the normalized emittance calculation. By using the experimental procedure described in Chapter 3, the energy and energy spread are plotted in Figure 4.1 for the two LINAC operation modes, where each 'index' represents the energy and energy spread for one beam size measurement at certain dipole current. For the Single-bunch mode, an energy $E = 147.8 \pm 0.2$ MeV was obtained with an energy spread percentage $\sigma_\delta = 0.18 \pm 0.01$ %. The energy uncertainty only represents the 0.1% of the total energy. For the Multi-bunch mode, an energy $E = 147.6 \pm 0.2$ MeV was obtained with an energy spread percentage

*These results were performed under supervision and collaboration with FAC group of SIRIUS

$\sigma_\delta = 0.41 \pm 0.02 \%$. The energy uncertainty in this case indicates again the 0.1% of the total energy. When looking for the energy spread of the multi-bunch mode, it is only 0.09 % below the maximum acceptance value ($\sigma_\delta = 0.5 \%$).



(a) Single-Bunch results for energy and energy spread

(b) Multi-Bunch energy results for energy and energy spread

Figure 4.1: **Beam energy and energy spread results.** For the Single-bunch mode and Multi-bunch mode at the LINAC exit, the E and σ_δ results are oscillating around the mean value due to thermal effects.

The oscillating effect in both energy and energy spread are attributed to temperature fluctuations (thermal expansion) in the accelerating structure which is periodically being cooled. Another fundamental requirement for a correct LINAC commissioning is temperature fluctuations have to be close to zero, to avoid these kind of oscillating effect in the energy and energy spread.

4.1.2 Normalized beam emittance and Twiss parameters results

Based on methodology described in Chapter 3, by using the beam energy and the quad-scan carried out in the last quadrupole at the LINAC exit, the first normalized emittance and Twiss parameters results are calculated for the horizontal plane and vertical planes for the single and multi-bunch modes of the LINAC.

Single-bunch mode results:

As can be seen in the Figure 4.2, the beam sizes as function of the quadrupole current (I) for Single-Bunch mode are presented. As seen, the beam size in the horizontal and vertical planes generates a pronounced parabola as a function of the quadrupole current. For the vertical plane the uncertainties tend to be greater than in the horizontal plane. This increase in the uncertainty for high current values can be explained due to the change in direction of the quadrupole current at the time of quad-scan. Ideally, the focusing quadrupole on the vertical plane should ideally operate only with "negative" currents.

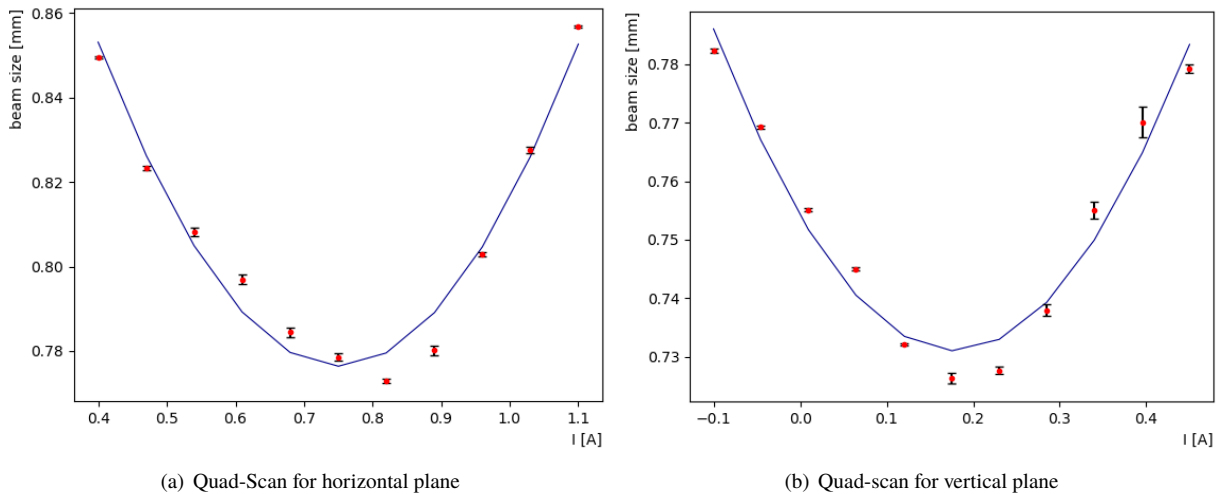


Figure 4.2: **Quad-scan beam fitting for Single-bunch mode.** For vertical and horizontal plane the beam size is quadratic as function of quadrupole current. $E = 147.8$ MeV at SIRIUS LINAC.

From the beam sizes with their respective uncertainties, through the mechanism of Transfer Matrix (TM) or the Thin Lens (TL) approximation, Twiss parameters and the normalized emittance are obtained. By Monte-Carlo error propagation, the uncertainties of normalized emittance and Twiss parameters are estimated and shown in Figure 4.3.

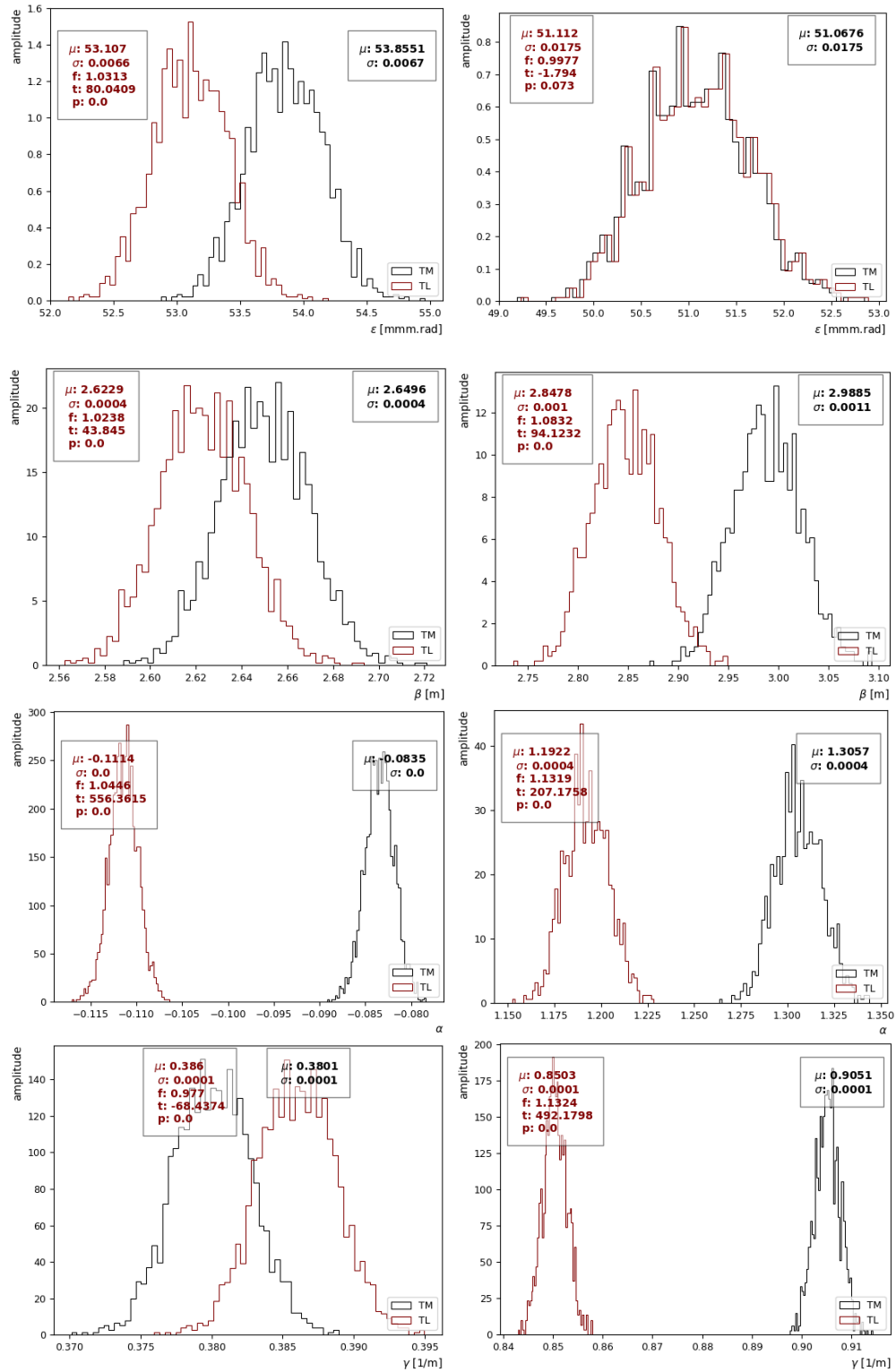


Figure 4.3: **Normalized emittance and Twiss parameters distributions.** Monte Carlo error propagation results for horizontal plane (left) and vertical plane (right). Single Bunch mode at $E = 147.7$ MeV

Although, the normalized emittance distributions are a global combination of Twiss parameters observe how in the vertical plane for both methods (TM or TL) have quite similar distributions centered almost in the same position despite the fact that their beam size uncertainties are relatively large, see first row of Figure 4.3. Assessed in the vertical plane, the TM method gives a $\epsilon_N = 51.07 \pm 0.02$ mm.mrad and in the TL method a $\epsilon_N = 51.11 \pm 0.02$ mm.mrad. On the other hand, for the horizontal plane, the ϵ_N distributions are not centered in the same position but very close within their uncertainties. For the TM method a $\epsilon_N = 53.855 \pm 0.007$ mm.mrad and for the TL method a $\epsilon_N = 53.107 \pm 0.007$ mm.mrad were obtained.

The fact that ϵ_N distributions for the vertical plane are quite similar, give a strong evidence that they are statistically the same. When applied the f -test, it gives a value of $f = 0.9977$, that is so close to 1 and inside the range of assumption of equality of population variance. With this information, the t -test gives $t = 0.7723$ which corresponds to $p=0.44$, that is bigger than the significance level $\alpha = 0.05$. Then, the null hypothesis cannot be rejected concluding that the two distribution are statistically the same. However, for the horizontal plane a value of $f = 1.013$ is obtained and corresponds population equal variances, but the t -test gives a $t = 80.040$ that corresponds a p value so close to zero, meaning that the both distributions are significantly different. These last result comes from the uncertainties in the beam sizes, betatron oscillations mostly presented in the horizontal plane and also by the fact that TL method is just an approximation of the TM method.

When the f -test is applied to Twiss parameters β , α and γ , the distributions are not equally centered. First, note how in all the distributions the f -value fall in the region to validate equal variances, but the corresponding t -values are very large, giving a p -value close to zero meaning significantly different distributions. These results also comes from the same reasons giving before. An interested observation is that in most cases the f -value is little bigger than 1 meaning that uncertainties for the TL distributions are lower than TM distributions.

Regarding the normalized emittance required for the correct injection into the Booster, they must be around 50 mm.mrad in both planes. In the horizontal plane a normalized emittance around 53 mm.rad and for the vertical plane a normalized emittance around 51 mm.rad were obtained. These two normalized emittance values are very close to the 50 mm.mrad required that can be easily corrected for example by using Orbit Corrector Magnets⁷⁰.

Multi-bunch mode results:

In Figure 4.4 the beam sizes as function of the quadrupole current for the Multi-bunch mode are presented. As seen in the Single-bunch quad-scan, the beam size as a function of the quadrupole current generates a pronounced parabola in both planes. In the multi-bunch mode, the uncertainties associated to the beam size are lower than the single bunch mode due to the quad-scan for both planes was performed in their respective direction of quadrupole current.

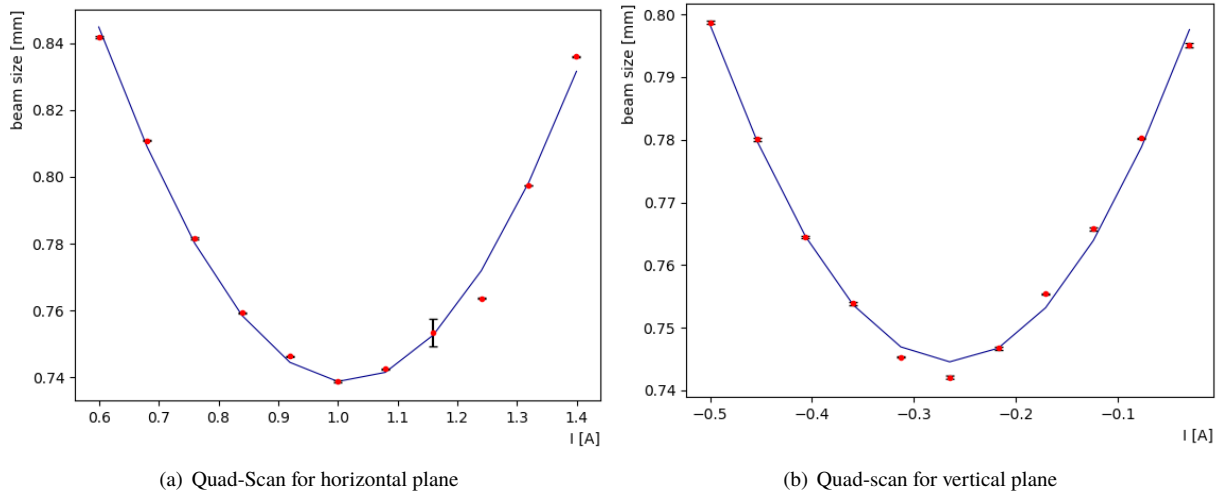


Figure 4.4: **Quad-Scan beam fitting for Multi-Bunch mode.** For vertical and horizontal plane the beam size is quadratic as function of quadrupole current. $E = 147.80$ MeV.

Again, as for the Single-bunch mode, the ϵ_N distributions for both calculation methods have greater similarities, both in the average and in the uncertainty, see Figure 4.9. With respect to the emittance in the horizontal plane both calculation methods yield very close values between each one with a similar uncertainty distribution.

In the horizontal plane, for the TL method a normalized emittance $\epsilon_N = 49.813 \pm 0.005$ mm.rad and for the TM method a $\epsilon_N = 50.747 \pm 0.005$ mm.mrad are obtained. These two normalized emittance values are extremely close to the 50 mm.mrad required. Also, doing the f -test a $f = 1.0194$ is obtained meaning equal variances and TL uncertainty lower than TM. As in the previous case for this plane its large t -value corresponds a p -value close to zero, which means different distributions.

For the vertical plane, the following normalized emittance values were obtained: $\epsilon_N = 61.560 \pm 0.007$ mm.mrad for TL method and $\epsilon_N = 61.567 \pm 0.007$ mm.mrad for TM method. In this case, the values of normalized emittance are not closer to the 50 mm radius necessary for the injection into the Booster. Then, more significant corrections are required. It is supported since, a $f = 1.0002$ and $t = 0.7723$ are achieved and correspond to $p = 0.44$ bigger than the significance level $\alpha = 0.05$. This p -value correspond a highly equal distributions. Checking the distributions of Twiss parameters at both planes, all of them are statistically different except β -distributions with $t = 0.9479$, which correspond to $p = 0.3432$.

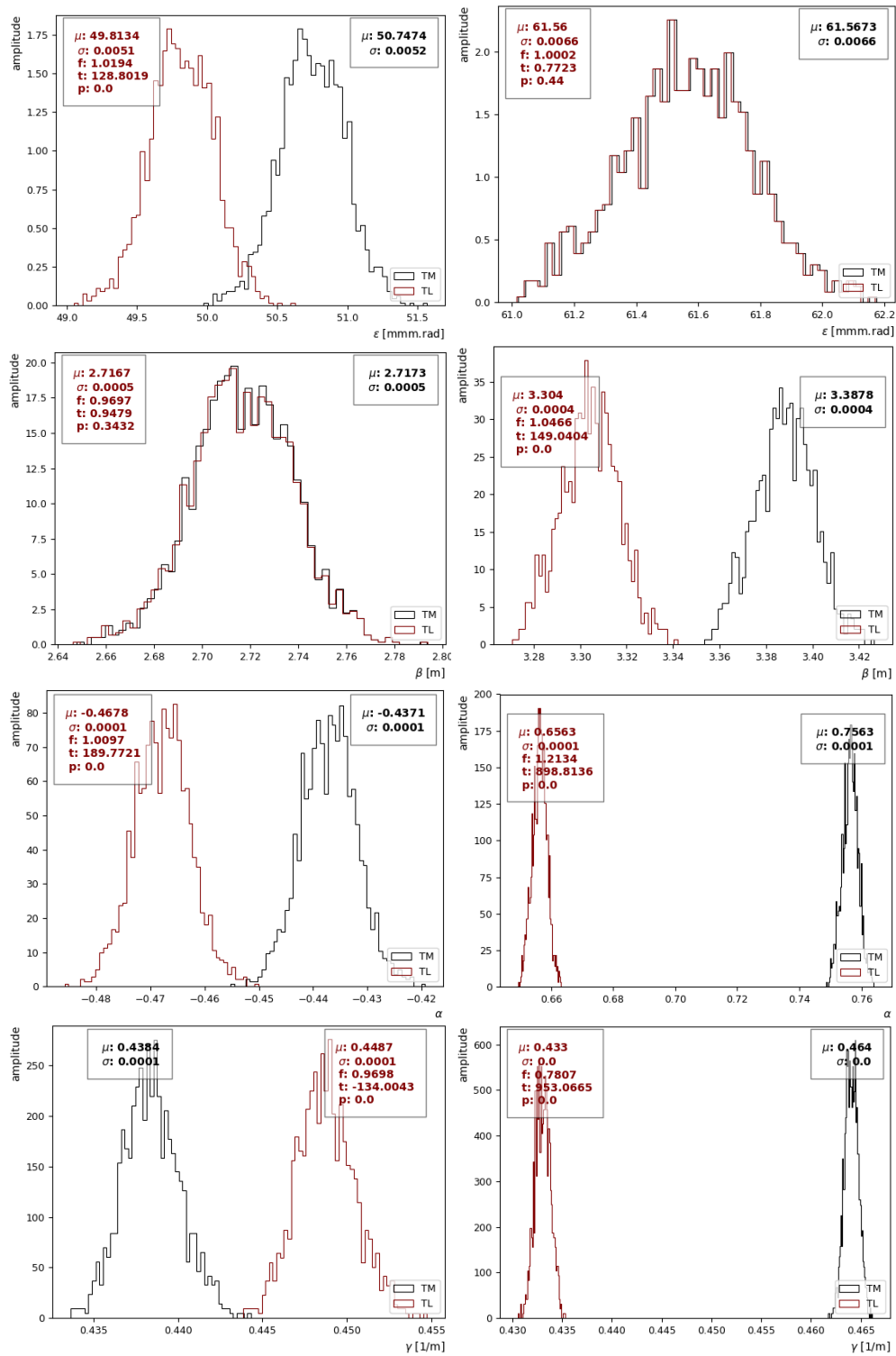


Figure 4.5: **Normalized emittance and Twiss parameters distributions.** Monte Carlo uncertainty propagation results for horizontal (left) plane and vertical plane (right). Multi Bunch mode at $E = 147.592$ MeV

Finally, Table 4.1 summarizes all the results extracted from ϵ_N and Twiss parameters distributions showed before.

	SINGLE BUNCH				MULTI-BUNCH			
Energy (MeV)	147.758				147.592			
Spread %	0.180				0.415			
Plane	Horizontal		Vertical		Horizontal		Vertical	
	TM	TL	TM	TL	TM	TL	TM	TL
ϵ_N (mm.mrad)	53.855	53.107	51.067	51.112	50.7474	49.8134	61.5673	61.560
β (m)	2.6496	2.6229	2.9885	2.8478	2.7173	2.7167	3.3878	3.3040
α	-0.0835	-0.1114	1.3057	1.1922	-0.4371	-0.4678	0.7563	0.6563
γ (1/m)	0.3801	0.386	0.9051	0.8503	0.4384	0.4487	0.4640	0.4330

Table 4.1: **Beam parameters and energy results at the LINAC exit, SIRIUS.**

Using the beam parameters showed in Table 4.1 it is possible determine the beam ellipse equations in phase space at P_0 . For the Single-Bunch mode are:

$$0.380x^2 - 0.167xx' + 2.649x'^2 = 0.186, \quad (4.1)$$

$$0.905x^2 + 2.611xx' + 2.988x'^2 = 0.176, \quad (4.2)$$

for horizontal and vertical plane respectively. For Multi-bunch mode are:

$$0.438x^2 - 0.935xx' + 2.717x'^2 = 0.175, \quad (4.3)$$

$$0.464x^2 + 1.512xx' + 3.387x'^2 = 0.212, \quad (4.4)$$

for horizontal and vertical plane respectively. Then, these beam ellipse equations can be used to simulate how the beam will propagate from the LINAC to Booster. The phase space ellipses have different orientations due to in horizontal plane the beam is focused and in the vertical plane the beam is defocused, see Figure 4.6.

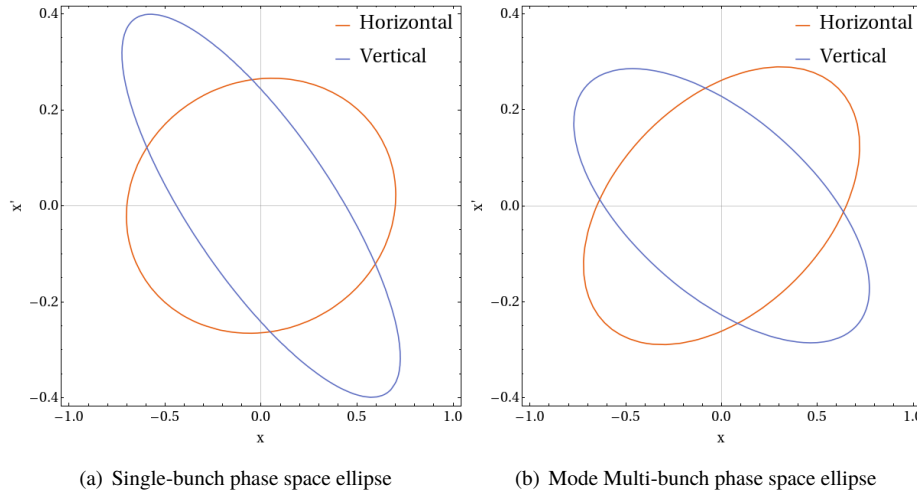


Figure 4.6: **Phase space ellipses at the LINAC exit.** As expected the equation of motion for each operation mode in both planes describes an ellipse in phase space.

4.2 Beam optical diagnostic system at CLEAR*.

This section will provide experimental results collected by BTV and Basler cameras using the created PYTHON-based quad-scan and emittance analysis scripts.

4.2.1 Quadrupole Scan Fitting

This section shows the results of the beam mean size obtained for horizontal and vertical quadrupole scan with their respective standard uncertainty of the mean. As mentioned earlier, these beam size values depends of the quadrupole current and describe a quadratic parabola.

Horizontal Plane Analysis

Figure 4.7 and Table 4.2 summarize the results of the QFD510 quadrupole current I vs. the horizontal beam size. Note that near the minimum of the parabola the beam uncertainties obtained in both BTV and Basler cameras are relatively small.

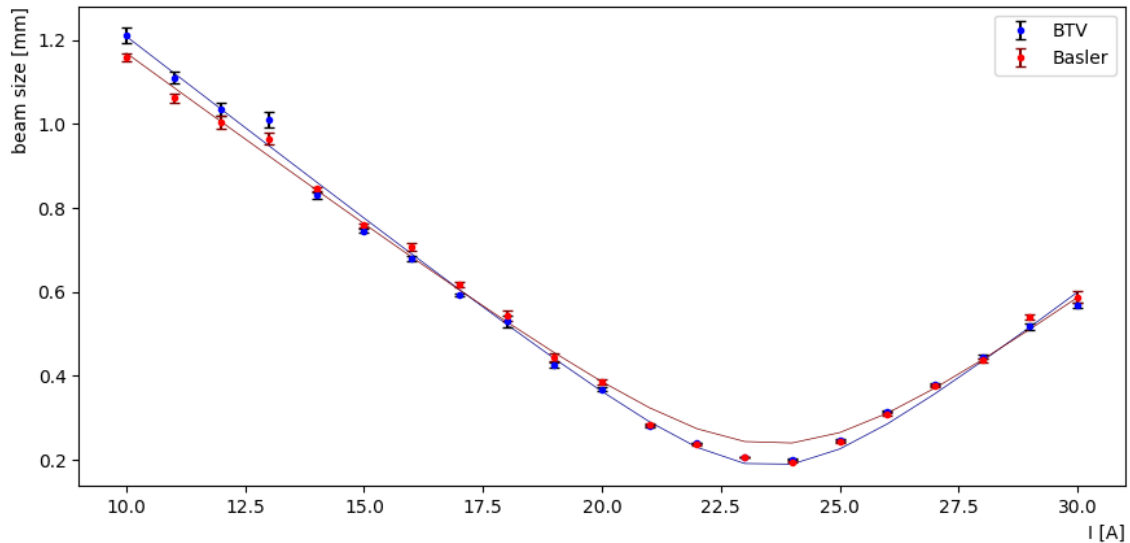


Figure 4.7: **CLEAR quad-scan QFD510 beam results.** Fitting for BTV and Basler cameras are shown with their corresponding uncertainties. Current range: 10-30 A at $E = 200$ MeV. Horizontal plane.

*This section was performed under supervision and collaboration with CLEAR group of CERN

Currents			BTV Camera		Basler Camera	
I1	I2	I3	Beam Size	Uncertainty	Beam Size	Uncertainty
A	A	A	mm	mm	mm	mm
20	0	10	1.21109414	0.01768955	1.15991254	0.00930433
20	0	11	1.11081910	0.01304858	1.06173458	0.00986736
20	0	12	1.03519630	0.01429802	1.00475742	0.0146482
20	0	13	1.00965021	0.01816018	0.96526001	0.01309515
20	0	14	0.83015494	0.00772617	0.84565821	0.00484977
20	0	15	0.74560703	0.00532294	0.75863304	0.00347194
20	0	16	0.67881239	0.00600965	0.70696501	0.00932774
20	0	17	0.59330877	0.00399306	0.61779463	0.00623516
20	0	18	0.52980625	0.01308275	0.54320197	0.01209205
20	0	19	0.42675374	0.00626097	0.44424522	0.00876266
20	0	20	0.36738059	0.00471802	0.38492807	0.00586329
20	0	21	0.28103501	0.00253438	0.28365901	0.00422652
20	0	22	0.24046656	0.00083161	0.23647056	0.00151724
20	0	23	0.20651354	0.00075555	0.20633116	0.00069846
20	0	24	0.20146944	0.00057423	0.19551512	0.00093229
20	0	25	0.24774182	0.00292849	0.24340826	0.00318868
20	0	26	0.31478410	0.00154311	0.30882198	0.00199913
20	0	27	0.38014562	0.00244329	0.37630138	0.00218089
20	0	28	0.44580303	0.0044087	0.43775043	0.00516152
20	0	29	0.51717359	0.0082498	0.5401986	0.00735925
20	0	30	0.56813167	0.00751788	0.58783804	0.01396973

Table 4.2: **Quadrupole Scan QFD510 results (CLEAR)**. Horizontal plane, I1=QDF520, I2=QDD515, I3=QFD510.

Also, look that BTV uncertainties far from the minimum of the parabola begin to be considerable. In contrast, for the Basler camera, these uncertainties continue to be relatively smaller than BTV camera. Besides, observe that in the extreme values of the parabola the results obtained for both cameras at the extremes begin to diverge causing a global different fitting trend.

Now, consider the results of normalized emittance and the Twiss parameters for an equidistant current range respect to the minimum of the parabola, a specific range where the uncertainties are relatively small in both cameras. The range from 18 to 28 amperes is taken and the distribution results are showed in Figure 4.8.

Note that two distributions of each parameter are very close between them, especially in the case of normalized emittance where both distributions are on top of each other. Then, the means of each parameter are analyzed. As was do in the previous section, first an analysis over the variances is required. For the normalized emittance distributions, a $f = 0.5918$ is obtained, which is inside the equal variances acceptance. Then, the t -test gives a $t = 1.111$ corresponding a $p > \alpha$, meaning equal normalized emittance distributions. Even more, the area from one tail to zero of the subtracted emittance distributions is $a = 0.484$ that is so close to 0.5, value that means perfectly zero

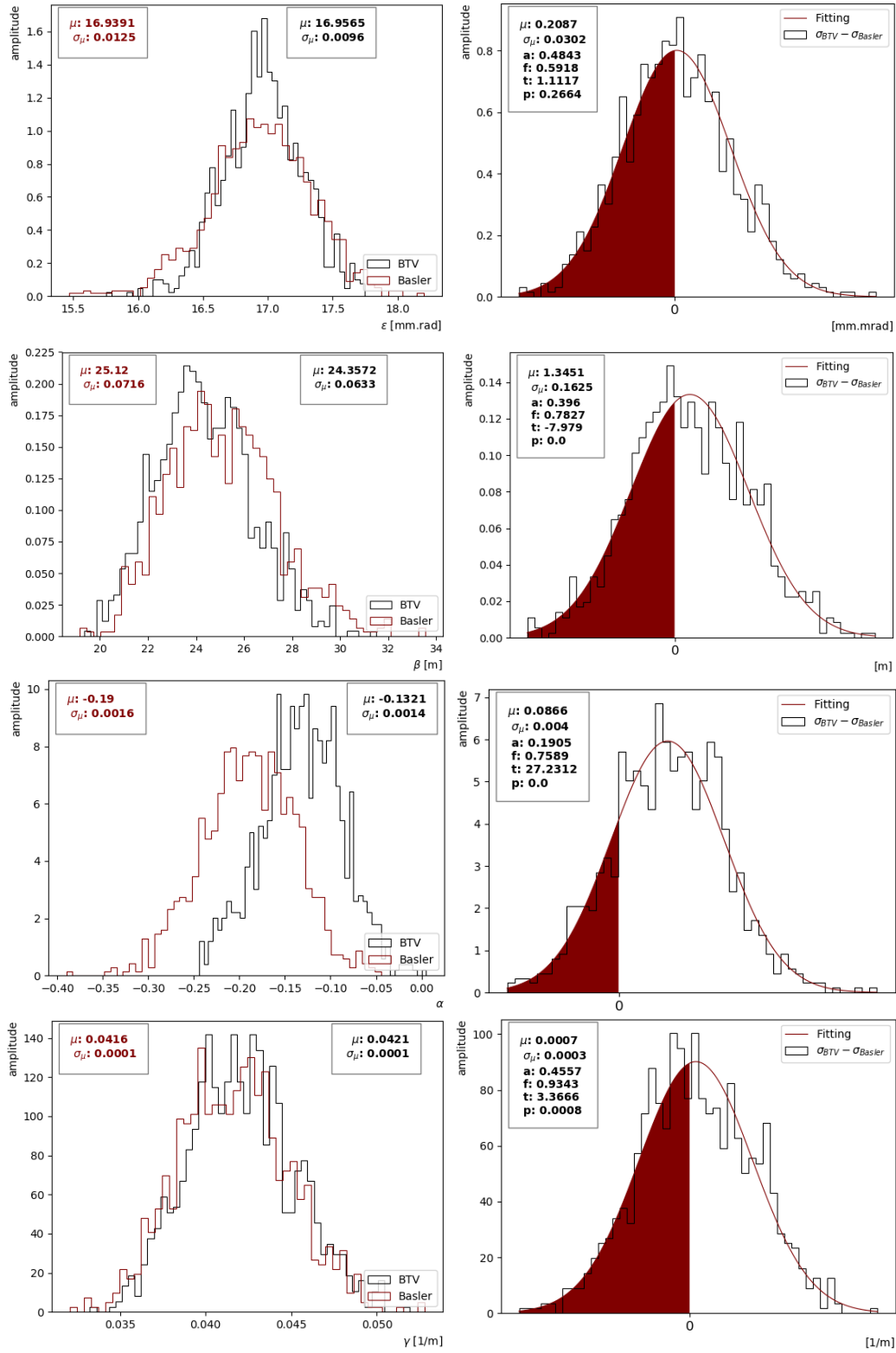


Figure 4.8: **CLEAR horizontal plane analysis.** Current range from 18-28 A. Left: Normalized emittance and Twiss parameters distributions for quad-scan QFD510 at E = 200 MeV. Right: Subtracted mean distributions and their respective statistics analysis results.

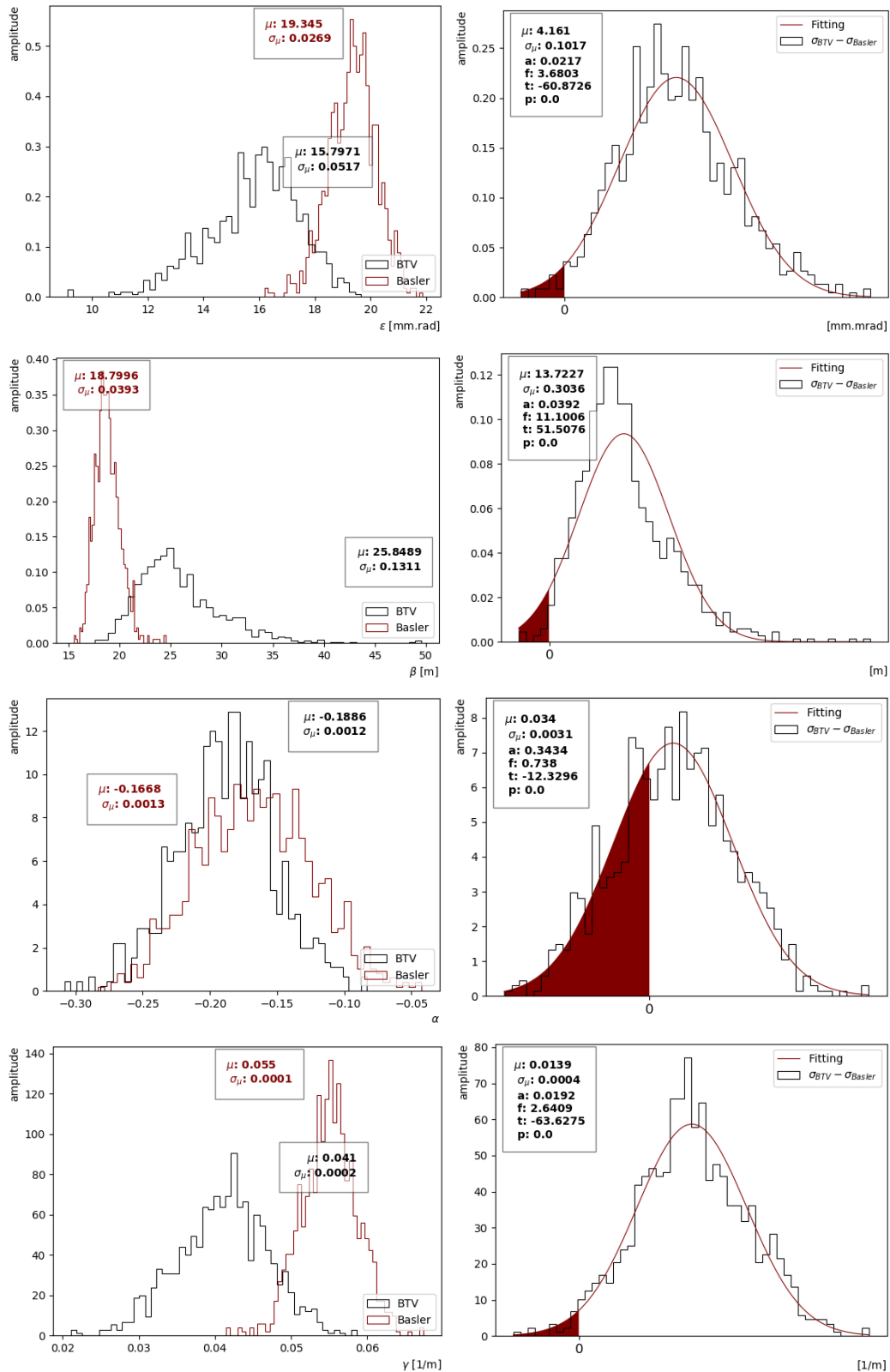


Figure 4.9: **CLEAR horizontal plane analysis.** Current range from 10-30 A. Left: Normalized emittance and Twiss parameters distributions for quad-scan QFD510 at E = 200 MeV. Right: Subtracted mean distributions and their respective statistics analysis results.

centered distribution. If the distributions of the means are perfectly equal, the new subtracted distribution should have a peak around zero. For the Twiss parameters, reasonable a -values were also obtained, especially with $a_\beta = 0.396$ and $a_\gamma = 0.456$. The worst result was obtained in the α difference distribution with $a_\alpha = 0.190$, $f = 0.758$ and $p < \alpha$, but in general as a global result, they can be considered as valid. These results are prove that both cameras can take considerable correct emittance measurements under small dynamic ranges.

In practice, it is not always possible to perform quad-scan in the first instance with measures equidistant from the lowest point of the fitted beam size parabola. To obtain equidistant measures, these are obtained after performing the first quad-scan and see where the smallest beam size is located. This is a process that takes a lot of time and resources. In addition, in accelerator physics, there are no studies that analyze two sources of data collection and their behaviour in small and long beam size ranges. This is the reason because we are going to analyze a long and non-centred dynamic range of currents.

Now, consider the case for the entire range of currents from 10 to 30 A where their normalized emittance and Twiss parameters distributions are shown in the Figure 4.9. At first glance, it is possible to identify that the results for both cameras are different. It is clear that the distributions of the means for the 4 parameter are far from each other, except for the alpha parameter, which can only be a coincidence. And as expected the p -value for these distributions is also very small, becoming practically zero. This fact comes from the small discrepancies in the beam size results for currents far from the center of the parabola of Figure 4.7, as mentioned before.

A positive aspect to mention is that the results of the new digital Basler camera have a lower standard deviation than BTV camera, coming from the small relative uncertainties of the beam size that were obtained along the parabola. Besides, it is necessary to take into account that the Basler camera it is not totally commissioned. After fix it, reduced beam size uncertainties are expected and in consequence, reduced normalized emittance and Twiss parameters. Also, after a better alignment would be interested to test and compare what will be the new changes in beam sizes and their influence in the global results.

Vertical Plane Analysis

On the other hand, Figure 4.10 and Table 4.3 show the results of the quad-scan in the QFD520 quadrupole, to see its influence in the beam size for the vertical plane. In this case, the uncertainties of the beam sizes through the entire parabola remain small in both BTV and Basler cameras, as was expected. Remember that this effect come from betatron oscillation only in horizontal plane. Another interesting fact to note is that for small currents the two cameras give very similar results but when the current is too large (greater than 35 A), the beam sizes begin to show significant differences between both cameras, which promises different results when calculating the normalized emittance and Twiss parameters. That is why we are going to analyze mainly the case where a current end is 35 A.

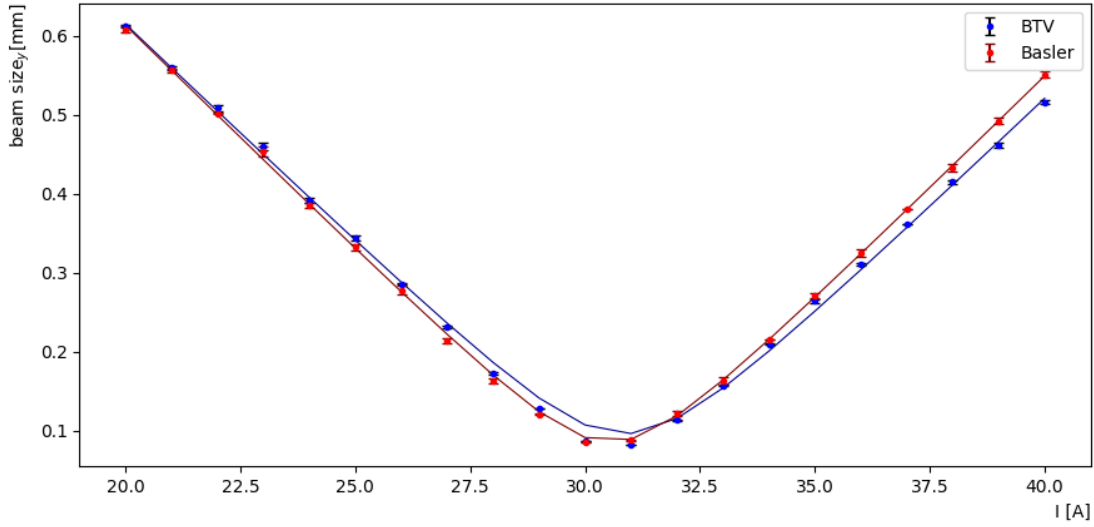


Figure 4.10: **Quad-scan results QFD520 at 200 MeV, vertical plane.** The standard errors of the mean describe a quadratic dependence as function of the quadrupole current.

Currents			BTV Camera		Basler Camera	
I1	I2	I3	Beam Size	Uncertainty	Beam Size	Uncertainty
A	A	A	mm	mm	mm	mm
20	0	15	0.61202642	0.00078556	0.60801146	2.4875e-03
21	0	15	0.5590718	0.00199073	0.55601117	1.1638e-03
22	0	15	0.50818414	0.00261279	0.50171594	8.5734e-04
23	0	15	0.45931354	0.00272733	0.45368335	3.5932e-03
24	0	15	0.39185305	0.00223177	0.38549502	1.6171e-03
25	0	15	0.34340692	0.00168263	0.33197195	2.3767e-03
26	0	15	0.28577689	0.0002002	0.27745130	3.0172e-03
27	0	15	0.23084467	0.00099743	0.21408367	1.8133e-03
28	0	15	0.17221296	0.00112002	0.16225145	1.9845e-03
29	0	15	0.12769298	0.00031991	0.12067659	7.9501e-04
30	0	15	0.08677956	0.00031778	0.08476629	2.4051e-04
31	0	15	0.08142836	0.00016791	0.08744078	4.0027e-04
32	0	15	0.1130646	0.00048762	0.12101557	1.9901e-03
33	0	15	0.15681402	0.00032003	0.16300252	2.4457e-03
34	0	15	0.20945553	0.00032871	0.21509890	2.1499e-04
35	0	15	0.26364369	0.00180724	0.27048127	2.5366e-03
36	0	15	0.30981912	0.00084761	0.32503442	2.4870e-03
37	0	15	0.36109203	0.00031372	0.38051733	3.7122e-05
38	0	15	0.41450307	0.00134405	0.43312147	2.5257e-03
39	0	15	0.4608699	0.00180108	0.49173358	2.4073e-03
40	0	15	0.51581484	0.00140992	0.55054430	2.2083e-03

Table 4.3: **Quad-scan QFD520 results (CLEAR):** Vertical plane, I1 = QFD520, I2 = QDD515, I3 = QFD510.

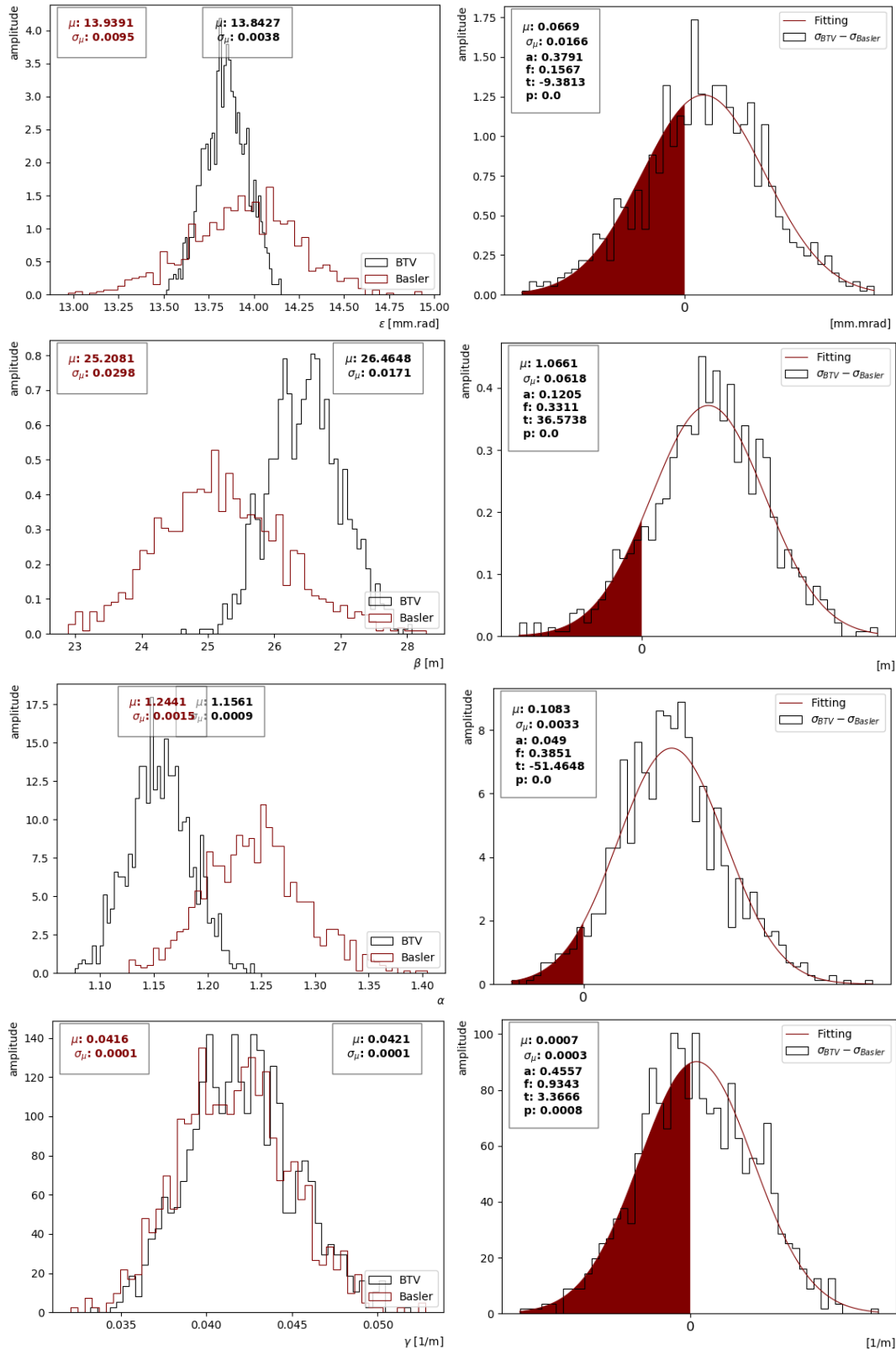


Figure 4.11: **CLEAR Vertical plane analysis.** Current range from 27-38 A. Left: Normalized emittance and Twiss parameters distributions for quad-scan QFD520 at E = 200 MeV. Right: Subtracted mean distributions and their respective statistics analysis results.

The left hand side of Figure 4.11 shows the normalized emittance and Twiss parameters distributions results for a current range of the quadrupole QDF520 that goes from 27 to 35 A. Note that the mean values of each parameter are relatively close to each other. But the standard deviations are not too similar. An interested result is obtained doing the f -test over all the distributions, where in almost all the cases $f < 0.5$. Then, all the distributions BTV and Basler have different variances. Now, checking for the area a -value, considerable large values are obtained, specially for ϵ_N and γ distributions. But despite these significant results, too small $p < \alpha$ values are obtained to validate that the corresponding both distributions are totally equal. 35 A is shown to be a breaking point, from this current value the distributions begin to be unlike and give different global results, result that also seems to be associated with a bad alignment of the Basler camera.

As expected, from the vertical plane significant p -values were obtained below 35 A, where the highest $p = 0.3791$ belongs to the normalized emittance distributions and the lowest $p = 0.049$ to the α parameter.

4.2.2 Dynamic range analysis

Something interesting to test would be how different current dynamic ranges affect the normalized emittance and Twiss parameters distributions in both cameras. In the horizontal plane, this is done using the observed fact that beam sizes far from the minimum of the parabola begin to diverge, causing slightly different parabolas and therefore different global results, compare again the results of Figure 4.8 and Figure 4.9.

Hence, how the normalized emittance and the Twiss parameters behaved under different dynamic ranges was tested, see Figure 4.12, for the following current ranges

N° Range	1	2	3	4	5	6	7	8	9
Current (A)	21-25	20-26	19-27	18-28	17-29	16-30	14-30	12-30	10-30

Table 4.4: **Different dynamic ranges.** Different current ranges to analyze until what range the results are similar for both cameras.

In general, the Figure shows that normalized emittance and Twiss parameters for both cameras have values that follow the same trend until they reach the current range seven. In it, the values of Emittance and Twiss parameters begin to diverge. To explain this, observe Figure 4.7 where the 2 beam mean sizes in each current, ranging from 10 to 13 have high discrepancies between them, which affects the results of normalized emittance and Twiss parameters for ranges 8 and 9.

After analyzing how the emittance and Twiss parameters behave in different current ranges, the better results are obtained in range 4, it has the biggest p -value and more likely results. Then, the normalized emittance and Twiss parameters results are shown in Table 4.5 and Table 4.6 as good results for the horizontal and vertical plane respectively .

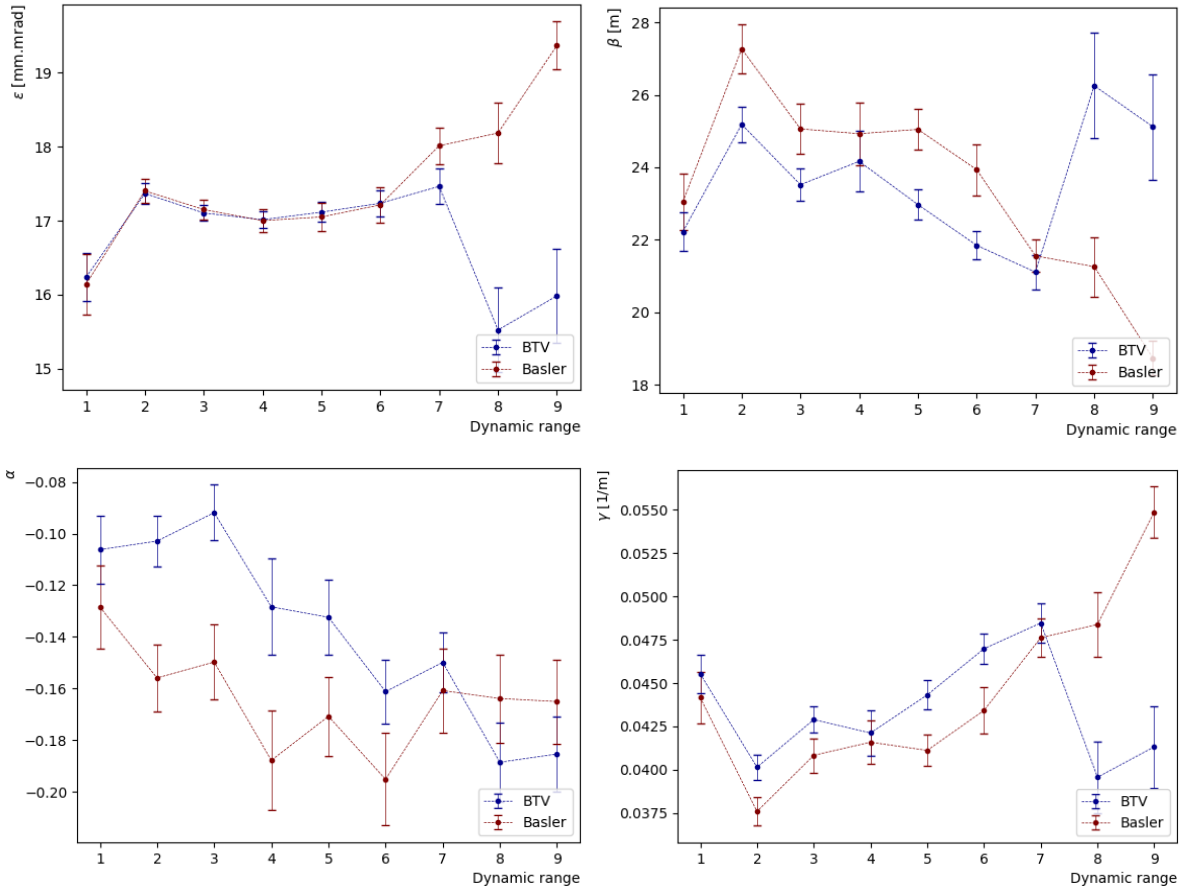


Figure 4.12: CLEAR **Dynamical range analysis**. Emittance and Twiss parameters results as function of different dynamic ranges. Horizontal plane.

	ϵ_N mm.mrad	$\delta\epsilon_N$ mm.mrad	β m	$\delta\beta$ m	α	$\delta\alpha$	γ 1/m	$\delta\gamma$ 1/m
BTV	16.96	0.01	24.36	0.06	-0.132	0.001	0.0421	0.0001
Basler	16.94	0.01	25.12	0.07	-0.190	0.002	0.0416	0.0001

Table 4.5: **Global beam results for normalized emittance and Twiss parameters. Horizontal Plane**

	ϵ_N mm.mrad	$\delta\epsilon_N$ mm.mrad	β m	$\delta\beta$ m	α	$\delta\alpha$	γ 1/m	$\delta\gamma$ 1/m
BTV	13.843	0.004	26.46	0.02	1.1561	0.0009	0.042	0.0001
Basler	13.94	0.01	25.21	0.03	1.244	0.001	0.0416	0.0001

Table 4.6: **Global beam results for normalized emittance and Twiss parameters. Vertical Plane**

4.2.3 Improvements

- To improve future measurements it is necessary a better alignment in the Basler camera, specially to analyze measurements with currents where the beam size is relatively large and compare the differences obtained between both cameras.
- To upgrade the future digital optical system, new hardware control is needed, including screen movement (pneumatic and motorized), filter or iris movement, light(s), and camera power cycle.
- Implement in JAPC an image processing tool which directly returns statistical quantities like fitted mean, sigma, and profiles given an AOI — saving a lot of processes in various monitoring GUIs running on workstations and delivering data at a high rate. Implementing also, a tool to flip and transpose the images before processing, complemented with an image background subtraction system using a new field name to separate from raw images.
- The implementation of the new class in the pyBasslerRDA software that includes the setting of all the user-relevant persistent parameters, including expert parameters such as screen calibrations, flips, history of the settings, and typical user-settings like AOI, fit AOI, camera gain, etc. Besides, the implementation of an indicator of background removal straightforward to set or disable.

Chapter 5

Conclusions

Beam dynamics and optical properties have been studied in two different accelerator structures, SIRIUS and CLEAR. For the calculation of normalized emittance in the SIRIUS LINAC, two ways of calculation have been used, Transfer Matrix and Thin Lens approximation. Both methods yield similar results by correctly choosing an equidistant range for the quadrupole current.

The normalized emittance and Twiss parameters at the output of the LINAC have been determined for the Single-Bunch and Multi-Bunch modes. These results are shown in Table 4.1 and satisfactorily approximate the design requirements for the correct operation of the beam at the LINAC exit. Moreover, on 02/21/2019 these values have been used to simulate the optimal configuration of the focus magnets in the transport line LTB and the result has been tested and they have been shown to achieve a stable electron beam orbit and correctly injection into the Booster. Moreover, experimentally on 02/24/2019, these beam parameters values has been crossed by the LTB in the direction of the Booster entrance. It is clear that in order to improve the results obtained, greater adjustments in the beam parameters, in the current range and energy parameters of the different components of the LINAC are necessary.

Regarding the CLEAR results shown in Table 4.5 and Table 4.6, the new Basler installed camera promises significant improvements in the Beam Imaging System. The positive qualities are: provide simultaneously a wide field of view, better quality and sharpness of the image, less noisy, small relative errors for the beam size at points far from the minimum of the parabola and higher dynamic range. However, there are some issues to fix, specially with the server (the Basler camera is not correctly shielded) crashing, as well as the lack of constant camera settings and calibrations. When comparing both cameras, the difference of means test for normalized emittance and Twiss parameters distributions fall in a range of p -value acceptance, meaning that both cameras are acquired the same data, but the Basler camera with better quality for large dynamic ranges.

Bibliography

- [1] Amanda Schupak. World population to top 11 billion by end of century. Retrieved from <https://www.cbsnews.com/news/world-population-to-top-11-billion-by-end-of-century>, 2015. 03-21-2019.
- [2] Johan Schot and W. Edward Steinmueller. Three frames for innovation policy: Rd, systems of innovation and transformative change. *Research Policy*, 47(9):1554 – 1567, 2018.
- [3] M Stanley Livingston and LIVINGSTON MS. Early history of particle accelerators «. 1980.
- [4] Ernst-Eckhard Koch, Dean Eric Eastman, and Y Farges. Synchrotron radiation-a powerful tool in science. *handbook on synchrotron radiation*, 1:1–63, 1983.
- [5] LNLS. Industrial use of synchrotron light sources. Retrieved from <https://www.lnls.cnpem.br/activities/industrial-applications-of-synchrotron-light-sources/>, 2019. 11-23-2019.
- [6] Vernon D Barger. *Collider physics*. CRC Press, 2018.
- [7] I Kraus, J Cleymans, H Oeschler, and K Redlich. Particle production in p- p collisions and predictions for s= 14 tev at the cern large hadron collider (lhc). *Physical Review C*, 79(1):014901, 2009.
- [8] Pierre Papon. European scientific cooperation and research infrastructures: Past tendencies and future prospects. *Minerva*, 42(1):61–76, 2004.
- [9] Philip Willmott. An introduction to synchrotron radiation: Techniques and applications. *A John Wiley & Sons*, 2:341, 2011.
- [10] Shanghai Institute. Technical design report for the sirius electron linear accelerator. In *Conf. Proc.*, volume 6906161, pages 1–147, 2013.
- [11] LNLS. *Projeto Sirius, a nova fonte de luz síncrotron*. 2014.
- [12] LNLS. Machine:magnets. Retrieved from <https://wiki-sirius.lnls.br/mediawiki/index.php/Machine:Magnets/>, feb 2018. 05-24-2017.

- [13] Arsenij Aleksandrovič Sokolov and Igor Michajlovic Ternov. Synchrotron radiation. *Akademia Nauk SSSR, Moskovskoie Obshchestvo Ispytatelei prirody. Seksia Fiziki. Sinkhrotron Radiation, Nauka Eds., Moscow, 1966* (Russian title: *Sinkhrotronnoie izluchenie*), 228 pp., 1966.
- [14] Steven L Hulbert and Jill M Weber. Flux and brightness calculations for various synchrotron radiation sources. *Nuclear Instruments and Methods in Physics Research Section A: Accelerators, Spectrometers, Detectors and Associated Equipment*, 319(1-3):25–31, 1992.
- [15] Helmut Wiedemann. *Particle accelerator physics*. Springer, 2015.
- [16] Shyh-Yuan Lee. *Accelerator physics*. World scientific publishing, 2018.
- [17] Pomeranchuk I. Iwanenko D. On the maximal energy attainable in a betatron. *Phys. Rev.*, 65:343, May 1944.
- [18] H. Pollgck F. Elder, R. Langmuir. Radiation from electrons accelerated in a synchrotron. *Phys. Rev.*, 74:52–56, March 1948.
- [19] P. HARTMAN D. TQMBQULIAN. Spectral and angular distribution of ultraviolet radiation from the 300-mev cornell synchrotron. *Phys. Rev.*, 102:1423–1447, November 1955.
- [20] Christof Kunz. Synchrotron radiation. 1974.
- [21] LNLS. IntroduçãO aos aceleradores. Retrieved from <https://www.lnls.cnpm.br/sirius/introducao-a-maquinal/>, 2019. 05-20-2019.
- [22] R. Clarke. *INCOHERENT SOURCES: Synchrotrons*, pages 273–306. Elsevier, Amsterdam, 2005.
- [23] European Synchrotron Radiation Facility. History. Retrieved from <https://www.esrf.eu/home/about/History.html>. 09-30-2019.
- [24] Herman Winick. Fourth generation light sources. In *Proceedings of the 1997 Particle Accelerator Conference (Cat. No. 97CH36167)*, volume 1, pages 37–41. IEEE, 1997.
- [25] Pedro F Tavares, Simon C Leemann, Magnus Sjöström, and Åke Andersson. The max iv storage ring project. *Journal of synchrotron radiation*, 21(5):862–877, 2014.
- [26] LNLS. Ceremony marks the first stage of the sirius project. Retrieved from <https://lightsources.org/lightsources-of-the-world/americas/brazilian-synchrotron-light-laboratory>, 2019. 04-23-2019.
- [27] Stuart Henderson. Status of the aps upgrade project. 2015.
- [28] Y Okayasu, C Mitsuda, K Fukami, K Soutome, T Watanabe, and T Nakamura. High field gradient multi-pole magnets with permendur alloy for the spring-8 upgrade.
- [29] D. Roque da Silva. Sirius: The new brazilian synchrotron light source.

- [30] Christoph Steier, Jin-Young Jung, Hiroshi Nishimura, Serena Persichelli, Richard Donahue, Marco Venturini, Olusola Omolayo, Eric Buice, Andre Anders, Steve Virostek, et al. Status of the conceptual design of als-u. 2018.
- [31] Kyrre Sjobak, Erik Adli, Michele Bergamaschi, Stephane Burger, Roberto Corsini, Alessandro Curcio, Stephane Curt, Steffen Döbert, Wilfrid Farabolini, Davide Gamba, et al. Status of the clear electron beam user facility at cern. In *10th Int. Particle Accelerator Conf.(IPAC'19), Melbourne, Australia, 19-24 May 2019*, pages 983–986. JACOW Publishing, Geneva, Switzerland, 2019.
- [32] David I Thwaites and John B Tuohy. Back to the future: the history and development of the clinical linear accelerator. *Physics in Medicine & Biology*, 51(13):R343, 2006.
- [33] LNLS. Machine : Injection system. Retrieved from https://wiki-sirius.lnls.br/mediawiki/index.php/Machine:Injection_System/, 2019. 04-20-2019.
- [34] D Gamba, Roberto Corsini, S Curt, Steffen Doebert, W Farabolini, G Mcmonagle, PK Skowronski, F Tecker, S Zeeshan, Erik Adli, et al. The clear user facility at cern. *Nuclear Instruments and Methods in Physics Research Section A: Accelerators, Spectrometers, Detectors and Associated Equipment*, 909:480–483, 2018.
- [35] Alban Mosnier, Martial Authier, Daniel Bogard, Aline Curtoni, Olivier Delferriere, Gilles Dispau, Romuald Duperrier, Wilfrid Farabolini, Patrick Girardot, Marcel Jablonka, et al. The probe beam linac in ctf3. In *Tenth European Particle Accelerator Conference" EPAC'06"*, pages 679–681, 2006.
- [36] IN Ross. Feasibility study for the cern" clic" photo-injector laser system. Technical report, 2000.
- [37] Rudolf Bossart, JHB Madsen, P Pearce, JC Godot, Louis Rinolfi, JP Delahaye, and AJ Riche. The lep injector linac. Technical report, CM-P00059430, 1990.
- [38] G Bienvenu, JC Bourdon, P Brunet, J Rodier, et al. Accelerating structure developments for the lep injector linacs (lil). 1984.
- [39] Agnese Lagzda, Roger Jones, James Jones, Karen Kirkby, W Farabolini, and Deepa Angal-Kalinin. Relative insensitivity to inhomogeneities on very high energy electron dose distributions. 2017.
- [40] Maris Tali, Rubén García Alía, Markus Brugger, Veronique Ferlet-Cavrois, Roberto Corsini, Wilfrid Farabolini, Giovanni Santin, and Ari Virtainen. Mono-energetic electron induced single-event effects at the vesper facility. In *2016 16th European Conference on Radiation and Its Effects on Components and Systems (RADECS)*, pages 1–5. IEEE, 2016.
- [41] W Farabolini, D Bogard, A Brabant, A Curtoni, P Girardot, F Gobin, R Granelli, and F Harrault. Diagnostics for the ctf3 probe beam linac califes. *Transport*, 2(m2):5m, 2007.
- [42] N Baboi and Germany N Rouvière. Beam position monitors using a re-entrant cavity.

- [43] Rui Pan, Alexandra Andersson, D Walsh, W Gillespie, S Mazzoni, W Farabolini, M Martyanov, S Rey, A Goldblatt, T Lefevre, et al. Electro-Optical bunch profile measurement at ctf3. Technical report, 2013.
- [44] Carsten P Welsch, Hans Heinrich Braun, E Bravin, R Corsini, S Döbert, T Lefèvre, F Tecker, P Urschütz, B Buonomo, Oscar Coiro, et al. Longitudinal beam profile measurements at ctf3 using a streak camera. *Journal of Instrumentation*, 1(09):P09002, 2006.
- [45] W Farabolini. Califes probe beam status. In *International Workshop on Linear Colliders*, 2010.
- [46] Wilfrid Farabolini, Guillaume Adroit, Patrick Girardot, Rémi Granelli, Francis Harrault, CLH Lahonde-Hamdoun, Thierry Lerch, and Fabienne Orsini. Video profile monitors development for the ctf3 probe beam linac. In *Proceedings of EPAC*, volume 8, page 1101. Citeseer, 2008.
- [47] W. Farabolini R. Kieffer T. Lefèvre S. Mazzoni P. Karataev M. Bergamaschi, E. Bravin. Optical transition radiation interferometry (otri) experiment in califes. CALIFES Workshop, 2016.
- [48] Marek Gasior. An inductive pick-up for beam position and current measurements. Technical report, 2003.
- [49] A Dabrowski, Mayda Velasco, HH Braun, R Corsini, S Dobert, T Lefèvre, F Tecker, and P Urschutz. Non-destructive single shot bunch length measurements for the clic test facility 3. In *2007 IEEE Particle Accelerator Conference (PAC)*, pages 4069–4071. IEEE, 2007.
- [50] Reidar Lillestøl, Alexej Grudiev, Walter Wuensch, Namra Aftab, Erik Adli, Steffen Döbert, Roberto Corsini, Wilfrid Farabolini, Juergen Pfnstner, and Sumera Javeed. Status of wakefield monitor experiments at the clic test facility. Technical report, 2016.
- [51] FJ Cullinan, ST Boogert, W Farabolini, T Lefevre, A Lunin, A Lyapin, L Søyby, J Towler, and M Wendt. Long bunch trains measured using a prototype cavity beam position monitor for the compact linear collider. *Physical Review Special Topics-Accelerators and Beams*, 18(11):112802, 2015.
- [52] Carl A Lindstrøm, KN Sjobak, Erik Adli, J-H Röckemann, L Schaper, J Osterhoff, AE Dyson, SM Hooker, W Farabolini, D Gamba, et al. Overview of the clear plasma lens experiment. *Nuclear Instruments and Methods in Physics Research Section A: Accelerators, Spectrometers, Detectors and Associated Equipment*, 909:379–382, 2018.
- [53] L.R. Carver. Califes for impedance measurements. CALIFES Workshop, 2016.
- [54] L Catani, Alessandro Cianchi, E Gabrielli, K Honkavaara, V Kocharian, H Keller, and Kay Rehlich. A distributed digital camera system for accelerator optical diagnostics. 08 2019.
- [55] VL Ginzburg. Transition radiation and transition scattering. *Physica Scripta*, 1982(T2A):182, 1982.
- [56] Carlton-B. Reid. Measurement of electron beam emittance using optical transition radiation and development of a diffuse screen electron beam monitor, 1990.

- [57] Watec. 221s2 ntsc. Retrieved from https://www.wateccameras.com/products/camera/221s2_ntsc/, 2019. 12-27-2019.
- [58] BASLER. aca1920-40gm - basler ace. Retrieved from <https://www.baslerweb.com/en/products/cameras/area-scan-cameras/ace/aca1920-40gm/>, 2019. 12-26-2019.
- [59] Matthew Sands. The physics of electron storage rings: an introduction. In *Conf. Proc.*, volume 6906161, pages 257–411, 1970.
- [60] Klaus Floettmann. Some basic features of the beam emittance. *Physical Review Special Topics-Accelerators and Beams*, 6(3):034202, 2003.
- [61] C.E. Rees. Error propagation calculations. *Geochimica et Cosmochimica Acta*, 48(11):2309 – 2311, 1984.
- [62] AT Green. Development of a python based emittance calculator at fermilab science & technology (fast) facility. Technical report, 2016.
- [63] Carl A Lindstrøm, Erik Adli, G Boyle, R Corsini, AE Dyson, W Farabolini, SM Hooker, M Meisel, J Osterhoff, J-H Röckemann, et al. Emittance preservation in an aberration-free active plasma lens. *Physical review letters*, 121(19):194801, 2018.
- [64] GM Anderson. Error propagation by the monte carlo method in geochemical calculations. *Geochimica et Cosmochimica Acta*, 40(12):1533–1538, 1976.
- [65] Barry K. Moser and Gary R. Stevens. Homogeneity of variance in the two-sample means test. *The American Statistician*, 46(1):19–21, 1992.
- [66] Graeme D Ruxton. The unequal variance t-test is an underused alternative to student’s t-test and the mann–whitney u test. *Behavioral Ecology*, 17(4):688–690, 2006.
- [67] Jagdish K Patel and Campbell B Read. *Handbook of the normal distribution*, volume 150. CRC Press, 1996.
- [68] JAPC. Java api for parameter control (japc). Retrieved from <https://wikis.cern.ch/display/JAPC/Home>, 2019.
- [69] PyDM Tutorial. Main screen. Retrieved from https://slaclab.github.io/pydm-tutorial/action/designer_main.html, 2019. 12-27-2019.
- [70] J Safranek and M Lee. Calibration of the x-ray ring quadrupoles, bpms, and orbit correctors using the measured orbit response matrix. In *AIP Conference Proceedings*, volume 315, pages 128–136. American Institute of Physics, 1994.

Abbreviations

c speed of light 2, 5, 7

BMs Bending Magnets 3

BTS Booster to Storage Ring 15

BTv Beam Observation TV xviii, xxi, 22–24

bw spectral bandwidth 6

CALIFES Concept d’Accélérateur Linéaire pour Faisceau d’Electron Sonde xiv, 11, 19, 20

CERN European Organization for Nuclear Research xviii, 10, 11, 18, 19

CLEAR CERN Linear Electron Accelerator for Research xviii, xxi, 11, 12, 18–22

CLIC Compact Linear Collider xviii, 11, 18, 21, 22

CNPEM National Center for Research in Energy and Materials 9

CTF3 CLIC Test Facility 3 11

DESY Deutsches Elektronen Synchrotron or German Electron Synchrotron 7

EOSD Electro-Optical Spectral Decoding 20

ESRF European Synchrotron Radiation Facility 8

FAC Accelerator Physics Group 49

HV high voltage 2

ICT Integrated Current Transformer 20

IDs Insertion Devices 4, 8

LHC Large Hadron Collider 11

LIL LEP Injector Linac 20

LINAC Linear Accelerator xvii, 2, 3, 12, 13, 15, 28

LTB LINAC to Booster 15, 67

OTR optical transition radiation xviii, 20–24, 37, 38

PoE Power over Ethernet 23, 24

RF Radio Frequency xvii, 2, 3, 16, 20

TL Thin Lens 51, 53, 54

TM Transfer Matrix 31, 51, 53, 54

WCM Wall Current Monitor 21

WFM Wake Field Monitor 21

YAG Yttrium Aluminium Garnet 20